Investigation of the Ligand Shells of Homo-Ligand and Mixed-Ligand Monolayer Protected Metal Nanoparticles: A Scanning Tunneling Microscopy Study

by

Alicia M. Jackson

B.S. Materials Science and Engineering
Massachusetts Institute of Technology, 2002

SUBMITTED TO THE DEPARTMENT OF MATERIALS SCIENCE AND ENGINEERING IN PARTIAL FULFILLMENT OF THE REQUIREMENTS FOR DEGREE OF

DOCTOR OF PHILOSOPHY IN MATERIALS SCIENCE AND ENGINEERING

at the
MASSACHUSETTS INSTITUTE OF TECHNOLOGY

June 2007

Signature of Author:____
Department of Materials Science and Engineering
May 21, 2007

Certified by:____
Francesco Stellacci
Finmeccanica Assistant Professor of Materials Science and Engineering
Thesis Supervisor

Accepted by:____
Samuel M. Allen
POSCO Professor of Physical Metallurgy
Chair, Departmental Committee on Graduate Students

Investigation of the Ligand Shells of Homo-Ligand and Mixed-Ligand Monolayer Protected Metal Nanoparticles: A Scanning Tunneling Microscopy Study

by

Alicia M. Jackson

Submitted to the Department of Materials Science and Engineering on May 21, 2007
in Partial Fulfillment of the Requirements for the Degree of
Doctor of Philosophy in Materials Science and Engineering

ABSTRACT

Monolayer Protected Metal Nanoparticles have recently found widespread use in and are the focus of intensive study in many areas of scientific research ranging from biology to physics to medicine. Consisting of a nanoscale, crystalline, metallic core surrounded by a self-assembled monolayer of ligands (a 3-D SAM or ligand shell), their appeal and utility stem from their numerous unique properties—many of which arise and are modulated by the intimate spatial and electronic contact between core and shell. The ligand shell controls the particle's interactions with its environment (e.g. sensing, assembly, and electron transfer ability). Furthermore, the ability to manipulate and assemble such nanomaterials through the ligand shell is paramount to their incorporation into and the development of new nanoparticle based materials and devices. However, little is known of the exact composition and packing arrangements of molecules within the ligand shell, and even less so on how to control the resulting nanostructuring.

In this thesis we present a Scanning Tunneling Microscopy investigation of the ligand shells of homo- and mixed-ligand metal nanoparticles. We develop an understanding and model of the ligand arrangements around the nanoparticle core, showing that the multifaceted, high curvature, and topologically spherical nature of the core results in a 3-D SAM that has many differences from its 2-D SAM counterparts. We show that the core curvature (and correspondingly, the changing facet to edge ratio on the core surface) of the particles is the dominant driver for the packing and behavior of the ligand shell. Most interestingly, we find that when certain two-component, mixed SAMs are assembled around the particle core, the ligands phase-separate into ordered, ribbon-like domains, only a few molecules in width—a behavior never before seen on flat surfaces. We show that both the domain morphology and width can be controlled through the ligand shell composition and the particle core size, and that the observed phase-separation is a general phenomenon across nanoparticle compositions. We present these studies as a first step towards developing a complete model of and control over the ligand shell structure of nanoparticles.

Thesis Supervisor: Francesco Stellacci
Title: Finmeccanica Assistant Professor of Materials Science and Engineering

List of Publications

- **A. M. Jackson,** J. W. Myerson, and F. Stellacci, "Spontaneous assembly of subnanometre ordered domains in the ligand shell of monolayer protected nanoparticles," *Nature Materials*, 2004.

- **A. M. Jackson**, Y. Hu, P. Jacob-Silva, and F. Stellacci, "From Homoligand- to Mixed-Ligand- Monolayer-Protected Metal Nanoparticles: A Scanning Tunneling Microscopy Investigation," *Journal of the American Chemical Society,* 2005.

- G. A. DeVries, M. Brunnbauer, **A. M. Jackson**, Y. Hu, B. Long, B. Neltner, O. Uzun, B. H. Wunsch, and F. Stellacci, "Divalent Metal Nanoparticles," *Science*, 2007.

- A. Centrone, Y. Hu, **A. M. Jackson**, G. Zerbi, and F. Stellacci, "Phase Separation on Mixed-Monolayer-Protected Metal Nanoparticles: A Study by Infrared Spectroscopy and Scanning Tunneling Microscopy," *Small*, 2007.

Acknowledgements

Here I would like to thank those who have made my research as well as my experiences at MIT so fulfilling. Firstly, to my advisor, Francesco Stellacci—the always energetic, passionate, demanding, and creative mastermind behind SuNMaG. I thank him for his constant insight and guidance and most importantly, for teaching me to go after the important, challenging, and high-risk problems in research. Also, to the entire SuNMaG group, especially the founding members: Arum Amy Yu, Robert Barsotti, Gretchen DeVries, and Markus Brunnbauer—for our many adventures in and outside of the lab. I am very thankful to my fellow STM imagers: Jill Miwa--who brought me to my imaging A-game--and also to Ying Hu, Suelin Chen, and Cedric Dubois for all of our conversations and their insights into STM. Also I want to give a very special thanks to my UROP, Paulo Jacob-Silva, whom I was incredibly blessed to have as my student. He is one of the most thoughtful and talented students that I know. Lastly, to Professor Augustus Witt who inspired me to enter materials science during my first undergraduate year at MIT. He provided me with invaluable advice and I miss his presence.

I would also like to thank that many collaborators with whom I worked during my thesis: Professor Federico Rosei of the Institut national de la recherche scientifiqe at the Universite du Quebec for use and guidance of his UHV/VT STM; Professor Royce Murray and his post-doc, Joe Tracy, at UNC Chapel Hill who provided countless samples of nanoparticles; and lastly to Professor Sharon Glozter and her graduate student, Chetana Singh, for all of their insights and computational studies on ordered phase separation

Lastly I am very grateful to my family for all of their support and thoughts during these years. Most importantly, I am most thankful to my fiancé and best friend, Dan, for his unending support and belief in me, his pure love of science and exploration, and his ability to always make me smile.

Table of Contents

Table of Figures

1. Introduction and Background

1.1. Introduction

In the past 20 years gold nanoparticles have evolved from interesting, esoteric examples of quantum confinement studied in a few scientific labs to the forefront of and one of the main players in nanotechnology. They are one of the few nanomaterials whose nanotechnological promise has come to fruition. Their ubiquity in science as well their emerging presence in industry is due to a combination of factors: 1) first and foremost are their numerous unique and novel optical and electronic properties both singularly and in aggregate form, 2) the ability to modulate these properties easily and controllably, 3) their facile and gram scale syntheses, 4) the ability to assemble such particles using self-assembly, allowing for large-scale and spontaneous formation of complex architectures and 5) the ability, through the development of scanning probe microscopies, to image, characterize, and manipulate individual particles. Additionally, nanoparticles continue to be a rich area for scientific research and development ranging from biology—ultrasensitive DNA analysis, targeted drug delivery, and MRI contrast agents--to fundamental physics—plasmonics, negative index materials, and superlensing.

Nanoparticles occupy the strange ocean between the molecular/quantum and macroscopic/classical worlds, borrowing behaviors from each and exhibiting new properties as well—the 'melting pot' of physics, if you will. Indeed they are often referred to as 'artificial' atoms as they define the building blocks of an alternate, nano-world made up of metamaterials. Monolayer protected gold nanoparticles consist of a gold crystalline core surrounded by a self assembled monolayer of thiolated molecules. Just as their behavior is ruled by the dual worlds of quantum and macroscopic, their properties are derived from the combination of metallic core and ligand shell. It is the nanoscale size of the metallic core that gives rise to the unique optical and electronic properties (e.g. surface plasmon resonance, single electron transistor behavior), but it is the ligand shell that modulates these properties (shifting SPR wavelengths and charging energies) due to its intimate spatial and electronic connections to the core. Additionally, the ligand shell serves as the link between the nanoparticle and its environment, providing the particles with solubility, controlling intermolecular interactions, and guiding assembly. While the optical and electronic properties of the nanoparticles with regards to their metallic core shape, size, and structure have been studied in depth, less is known of the ligand shell in regards to molecular packing, shell morphology and true chemical composition. For example, the rate of ligand place exchange has been found to vary with particle size, age, composition, as well as with both incoming and outgoing ligand functionality, making prediction of the reaction product nearly impossible. Thus, to direct the placement and introduction of specific molecules into the ligand shell (e.g. for sensing or to guide assembly), requires an understanding of and subsequent control over the dynamics and packing of the molecules within the ligand shell. The ability to control and predict the composition and structure of the ligand shell has direct consequences on the usability and the nature of nanoparticles, which is essential for the integration of and creation of nanoparticle devices and materials.

The focus of this thesis project is to study and understand the ligand shell ordering on gold nanoparticles through scanning tunneling microscopy (STM) and how this ordering affects interactions with their environment in the forms of solubility and protein interactions. Specifically we show that the underlying curvature of the nanoparticle core has direct consequences on the structure and ordering of the molecules within the ligand shell. We find that ligands show a packing structure that differs from flat monolayers and varies with the degree of curvature of the substrate; we use our STM measurements to propose a model for the structure of the ligand shell. Furthermore find that the phase separated domains often present in flat monolayers, form highly ordered, molecular scale domains on nanoparticles. We show that this unique ordering is a direct consequence of the high curvature and 2π rotational symmetry of the core. Lastly, we discuss and examine our data to develop an understanding of the mechanisms and driving forces behind ordered phase separations

In the following chapter I concentrate mainly on a discussion of monolayer protected metal nanoparticles. Their discovery, synthesis, unique properties, as well as differences with semiconductor particles will be discussed. Additionally, an overview of 2-dimensional self-assembled monolayers (2-D SAMs) is included in order to later to highlight and develop an understanding of the unique properties of similar (in composition) SAMs on nanoparticle cores. Characterization techniques of nanomaterials will also be discussed with particular emphasis on what these techniques have so far illustrated about the ligand shells of nanoparticles.

1.2. History of metal nanoparticles

Metal nanoparticles have been synthesized, studied, and used in various applications from coloring glass to curing illness for over 2,000 years, first appearing around the 5th or 4th century B.C. in Egypt and China.[a,1,2] The particles were recognized for their novel physical behaviors, particularly optical, which were uncharacteristic of their bulk counterparts. One of the most famous demonstrations that their unique properties were coveted and well known is their inclusion into the Lycurgus Cup; created in the 5th or 4th century B.C., the cup has the ethereal ability to appear ruby red in transmitted light and green in reflected light. It is not until the 17th-19th centuries that we find written records from various authors described the formation and uses of gold colloids in solution,[3-5] many realizing that the solutions were composed of ‘gold in the finest degree of subdivision’—that is, representative of the smallest components of matter.[6] The first reported synthesis and intensive study of gold colloids[b,7] was by Michael Faraday in 1857, who, using a two phase system, reduced an aqueous solution of chloroaurate ($AuCl_4^-$) using phosphorous in CS_2. Faraday recognized that the ‘ruby-red’ color of the solution was not due to molecular gold, but to suspended colloids, and proceeded to investigate their optical properties in both solution and the solid state noting their color change with size in solution (using a long column to allow the particles to size separate) and in the solid state with compression. He was particularly interested in understanding the differences in the interaction with light of gold particles in solution,

---

[a] It is interesting to note that the ‘curative effects’ of metal nanoparticles are only now being rigorously studied and understood. Recently it was demonstrated that gold complexes remove antigenic peptides from major histocompatibility (MHC) class II molecules, inhibiting the activation of the self-reactive T lymphocytes that cause rheumatoid arthritis or other autoimmune diseases.[1]

[b] The term ‘colloid' is usually used to distinguish the method of preparing nanoparticles, the predominant methods of preparation being growth by molecular beam epitaxy (MBE) or organometallic synthesis (colloidally-prepared).[7]

films of varying thickness, and the bulk state—studies which helped him formulate several fundamental theories on the interaction of light with metals.[8]

The first modern studies of gold colloid synthesis and their properties began with the work of Schmid and coworkers in the 1980's, who developed a synthesis method for the $Au_{55}(PPh_3)_{12}Cl_6$ cluster—a 14 Å gold core stabilized by phosphine and a member of the 'magic number' family of stable clusters (discussed below). The cluster is made by passing diborane, B_2H_6, through a 50–60 °C benzene solution of PPh_3AuCl. The diborane reduces Au(I) to Au(0) and complexes excess phosphine [9], resulting in a black powder of nanoparticles. Because the particles are a magic number cluster, they show a significantly narrow size distribution (1.4 ± 0.4 nm)—a result which aids in their characterization. Schmid extensively studied these clusters, demonstrating for the first time many of their unique properties such as discrete energy levels, as well as investigating their core structure. However, due to their small size, and hence highly energetic surfaces, as well as weak outer stabilization layer, the resulting nanoclusters have a limited thermal stability, decomposing in solution when warmed to 50–60°C [10], and thus limiting their utility to many applications and studies.

The first synthesis of stable, monolayer protected particles was soon after demonstrated by Schiffrin and coworkers[11]—a result which opened the door to metal nanoparticle research and their recognition as a new class of materials. The particles are synthesized using a simple two-phase reaction in which a gold salt is reduced in the presence of thiolated ligands (described in-depth below). The synthesis yielded particles 1-3 nm in core diameter, capped with a self-assembled monolayer of alkanethiolates. It is this dense monolayer which results in the stability, and hence utility, of such particles. The nanoparticles can be repeatedly isolated and redissolved in a variety of solvents without irreversible aggregation, allowing them to be handled as giant supramolecular assemblies for a variety of chemical manipulations and study.

1.3. Introduction to electronic properties of nanoparticles

Nanoparticles are typically composed of either a semiconductor or metal core ranging from 1-100 nm in diameter, and made up of tens to thousands of atoms. The particles' properties bridge the gap between atomic and bulk behavior, displaying characteristics from both, as well as new properties. Their small size results in electron confinement effects, generating many of their attractive electronic and optical properties.[12] Nanoparticles present a large percentage of their total atoms at the surface as compared to bulk materials: a 1.3 nm diameter gold nanoparticle has 88% of its atoms at the surfaces; a 5 nm particle, 23%; a 100 nm particle, 1.2%; and a 1000 nm particle, 0.2%.[13] Thus, due to their overwhelming presence, it is the electronic states of the surface atoms that dominate many of the properties of nanomaterials. Subsequently, those particles which are at the small end of the size spectrum tend to display molecular-like characteristics, while those at the large end tend to behave more similarly to the bulk material. Although all nanoparticles display confinement effects, the material nature of the core (whether semiconductor or metal) determines how these effects are manifested and at what length scales they occur.

1.3.1. Semiconductor nanoparticles

The term quantum confinement, when applied to low-dimensional semiconductors, describes the confinement of the exciton within the physical boundaries of the semiconductor. The exciton Bohr radius, a_B, is often used as a meter-stick to judge the extent of confinement in a low-dimensional structure, with the confinement regimes determined by comparing a_B to the diameter of the nanocrystal, D. This results in three characteristic regimes of confinement: the strongly-confined regime, $D < 2a_B$; intermediate confinement regime, $D \sim 2a_B$; and, weakly-confined regime: $D > 2a_B$.[14, 15] Note that the term 'quantum dot' is usually applied to semiconductor nanocrystals in the size limit where the particle volume is smaller than the volume defined by the Bohr radius of that particular semiconductor. It is in the strongly-confined regime that the optical properties of these quantum dots are most affected. For example, in the CdSe system, as the dimensions of the nanocrystal are reduced below the Bohr radius (a_B~5.0-5.5 nm) the optical transitions shift toward the blue (i.e toward higher energy transitions).[16, 17] This shift is due to an increase in the particle's 'effective bandgap', becoming larger than that of the bulk material, as a result of selection rules which come into play as the particle decreases in size and comes to resemble an 'artificial atom'.

1.3.2. Metal nanoparticles

In the case of metal nanoparticles, the effect of the particle dimensions on electronic properties is different from that of semiconductor particles.[12] Metal nanoparticles are able to maintain their metallic nature down to ~2 nm (for gold) in diameter; however, surface effects are present and play an increasingly larger role (with decreasing size) in modulating the electro-optical properties of the particles due to the large surface to volume ratio. Below, ~1-2 nm, the particles begin to show molecular-type behavior and the continuous density of electronic states is broken up into discrete energy levels, whose spacing between energy levels depends on the Fermi Energy of the metal and on the number of electrons in the metal (Figure 1.1).[12, 18]

Due their nanoscale core size, single electron transitions can be observed for a nanoparticle placed into a circuit. The particles show a characteristic Coulomb blockade when the charging energy, $E_{el} = e^2/2C$, to place an electron onto the particle is larger than the thermal energy, $E_T = kT$. $C = 4\pi\varepsilon_o r$ is the capacitance of the particle, where ε_o is the permittivity of free space and r is the particle radius.[2] Because this charging energy can be modulated through coupling the particle with other molecules, it has been suggested and demonstrated that the particles can be used as sensors.[19]

One of the most distinguishing features of metal nanoparticles is the presence of a surface plasmon resonance (SPR) (for gold particles it lies within the visible at ~520 nm giving the particles their typical ruby-red color in solution). Surface plasmon resonance occurs when there is an excitation of a coherent oscillation of electrons around the nanoparticle core induced by an electromagnetic field.[20] Mie, in 1908, solved Maxwell's equations for the absorption and scattering of electromagnetic radiation by spherical particles and showed that the energy of the SPR depends on both the free electron density and the dielectric medium surrounding the core. For particle sizes smaller than 20 nm, the bandwidth of the plasmon peak is inversely proportional to the radius of the particles, due to increased surface scattering.[21] Sharp decreases in the plasmon resonance peak intensity occur with decreases in particle size below 3.2 -1.4 nm due to the onset of quantum size effects, and is essentially absent below 2 nm. Additionally, because the plasmon resonance condition is sensitive to the dielectric environment, nanoparticles can be employed as sensors by examining SPR peak shifts as a function of binding events.[22]

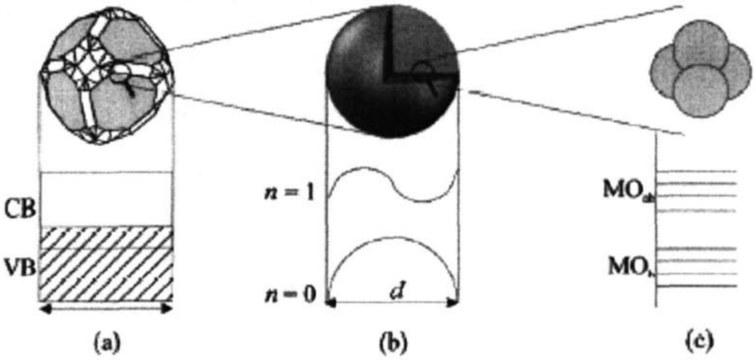

Figure 1.1 Illustration of how the size transition from a bulk metal,(a), to a nanocluster,(b), to a molecular cluster,(c), affects the electronic structure of a material. Note that in the case of the nanoparticle, b, the diameter is comparable to the exciton bohr radius, and hence surface effects begin to dominate the behavior. Taken from Schmid, G.; Baumle, M.; Geerkens, M.; Helm, I.; Osemann, C.; Sawitowski, T. Chem Soc Rev 1999, 28, 179-185.

1.4. Magic numbers and nanoparticle core shapes

The 55 atom cluster produced by Schmid is one of a series of later characterized 'magic number' clusters--so named in that the total number of Au atoms within the cluster results in fulfilling special geometrical configurations giving an extremely stable particle—hence their overwhelming prevalence as compared to clusters with non-magic numbers of atoms.[23] The nucleation and atom-by-atom growth processes of particles are governed by bonding and packing considerations, which are further affected through the kinetics and thermodynamics of the synthesis method. Since bonding effects and packing factors are electronic and steric in nature, this implies that magic numbers of atoms will result from the filling of electronic or atomic shells.[23] Thus the sequence of a nanoparticle's magic numbers carries essential information about particle's electronic and ionic structure.[24-26] The differences in the inter-atomic potentials and pairing forces lead to the significant differences in structure between materials, their mass spectra and their magic numbers.

For metal cluster sizes greater than several tens of atoms, there is strong experimental evidence that geometrical packing constraints dominate the resulting particle structure with spherical close packed geometries, particularly the Mackay filled icosahedra.[27-29] The Mackay filled icosahedra contain concentric closed icosahedral shells of atoms plus one central atom.[30] The first such magic number is 13: twelve gold atoms in a dodecahedral shell surrounding a central one. The second such shell is completed with precisely 55 atoms in total (Figure 1.2). These structures are pentagonally symmetric (a symmetry not found in bulk materials) and occur every n atoms, with n = 13, 55, ···, 1/3(2n+1)(5n2+5n+3). These geometries have been deduced by a variety of means. For example, abundance mass spectra of metal clusters up to sizes containing thousands of atoms show intensity enhancements, termed *magic numbers*, at each cluster size which corresponds to a complete Mackay icosahedron.[31]

Figure 1.2 Example of a 55-atom Mackay icoshedron. Taken from: Calvo, F.; Doye, J. P. K. *Phys Rev E* 2001, *6301*

Magic number sizes can also arise from fulfilling electronic orbitals, seen in particular for small particles, and their resulting structure and properties can be explained using the jellium model.[18, 32] In this representation, the cluster is seen as a single large atom, where the distribution of ionic cores is replaced by a constant positive background, or “jellium density”, and only the valence electrons are considered.[23] Thus, the interaction of valence electrons with the positive spherical charge distribution can be modeled with a large spherically symmetric potential well. The energy levels are calculated by solving the Schrodinger equations similarly to as one would the hydrogen atom, and additionally, delocalized electronic orbitals can be calculated. As atoms are added to the cluster, their corresponding valence electrons fill these orbitals; ‘magic numbers’ of atoms result in filled, complete orbitals, and hence preferred numbers of atoms per cluster.

Although syntheses of small magic number clusters (Au_{147} and smaller) tend to be relatively monodisperse and composed solely of magic numbers, syntheses of larger clusters tend to have more polydispersity with particles that do not conform to magic numbers due to geometric considerations and kinetic constraints during synthesis.[33] For very small clusters, the atoms can be considered very mobile during the growth process, and hence as atoms are added to the cluster, it is relatively simple for the structure to reorganize so as to fulfill geometric and electronic conditions. However, for larger clusters, as each new atom is added, it remains on the surface—thus, electronic properties are hardly affected, and hence geometrical constraints take priority.[23] For example, regular noncrystalline structures with fivefold axes of symmetry, such as icosahedra and decahedra are formed as these structures serve to minimize surface energy.

1.5. Nanoparticle synthesis

Since the initial syntheses of Schmid and Schiffrin a variety of metal nanoparticles have been synthesized ranging in size from 1-100 nm, composed of various noble metals and their mixtures, and capped with a wide array of ligands.[2] The typical synthetic mechanism is as follows: a metal salt is reduced to give zero valent metal atoms. These atoms collide in solution with other ions, atoms, or clusters, forming ‘seeds’, which then grow with the further addition of atoms. The growth is modulated through the presence of passivating molecules (e.g. thiolated ligand or surfactants) which serve to passivate the cluster against further addition of atoms. Thus, varying the ligand to gold ratio, strength of ligand-gold interaction, as well as the rate at which the reducing agent is added results in particles of varying size as well as affecting particle size polydispersity.

As mentioned briefly above, one of the strengths of the Schriffin method of nanoparticle synthesis is the resulting isolability and stability of the particles afforded by the presence of an alkanthiolate monolayer surrounding the core. The presence of a molecular layer serves to lower the free energy of the nanoparticle surface, thereby reducing the reactivity of the particle. Additionally, the steric bulk of the molecules provides a physical barrier against aggregation, and any associated charges with the molecules provide electrostatic interactions (typically repulsive) between particles. The variety of ligands utilized is large and often is a function of the synthetic method used to produce the nanoparticles. As particles are forming in solution, the passivating molecules are in a dynamic equilibrium between their adsorbed and desorbed state on the particle surface.[34] The amount of ligand in each state depends on the rates of desorption and adsorption which are related to the strength of the metal-surfactant interaction. Thus, for chemisorbed surfactants, the rate of desorption is small, and growing particles are fully capped early in the synthesis, resulting in smaller particles--indeed it is difficult to grow larger particles free from large populations of smaller particles. However physisorbed capping agents, due to their larger rate of desorption, allow for more control over nanoparticle size through varying their concentration.

The most prevalent passivating molecule for gold nanoparticles as well as for many other materials is thiolated ligands. The well studied and fairly strong (40[35, 36]-50 kcal/mol[13]) nearly covalent Au-S interaction, as well as the wide array of functionalized alkythiols available, allow for a variety of highly stable, functionalized nanoparticles. Additionally, the similar affinities of thiols for all crystalline facets results in isotropic growth of and fairly spherical shapes of particles.[13, 37] One particularly attractive property of alkanethiols monolayers is their ability to undergo place exchange with other alkanethiols and molecules (discussed in further detail below). This allows for the formation of particles with specific functionalities that may not be able to be introduced during the synthesis, as well as some control (through stoichiometry) over placing monomolecular amounts of ligands onto nanoparticles.[38]

1.6. Methods of monolayer protected metal nanoparticles synthesis

Synthesis of alkanethiolate coated nanoparticles can be achieved through various methods. Nanoparticles can be either first synthesized with a loosely bound surfactant layer which is then displaced through the addition of stronger binding thiols (the ligand exchange method), or particles can be synthesized directly with the desired ligands (direct synthesis method). Each method has its strengths and weakness--the former resulting in nearly monodisperse, but larger particles which may not be able to be functionalized with certain thiolated ligands (due to solubility or steric constraints) while the latter results in more polydisperse size distributions, but allows access to smaller particles. The "ligand-exchange" method is particularly useful if the desired ligand is not compatible with the highly reductive environment required for forming nanoparticles or if the desired ligand is particularly valuable (or simply not commercially available).

1.6.1. Citrate reduction

One of the most common and longest utilized methods of gold nanoparticle synthesis is that of sodium citrate, $3Na^+ C_3H_5O(COO)_3^{3-}$, reduction of $HAuCl_4$ in water, demonstrated by Turkevitch in 1951.[39] The method results in nearly monodisperse distributions of particles whose size can be varied from ~10-150 nm through the ratio of citrate to gold.[40] The particles are surrounded with a loose shell of citrate ions and stabilized primarily through electrostatic interactions. The surrounding citrate can be displaced through the addition of stronger binding agents. However not all of the citrate is displaced and the procedure can be difficult with the loss of charge around the particles resulting in aggregation. Additionally, with only citrate as the capping layer, the particles irreversibly aggregate upon drying, changes in pH, or ionic strength.[41]

1.6.2. Direct synthesis of alkanethiolate coated nanoparticles

Currently, alkanethiolate monolayer protected metal nanoparticles are typically synthesized using one of two similar methods. The first, that developed by Schiffrin and coworkers as discussed previously, consists of a two phase method in which a gold salt in an aqueous phase is transferred (via a phase transfer agent) to an organic phase (toluene) containing thiolated ligands, followed by reduction by with BH_4^- to form gold clusters passivatd by ligands:[11]

$$AuCl_4^- + RSH \rightarrow (-Au^{I}SR-)_n(\text{polymer}) \quad (1)$$

$$(-Au^{I}SR-)_n + BH_4^- \rightarrow Au_x(SR)_y \quad (2)$$

The details and kinetics of the reaction are not completely understood, but several details have been recently uncovered. The presence of the intermediate product of $(-Au^{I}SR-)_n$ was recently characterized for gold particles[42], as well as extensively for silver particles;[43] while the polymer forms quickly (within minutes) for Ag, the reactions is much slower for Au and takes place overnight. In reactions using a 2:1 mole ratio of $RSH:AuCl_4^-$, Murray and coworkers found that the orange-brown $R_4N^+AuCl_4^-$/toluene solution fades within 5 min after adding the alkanethiol, which they suggest may signify an alkanethiol-induced reduction to Au(I).[34] Consistent with this hypothesis are (i) the formation of oxidized thiol (the corresponding disulfide, seen by NMR) as a major byproduct of the reaction, and (ii) the stoichiometric requirement of a threefold excess of thiol to completely reduce the metal center to Au(I).[44] Also, literature syntheses for Au(I) alkanethiolate complexes, which are thought to be $[Au\text{-}S(R)\text{-}]_n$ polymers, follow a similar procedure.[45] Experiments by Murray using less reductant yielded clusters with increased average core size and larger quantities of insoluble matter, presumably aggregated clusters.[34] Because the reaction involves the reaction of $(-Au^{I}SR-)_n$ with $NaBH_4$ across the solvent interface, the rate of reaction is controlled due to interfacial stoichiometry. The reaction is amenable to a variety of ligand functionalities, ranging from polar to nonpolar, and to core metals such as Ag, Cu, and Pd, as well as alloys of these metals.[2]

The second particle synthesis method, also developed by Brust[46],and further improved by Kang and Kim for silver particles,[47] also relies upon the reduction of a gold salt in the presence of thiolated ligands, but occurs in a single phase, ethanol, at 0 °C. The synthesis is more sensitive to reaction parameters, due to the lack of interface, and is limited in the functionalities of ligands that can be introduced (due to solubility), but avoids the use of a phase transfer agent which could 'contaminate' the ligand shell of the resulting particles. Both syntheses result in a polydisperse size distribution of nanoparticles, typically between ~1-7 nm in diameter, but the median diameter can be tuned with respect to the Au to ligand ratio, ligand functionality and structure, and the reduction rate. The particles can be isolated through precipitation, filtered, and washed with a variety of solvents and then redissolved.

1.7. Self-assembled monolayers

Each parameter (core size, core metal, ligand composition) of the nanoparticle is chosen to give the desired properties to the particles: plasmon resonance, electron transfer ability, desired solubility, catalytic activity, as well as a host of other properties. Although much of the initial metal nanoparticle research focused on the electronic and optical properties in relation to the metallic core crystallographic shape, size, and composition, there is significantly less known in regards to the structure and composition of the surrounding ligand shell, or 3-D monolayer, and its contribution to nanoparticle properties. Indeed, because of the intimate spatial and electronic connection between the core and the ligand shell, many properties of the nanoparticles are modulated (e.g. surface plasmon resonance frequency, catalytic activity, and conductance) and even derived from the ligand shell (solubility). Thus, it is necessary to develop an understanding of how the ligand shell influences the properties of the nanoparticles, as well as the structure and composition and composition of the ligand shell as this fundamentally will alter the properties of the particles.

1.7.1. Structure of 2-D self-assembled monolayers

In order to better appreciate and understand the packing, conformation, and composition of the surrounding ligand shell (3-D SAM) of nanoparticles, it is illustrative to first consider 2-D SAM's of thiolated ligands on flat gold. Alkanethiolate monolayers on Au have historically been the most studied monolayer system due to the easy acquisition, preparation, and chemical inertness of gold, as well as its high binding affinity for thiols, the high stability of formed monolayers, and the numerous techniques available for characterization of the monolayers.[13] Monolayers can be formed in a variety of ways; however, the most common is to immerse the substrate into a solution of thiols (~0.01-100 μM) for ~12-18 h.[13] Complete surface coverage occurs very quickly (within minutes) with reorganization and the formation of a more ordered, denser monolayer occurring over longer time scales (hours). Alkanethiols tend to form highly ordered monolayers on extended, flat Au(111) surfaces (Figures 1.3 and 1.4). For alkanethiols of length C_n, $n<16$, FTIR and electron diffraction have shown that the molecules pack along their chain lengths into a crystalline, hexagonal array commensurate with the underlying gold lattice with a $(\sqrt{3} \times \sqrt{3})R30^{\circ}$ (or $c(4\times2)$ superlattice of a $(\sqrt{3}\times\sqrt{3})R30^{\circ}$) lattice overlayer structure (Figure 1.4).[48] That is, the sulfur-sulfur lattice spacing (~4.99 Å) is $\sqrt{3}$ times greater than the Au lattice spacing (2.88 Å) and rotated 30° with respect to the Au lattice, with the sulfur groups located in the 3-fold hollow sites.[49] This resulting packing structure is determined through the competing electronic interactions between the Au substrate atoms and sulfur atoms (hence the packing at 3-fold hollow sights) as well as the interactions between the ligand chains, with shorter chains' packing structure more influenced by the substrate and longer chains by their interchain interactions. The tilt angle (~30°) and twist of the molecules are optimized to allow for interlocking of the chain backbones, thereby maximizing van der Waals interactions between the chains while under the constraint of surface bonding at the Au lattice 3-fold hollow sites.[50]

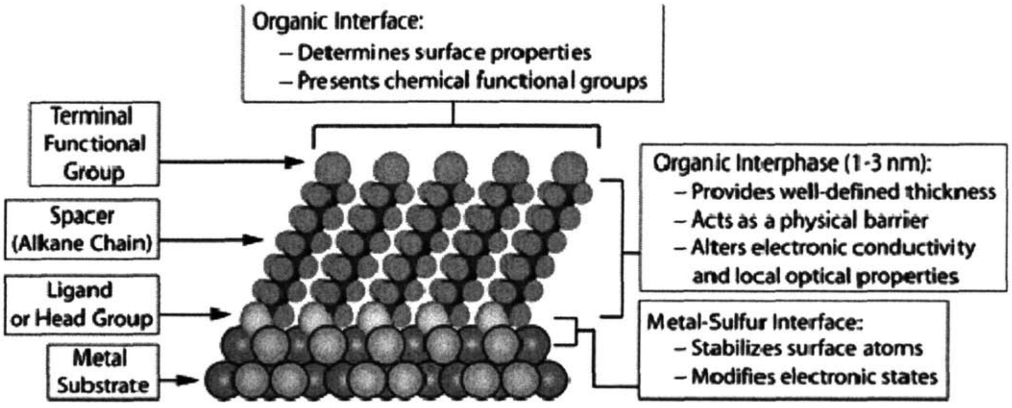

Figure 1.3 Schematic diagram of an ideal, single-crystalline SAM of alkanethiolates supported on a Au(111) surface. The anatomy and characteristics of the SAM are described. Taken from Love, J. C.; Estroff, L. A.; Kriebel, J. K.; Nuzzo, R. G.; Whitesides, G. M. Chem Rev 2005, 105, 1103-1169.

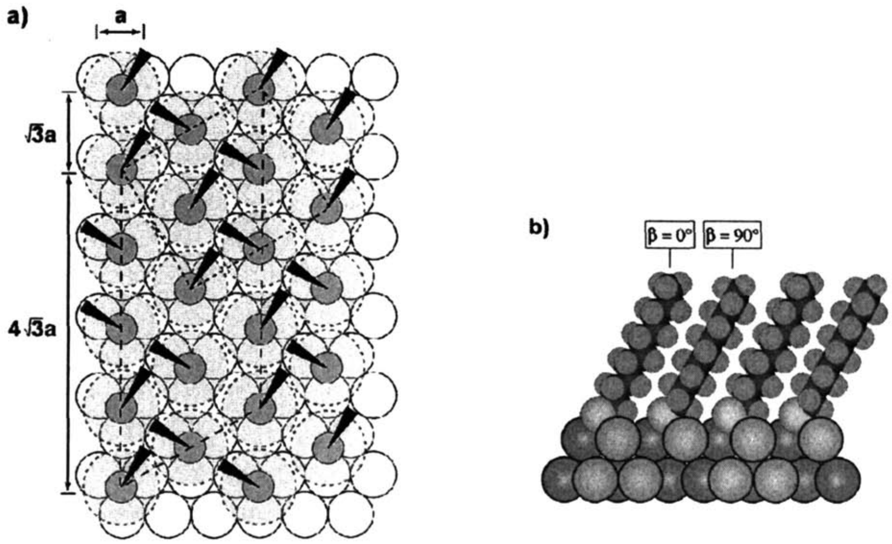

Figure 1.4 Schematic diagram depicting the monolayer arrangement of decanethiolates on Au(111) (a) Structural model of the commensurate adlayer formed by thiols on the Au(111). The arrangement shown is a ($\sqrt{3}\times\sqrt{3}$)R30° structure where the sulfur atoms (dark gray circles) are positioned in the 3-fold hollows of the gold lattice (white circles, $a = 2.88$ Å). The light gray circles with the dashed lines indicate the approximate projected surface area occupied by each alkane chain; the dark wedges indicate the projection of the CCC plane of the alkane chain onto the surface. Note the alternating orientation of the alkane chains defines a c(4 × 2) superlattice structure. The formal c(4 × 2) unit cell is marked (long dashes); an equivalent $2\sqrt{3} \times 3$ unit cell is marked by lines with short dashes. The alkane chains tilt in the direction of their next-nearest neighbors. (b) Cross-section of the SAM formed from decanethiol. Note the alternating rotations of the carbon chains in this view. The chains are labeled with twist values to indicate the relative orientations of the neighboring chains. Love, J. C.; Estroff, L. A.; Kriebel, J. K.; Nuzzo, R. G.; Whitesides, G. M. *Chem Rev* 2005, *105*, 1103-1169.

The nature of the formation of the Au-S bond and the subsequent fate of the hydrogen are subjects of great contention. In general, the reaction is considered to be the oxidative addition of the S-H bond to the gold surface, followed by a reductive elimination of the hydrogen.[49] When a clean gold surface is used, the proton likely ends up as a H_2 molecule—this can be deduced from the fact that monolayers can be formed from gas phase, in the complete absence of oxygen: [51, 52]

$$\text{R-S-H} + \text{Au}_n^0 \rightarrow \text{R-S}^-\text{Au}^+ \bullet \text{Au}_n^0 + \frac{1}{2}\text{H}_2$$

or, equivalently:

$$\text{RSH} + \text{Au} \rightarrow \text{RSAu} + \text{H}^\bullet$$

The Au-S bond is reasonably strong and estimated to be on the order of 40-50 kcal/mol.[13, 35, 36] The bond dissociation energy for the RS-H bond is ~87 kcal/mol[53], and that for $2H \rightarrow H_2$ is -104 kcal/mol.[54] Thus the total reaction has a heat of formation of ~-5 kcal/mol.

The short-range attractive van der Waals (VDW) interactions between the alkyl back bones dominates the packing structure, as discussed above, with the chains assuming a tilt angle of ~30° in order to interlock with their neighbors.[50] The intermolecular interaction between ligands in dense monolayer films has a calculated interaction energy of ~1.4-1.8 kcal/mol per CH_2.[55] Although SAMs tend to be highly crystalline, at room temperature there are a significant proportion (~5-10%) of gauche defects at the chain termina, the total amount being a function of the free volume available at the end group.[56] The organization at the endgroups can be controlled by the formation of H bonds, as in the case of -OH groups, or be restricted by the size and shape of the functional group (OH vs COOH or SO_3H).[49] The final organization of the monolayer is the result of an interplay between substrate-molecule interactions, molecules-molecule interactions (e.g. electrostatic and VDW forces), as well as intramolecular interactions (e.g. bond stretches, angle bends, and torsions).[49]

1.7.2. Place exchange

One particular hallmark of thiolated SAMs is their ability to undergo place exchange. Due to the similarity in energy between the adsorbed and desorbed states, the molecules are in a dynamic equilibrium between the two. This results in the ability to form highly ordered monolayers due to the reversibility of the adsorption process as well as to incorporate new molecules into the monolayer through the addition of new ligands into the place-exchange solution. Place exchange occurs rapidly (minutes-hours) at grain boundaries, defects, and regions of disorder in the SAM; however, the replacement of molecules in dense, crystalline regions on the flat Au(111) terraces is slow (days).[57-59] This is due to the lower organization of the chains at defects and boundaries as compared to (111) terraces. There is an increased intermolecular interaction between ligands on the terrace with a calculated interaction energy of ~1.4-1.8 kcal/mol per CH_2 group in dense monolayer films; this results in an increased barrier to desorption and hence lower place exchange rate.[55] Also there is a lower average coordination numbers for Au atoms at grain boundaries—increasing the probability that Au-thiolate complexes could desorb.[55, 57, 60, 61] The composition of the resulting SAM is dependent on the concentrations and chemical functionalities of thiols in solution, the number of defect sights in the initial SAM and underlying substrate,[55] as well as the immersion time in the thiol solutions (as the time to reach equilibrium is on the order of days to weeks).[61]

The mechanism of place exchange is largely under contention. The first point of uncertainty is the role of hydrogen in desorption of ligands from the Au surface. The second point is the competition between thiol desorption and disulfide desorption.[62] We can write the two forms of thiol desorption as: [53]

$$2RSAu+H_2 \rightleftharpoons 2RSH+2Au \quad (i)$$

$$2RSAu \rightleftharpoons RSSR+2Au \quad (ii)$$

In the case of reaction (i), the energy of desorption , as calculated above, is ~5 kcal/mol.

For the case of reaction (ii), the reaction to form RSSR involves the breakage of two RS-Au bonds (40 kcal/mol each) and the formation of a RS-SR disulfide bond (~74 kcal/mol for disulfide bond cleavage.[53] This gives a heat of reaction of ~+6 kcal/mo, comparable to that of reaction (i),and suggesting that both mechanism take place. Note that the reaction shown in (ii) requires no hydrogen to proceed, and so is suggested to be the dominant desorption method in the absence of hydrogen.[62] Furthermore, there has been some debate as to which mechanism is dominant under solution conditions at RT, with several authors attaining conflicting results.[63] .

1.7.3. 'Mixed SAMs'

Mixed self-assembled monolayers of alkanethiolates are composed of two or more types of ligands formed either directly from a solution containing a mixture of ligands or sequentially by immersion in different thiol solutions, using place exchange to incorporate the new ligands. However, it should be considered that sequential immersion is likely to incorporate the new thiols at defect sights first, while simultaneous immersion will produce a more homogeneously dispersed monolayer.[61] Mixed alkylthiol SAMs tend to show similar monolayer ordering as their homoligand counterparts. The mole fraction of a specific adsorbate in the SAM reflects, but is not necessarily the same as, the mole fraction of the adsorbate in solution through all ranges of concentration. Indeed, Whitesides and coworkers have suggested that mixed self-assembled monolayers formed at room temperature are not at equilibrium with the solution due to the slow rate of exchange between thiols in solution with those at the surface, and equilibrium can only be achieved through SAM formation at higher temperatures (e.g. >60 °C).[61] Furthermore, experimental conditions can bias the relative ratio of the molecular components constituting the SAM;[61, 64] for example, the choice of solvent can modify the relative mole fractions of adsorbates in SAMs formed from a mixture of polar and nonpolar molecules.[65-67]. Similarly, mixtures of *n*-alkanethiols with different chain lengths will form SAMs with a composition enriched with the longer alkanethiol, with the bias increasing over time due to increased stability through interchain interactions.[68] Thus, as discussed above for place-exchange reactions in SAMS, the composition of the resulting mixed SAM is dependent on the concentrations and chemical functionalities of thiols in solution, the number of defect sights in the initial SAM and underlying substrate,[55] as well as the immersion time in the thiol solutions (as the time to reach equilibrium is on the order of days to weeks).[61]

1.7.4. Phase separation in mixed monolayers

For certain mixtures and ratios of ligands, it has been shown that the molecules can form phase separated domains.[59, 69-72] Although there had been some evidence that inhomogeneities in composition existed in the monolayer from XPS measurements and theoretical calculations, it was not until the advent of scanning probe microscopies that these domains could be directly observed.[59] Formation of the domains is temporal, with domains forming over the period of minutes to days depending on the degree of chemical difference between the molecules.[55, 59, 61] Typically, phase separation occurs for ligands with different functional groups and lengths and when one type of ligand is not in far greater excess of the other. Formation of phase separated domains occurs due to the competing energies of enthalpy and entropy—ligands maximize their enthalpic interactions by packing next to ligands of similar height so as to interlock their backbones, while entropy encourages mixing of the different ligands. However, phase separation can be thwarted though judiciously choosing different ligands which, although chemically different, interact strongly. There is some debate as to whether phase separated domains represent the true equilibrium state of the SAM.[61] The establishment of total equilibrium of the SAM is complicated by at least two types of equilibria: (i) equilibrium within the SAM of a mixture of ligands at a fixed composition, and (ii) equilibrium between the SAM and the solution. Folkers suggests that in the formation of domains from an initially mixed two component monolayer, isolated domains represent single phase, single component 'near-equilibrium' regions in a sea of a different average composition, with the 'near-equilibrium' regions forming near step edges and defects where place exchange can occur quickly.[61] Similarly, Stranick et al. studied the evolution of phase-separated domains using STM as well as Time of Flight Secondary Ion Mass spectrometry (TOF-SIMS), noting that TOF-SIMS lacks the resolution to distinguish domains below 50 nm.[59] Mixed monolayers were formed by immersing the Au substrate in to a 1mM solution of thiols for 4 days. Stranick postulates that the formation of domains results from the system evolving from a highly mixed, high energy configuration (due to the large number of interface interactions) towards a lower energy configuration by reducing the interface length and hence energy through the growth of increasingly larger domains. Interestingly Stranick found that for different compositions of the same molecules, different domain morphologies were observed. For example, in a 1:1 mixture of $SH\text{-}(CH_2)_{15}CH_2\text{-}OH$ and $SH\text{-}(CH_2)_{15}CH_2\text{-}CN$, the domains were highly connected, but narrow with a width of ~4-5 nm (Figure 1.5). Similarly for a 1:3 mixture the domains were also nearly continuous; however, for the complementary 3:1 mixture, no extended, continuous domains were seen. This difference is attributed to the larger intermolecular attraction between $-CH_2\text{-}CN$ groups than $-CH_2\text{-}OH$ groups.

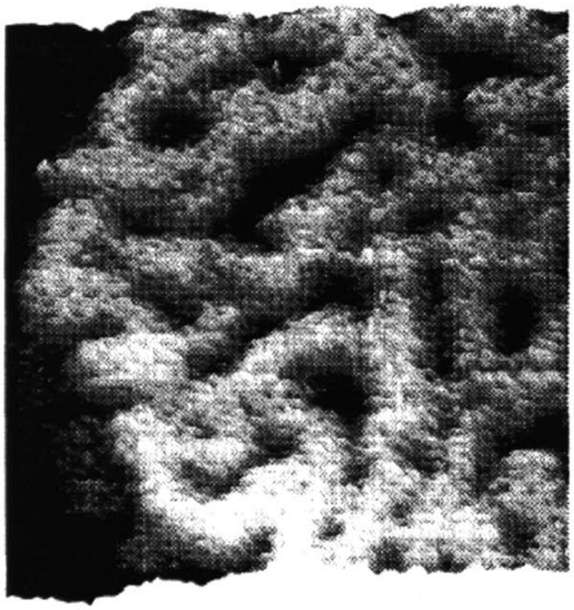

Figure 1.5 STM height image showing a 4.5 x 4.5 nm area of a phase-separated domains within a SAM composed of a 1:1 ratio of $SH\text{-}(CH_2)_{15}CH_2\text{-}OH$ and $SH\text{-}(CH_2)_{15}CH_2\text{-}CN$ on Au(111). The image was obtained with a tunneling current of 2 nA and a tip bias voltage of -2V. The vertical scale shows a 3 Å range in topography. On the left side of the image is a monatomic height step in the Au substrate. Taken from: Stranick, S. J.; Atre, S. V.; Parikh, A. N.; Wood, M. C.; Allara, D. L.; Winograd, N.; Weiss, P. S. *Nanotechnology* 1996, *7*, 438-442.

1.8. Characterization of the nanoparticle core

Because nanoparticles can be treated as a large molecular species, they can be characterized using a large range of techniques not available to bulk materials. The core structure and properties of nanoparticles has typically been the focus of most nanoparticle characterization studies. TEM is the most common characterization tool as it allows for the visualization of the crystalline core from which one can determine the size dispersity of the sample, amount and structure of single crystalline cores, as well as aggregation behavior. Direct observations of individual nanoparticles are difficult. High-resolution transmission electron microscopy (HRTEM) can resolve atomic planes in nanoparticles and has been used extensively to investigate structural defects in larger particles.[73] However, the high energy electron flux that HRTEM needs to obtain images strongly excites small particles and thus may not reflect the true structure; in fact a distinct "quasimolten" state has been observed.[74] Both for this reason, and because there are difficulties in interpreting images of very small particles, HRTEM is of limited use in determining the structure of particles less than ~3 nm in diameter. Further complicating analysis of the core structure is the fact that often nanoparticles >3 nm contain a large number of defects making crystal structure characterization difficult.[33] Additionally, tools such as small angle x-ray scattering (SAXS) and x-ray diffraction (XRD) can be used for observing the crystal structure of the core as well as any order that might be present in the packing arrangement between nanoparticles.

For the Schiffrin method of synthesis of gold particles, the cores tend to range from 2-6 nm in diameter with an average of ~ 4 nm and are typically single crystalline. It has also been noted that due to the large ratio of surface to volume, core shapes tend to be a function of size.[75] For particles with a diameter of less than 2 to 3 nm, the predominant shape is icosahedral. As the core increases in size, the truncated dodecahedral shape becomes dominant, and for particles larger than 4 nm the truncated octahedral shape is the most common (see Figures 1.6 and 1.7 for examples of various core shapes).[33, 76] SAXS and computation studies have revealed that there is a slight contraction (5%) of the gold lattice as compared to the bulk due to increased surface energy.[77, 78] TEM has also revealed that the clusters tend to form ordered 2-D and 3-D aggregates, which are increasingly prevalent with decreasing polydispersity of the sample.

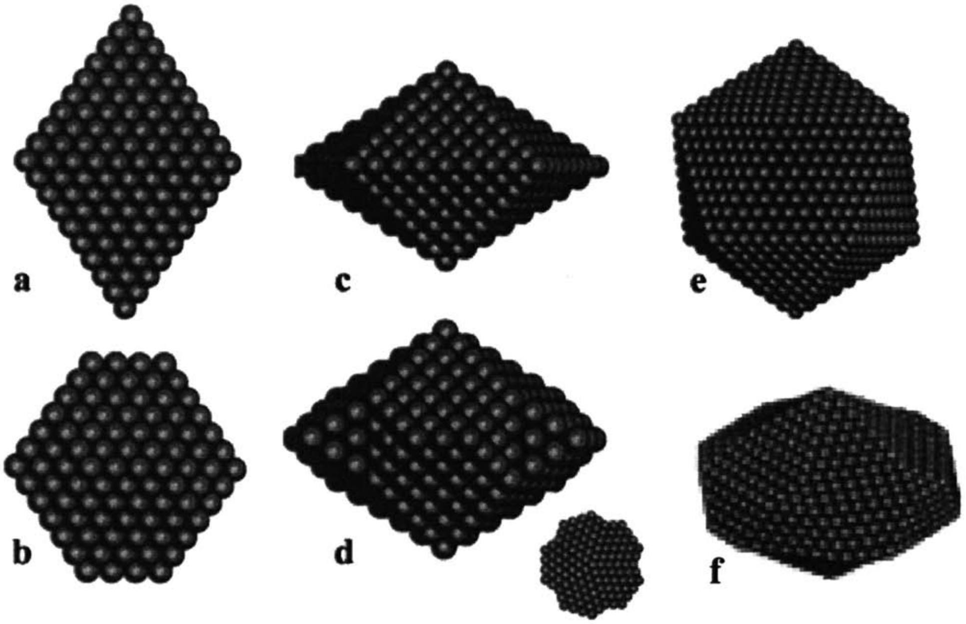

Figure 1.6 (a) The three most common shapes of metal nanoparticles observed. (a) The fcc octahedron (O). (b) The truncated octahedron (TO). (c) The regular decahedron. (d) The truncated decahedron (D_h). (e) The icosahedron structure (I_h). (f) The truncated icosahedron (TI) Image Taken from: Ascencio, J. A.; Perez, M.; Jose-Yacaman, M. Surf Sci 2000, 447, 73-80.[79]

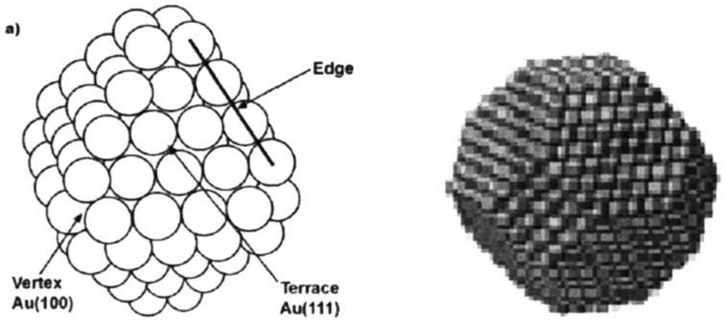

Figure 1.7 Model of an Au_{140} (left) and Au_{1289} (right) nanocluster with truncated octahedral geometry. Note the increase in the number of edge sights with increasing nanoparticle size. (left)Taken from Love, J. C.; Estroff, L. A.; Kriebel, J. K.; Nuzzo, R. G.; Whitesides, G. M. *Chem Rev* 2005, *105*, 1103-1169. (right) Taken from Luedtke, W. D.; Landman, U. *J Phys Chem B* 1998, *102*, 6566-6572.

1.9. Characterization of the nanoparticle ligand shell

Characterization of the ligand shell packing and conformation has proven to be more difficult than that of the core. This is due to a variety of factors such as the small ratio of ligand to metal for each particle leading to small signals, as well as the inherent polydispersity of nanoparticle samples combined with the fact that most techniques provide only ensemble averages, tending to smear out most results. Additionally, the high amount of edge and corner sites of the core may result in different packing environments for ligands depending on location—on a 1-2 nm Au particle, ~45% of surface atoms are located on edges or corners—further complicating particle data.[56] The methods of characterization range from spectroscopies such as Fourier Transform Infrared Spectroscopy (FTIR),[56, 80] Nuclear Magnetic Resonance (NMR),[80, 81] and UV-Vis to microscopies such as Atomic Force Microscopy (AFM) and Scanning Tunneling Micrscopy (STM)[82] (both of which provide single particle data) to Thermal Gravimetric Analysis (TGA), Differential Scanning Calorimetry (DSC),[80] Elemental Analysis, as well as reactivities[83] of the ligands and metallic core.[13, 80-82]

It has become evident recently that 3-D SAMs have many differences as compared to their well-studied 2-D counterparts. This was not totally unexpected due to the high degree of defect-like sites (edges and corners) as well as curvature (in a topological sense) of the gold core which leads to a radial density gradient in free volume from the core surface to ligand endgroups. One of the most significant differences is that the packing density of ligands on nanoparticles (defined as the number of ligands per surface gold atoms) is 50% or more depending on core size (as determined using a combination of TGA and core size analysis from TEM[34]), much greater than the 33% percent density observed for flat monolayers (this is derived easily since each sulfur atom sits at a 3-fold hollow site, giving 1 ligand per 3 gold atoms—equal to 1/3 or 33%). Two possible explanations for the increased density have been suggested: 1) the ligands assume a much tighter packing (smaller sulfur-sulfur spacing) around the core afforded by the increased free volume of packing for head groups, with the sulfurs occupying off-hollow sites—a behavior not generally seen for 2-D monolayers; or 2) the larger coverage could also be explained assuming 33% coverage on the crystalline facets (with the ligands packing at traditional 3-fold hollow sites with a spacing equivalent to 2-D monolayers) and 100% coverage at the facet edges with 1 ligand per atom.[82] Using NMR spectroscopy, it has been concluded that the chemisorbed species on the gold nanoparticle surface is most probably a thiolate, not a disulfide, given the similarity in the ^{13}C chemical shifts of the Au/SR colloids and Au(I) alkylthiolates.[84] However, NMR has also demonstrated that there is a wide range in binding sites to which the ligands are attached, indicating that thiols are not in equivalent sites. To date it has not been conclusively proven which model correctly describes the ligand arrangements; theoretical models and their results regarding these two models are discussed below.

1.9.1. Reactivity studies

As discussed above, due to the high radius of curvature of the nanoparticles, there is large increase in free volume in the ligand shell as one moves radially from the core , resulting in increased volume for headgroup packing. The model of tight sulfur-sulfur packing accompanied by decreasing chain packing density radially from the core, is supported by numerous ligand reactivity studies.[83, 85, 86] Templeton probed the S_N2 reactivity of mixed monolayer ω-bromoalkanethiolate (either $C_{12}Br$, C_8Br, or C_3Br) and dodecanethiol (C_{12}) functionalized nanoparticles with primary amines (n-propyl, isopropyl, and tert-butyl). It was found that the extent of reaction was highly related to the steric bulk of incoming nucleophiles as well as to the relative chain lengths of the ω-bromoalkanthiolate and the surrounding alkanethiolates chains. For example, nucleophilic reactions occur easily and rapidly on $C_{12}/C_{12}Br$ nanoparticles, but only under vigorous conditions for a C_{12}/C_3Br particle, suggesting that the C_3Br was partially 'blocked' by the surrounding $C_{12.}$ Interestingly, the authors found that the reactivities of functional groups at the chain ends ($C_{12}Br$) were nearly equivalent to those for monomers in solutions, indicating that the endgroups are not as tightly packed nor as confined as they would be in a 2-D monolayer. It should also be noted that although reactions on C_{12}/C_8Br and C_{12}/C_3Br nanoparticles did not occur as facilely as on $C_{12}/C_{12}Br$, the reactions were able to be driven to almost complete conversion with longer reaction times and elevated temperatures indicating that the ligand shell is not as sterically hindered as for 2-D SAMs and contains a significant amount of free volume.

The susceptibility of differently protected gold cores to a cyanide etchant can also give an indication of the density of packing of the alkanethiolates in the SAM. Cyanide causes the dissociation of the monolayer with concomitant etching of the gold substrate—the rates of decomposition can then be correlated to the extent to which the monolayer protects the core. Templeton used cyanide-mediated decomposition of the core to show that the rate depends on the steric aspects of the monolayer, slowing with increased chain length and bulkiness.[83] However for all chain lengths $>C_{10}$, NaCN decomposition rates are constant, consistent with the picture that close to the core, within 10 C-C chain lengths in this case, the ligands are ordered and packed tightly, but then beyond this length, the chains are liquid like and much less tightly packed.

1.9.2. Hydrodynamic radii measurements

Measurements of the hydrodynamic radii of monolayer-protected gold nanoparticles support the hypothesis that the outer part of the thiol layer is loosely packed.[87] A nanoparticle coated with a well-packed SAM is expected to have a hydrodynamic radius equal to the sum of the radius of the gold core and the fully extended alkanethiolate. This expectation does not, however, match experimental results. Murray and coworkers studied nanoparticles with decanethiol, C_{10}, dodecanethiol, C_{12}, and tiopronin monolayers in a variety of solvents. The authors measured the hydrodynamic radii by studying the spreading of a plug of nanoparticle solution injected into a slowly moving solvent stream. All measured hydrodynamic radii of the monolayer-protected gold nanoparticles are smaller than predicted by assuming an all trans-ligand chain, suggesting that the monolayer is not well packed along the outer edge. The inference then is that the outer portions of the alkanethiolate chains are extensively penetrated by and are "free draining" of solvent and have substantial disorder--a picture consistent with spectroscopic[56] and chemical reactivity[83] studies indicating that the alkanethiolate chains are liquid-like.

1.9.3. Place exchange studies

Similar to flat 2-D monolayers, the ligand shell of gold nanoparticle can undergo place exchange to introduce new functionalities into the ligand shell. Indeed, place exchange studies on nanoparticles are often used as a model for exchange in 2-D systems due to the broader range of characterization techniques available for 3-D monolayers on particles.[34, 80-83, 88, 89] The process of place-exchange is thought to be an associative one, with an incoming thiol attaching to the surface and a bound ligand leaving simultaneously.[34, 83, 88, 89] Murray extensively studied the dynamics of place exchange using octanethiol (C_8) coated Au_{314} nanoparticles exchanged with benzylthiol, using ^1H NMR spectroscopy.[88] The authors found that the rates of place exchange depend on the concentrations of entering and exiting ligands, with a 1:1 reaction stoichiometry, and detected no presence of disulfide—indicating that ligands did not leave in pairs. They conclude that the mechanism is that an entering ligand protonates a bound thiolate which then leaves, allowing the entering ligand to be incorporated into the monolayer. This conclusion agrees with their observations of decreasing place exchange rates with both increasing bulkiness of the entering ligand and increasing length of the initial monolayer ligands.

Additionally, the resultant ligand shell composition after place-exchange and how and what factors (e.g. concentration, time, particles size) determine such composition is still not well understood. In order to study the final equilibrium composition of place exchanged particles, Hostetler and coworkers performed place-exchange reactions in which they varied the ratio of incoming thiol ($MeO_2CC_{11}SH$) to ligand shell thiols (C_4, C_8, C_{12}, or C_{16}), noting the number of incorporated $MeO_2CC_{11}SH$ into the ligand shell with ^1H NMR.[88] The authors found that, except for very low (i.e. 1:20) ratios of incoming ligand:ligand shell thiols, the final amount of place exchanged thiol was well below, ~60-70%, that estimated for the case in which the reaction showed no selectivity between entering and exiting ligands. The authors argue that this result supports the theory that there is a strong gradation of surface site reactivity on the nanoparticles with highly active sites which are exchanged immediately and less active sites which have much longer time scale for place exchange. Hostetler notes that even after five days, the reaction may not lie at a true equilibrium. Furthermore, even under strong reaction conditions (e.g. high temperature) C_{12} and C_{16} protected nanoparticles will not fully place exchange, retaining ~20% of their original monolayer. The authors conclude that chain-chain interactions are significant factors in the stabilization of the monolayer and that while edge and vertex sites on the core may react quickly due to few intermolecular interactions, ligand on terrace sites are very slow to exchange due to the numerous interactions.

The use of place exchange studies has also illuminated key features of the formation and structure of the ligand shell around nanoparticles. Specifically, Chechik, using EPR spectra combined with GPC separations, found that the rate of place exchange decreases significantly with the age of nanoparticles.[90] Aging nanoparticles for tens of hours in solution after synthesis resulted in severely limited rates; however, the total number of ligand exchanged was unaffected. Using a combination of TEM and UV-Vis he concluded that the differences in reactivity with time were due to the reorganization of the particle surface through the annealing or stabilization of defect sights.

Additionally, Chechik[68] as well as Murray[88, 91, 92] have found a compositional dispersity in the amount of place exchanged ligands on a nanoparticle. In a first set of experiments, Hostetler and Murray et al. used a modified version of HPLC along with thin layer chromatography (TLC) to examine the place exchanged product of C_{12} coated nanoparticles exchanged with $HOC_{11}S$. Using NMR, it was determined that there was, on average, ~10 $HOC_{11}S$ ligands per particle. However, when the as reacted particles were then subjected to HPLC and TLC experiments, the particles became separated into two fractions containing (as determined through NMR) 6 exchanged ligands (37% of the product) and 17 exchanged ligands (52%). The authors note that the dispersity in the exchange number matches the dispersity in core size, suggesting that the number of ligands exchanged is a function of core size and thus perhaps core shape. Similarly, and more conclusively, in a later set of experiments Murray and coworkers demonstrated a similar result examining the place exchange of hexanethiol (C_6) Au_{140} particles with ferrocenyl octanethiol (HSC_8Fc). The authors use reversed phase HPLC (RP HPLC), which relies on the interaction between a nonpolar stationary phase and the ligand shell of the nanoparticles, augmented with dual detector method that determines nanoparticle core size through the ratios of optical absorbance and electrochemical currents (through fast scan cyclic voltammetry). Thus the method allows for simultaneous measurement of ligand shell composition and core size. The authors first size fractionated the C_6 coated particles (giving ~1.7 nm particles) and then place-exchanged these with HSC_8Fc. Using ^1H NMR, it was found that the ratio of place exchanged ligands to hexanethiolate ligand in the mixed ligand shell was 9:44. However, when this exchanged product was examined with the augmented RP HPLC it was found that the particles were polydisperse in composition, eluting at different times with either ~33, 7, or 5 ferrocenyl ligands per particle. Further analysis revealed that the particles which contained 33 ferrocenyl groups were actually Au_{79} (not Au_{140}), which have only ~38 ligands in its monolayer, indicating that the particle underwent complete exchange. The authors conclude that place-exchange reactions result in polydisperse products, the total amount of ligand exchanged depending on core size. Given that particle size and structure are generally related, this suggests a dispersity of binding sights on a nanoparticle, each with different reactivities, the amounts of which vary with particle size.[88] More specifically, it is postulated that the variations in the number of edge and vertex sites for different shapes of particles leads to a dispersity of binding sites on the particle due to steric constraints (from surrounding) ligands and reactivity of the Au surface atoms.

In a supporting work by Chechik and coworkers,[91] the partial place exchange of triphenyl phosphine protected Au particles (~2 nm in diameter) with spin labeled disulfides was examined using electron paramagnetic resonance (EPR) spectroscopy with gel permeation chromatography (GPC). After reacting the particles with the disulfide in a 20:1 (incoming disulfide:triphenyl phosphine) ratio, the particles were fractionated using GPC and the number of exchanged ligands examined. It was found that the particles separated into 3 fractions, each with a different number of exchanged ligands. However, because GPC depends on a convolution of both the core size as well as ligand shell, it could only be concluded that the reaction had resulted in a polydisperse product and no conclusions could be drawn on the effect of core size and shape.

Recently, Rotello and coworkers have found that the steric nature of ligands affects, in a non-intuitive way, the rate of place exchange. The authors demonstrate using fluorescently labeled thiols that linear thiols are more efficient at place exchanging than branched thiols whose branching point is at the C adjacent to the thiol, as would be expected from steric considerations.[85] However, if the branching point is displaced from the sulfur group by at least one carbon, it has a larger activity of place-exchange than a linear thiol of the same length (Figure 1.8). The authors suggest that branched thiols may pack better than linear ones due to their 'cone' shape which allows for increased interactions between, and hence stabilization of, the surrounding monolayer (Figure 1.9).

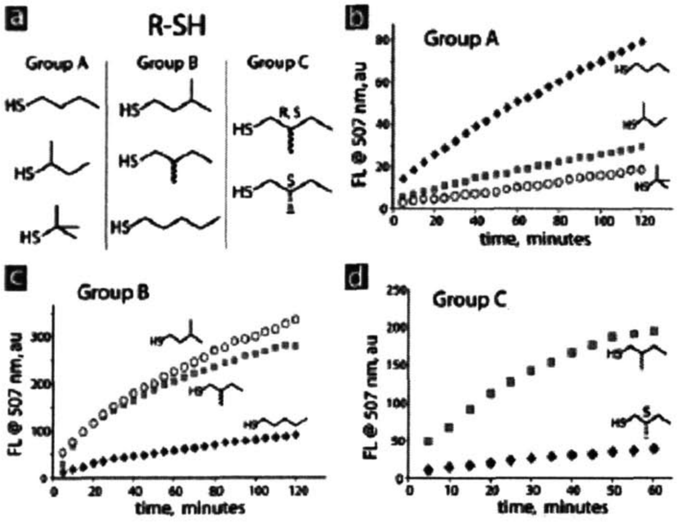

Figure 1.8 Effect of the steric nature of incoming ligands on place exchange. (a) Chemical structure of thiol ligands. (b), (c), and (d) Plot of degree of place-exchange (as measured by the fluorescence intensity of exchanged ligands in solution) with time of dye-labeled nanoparticles for various incoming thiol structures. The fluorescence intensity at 507 nm was plotted against reaction time. Taken from: Hong, R.; Fernandez, J. M.; Nakade, H.; Arvizo, R.; Emrick, T.; Rotello, V. M. *Chem Commun* 2006, 2347-2349.

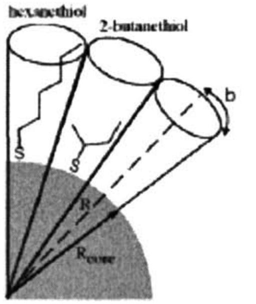

Figure 1.9 Schematic representation of a gold nanoparticle protected with branched and unbranched alkanethiolates. A cone can be drawn that encompasses the area available to each chain on a nanoparticle with a given diameter; the alkyl chain completely fills the volume of the cone at the surface of the nanoparticle but is unable to fill the larger end of the cone. Note that the branch thiolated more effectively fills the conical packing space. R is the radial distance, and b is the half-angle of the conical packing constraint. Taken from: Love, J. C.; Estroff, L. A.; Kriebel, J. K.; Nuzzo, R. G.; Whitesides, G. M. Chem Rev 2005, 105, 1103-1169.

1.9.4. FTIR studies

Several authors have further investigated the nature of the surrounding monolayer in regards to ligand conformation and packing by using infrared spectroscopy to probe the structure. The choice of FTIR is especially relevant, since reflection-absorption infrared spectroscopy (RAIRS) has been one of the principal tools in understanding the structure of the alkanethiolate chains on 2D-SAMs.[93] Both Murray and coworkers, using ligands of varying lengths,[56] as well as the group of Lennox and coworkers, using specifically deuterated and perdeuterated octadecanethiols,[80] have been able to deduce much amount the ligand conformation and chain defects (Figure 1.10). They found that the majority of the alkanethiolate ligands are in an all-trans zigzag conformation with the concentration of near core surface defects within the 3D-SAMs similar to, although ~5% higher than, those of alkanethiolates on flat gold surfaces.[56] For example: for C_3 and C_4 coated nanoparticles, they found ~30% near surface defects; C_5-C_{12}, ~20%; C_{16}-C_{24}, ~10%. Additionally, there is a significant concentration (10-25%) of chain end-gauche defects in which the outer CH_2CH_3 group lies gauche to the rest of the chain, the relative amount of which increases with increasing chain length. This is more than the estimated 5-10% density of these defects in 2-D SAMs,[56] and supports the model of increased free volume for and significant mobility of the chain end-groups. Overall, it was noted that smaller chain lengths (C_3, C_4, and C_5) are relatively disordered, with large amounts of gauche defects present, and thus most resemble free alkanes in the liquid state. The longer length alkanethiolates are predominantly in the all-trans zigzag conformation. Templeton further supports this conclusion by comparing the FTIR spectra of the particles in solution as compared to those in the solid state and the monomer, and finds that the solvated ligand shell exhibits a chain conformation that is highly disordered as compared to the solid state—indicating a more 'liquid' like conformation reminiscent of liquid alkanes.[83]

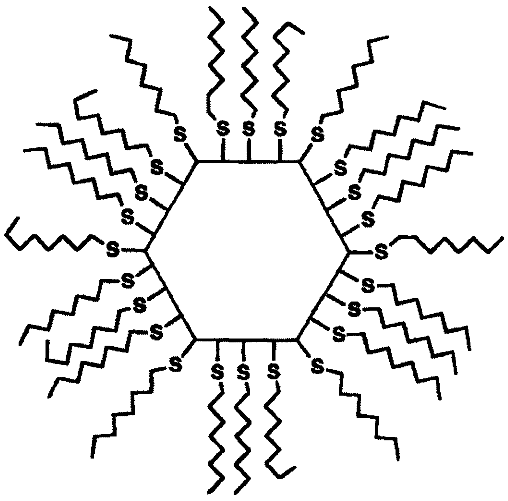

Figure 1.10 Schematic representation of a Au nanoparticle illustrating the types of defects observed in the surrounding ligand chains. Taken from: Hostetler, M. J.; Stokes, J. J.; Murray, R. W. *Langmuir* 1996, *12*, 3604-3612.

In order to elucidate the packing structure of ligands surrounding the metal core, Rotello and coworkers looked at hydrogen bonding in amide functionalized alkanethiolate coated nanoparticles in which the position of the amide moieties was varied along the length of the chain.[94] Spectroscopic data showed that intramolecular hydrogen bonding between adjacent amides substantially decreases with increasing distance from the particles surface; indicating the radial nature of the packing ligands with each located within a 'cone-shaped' region of space. In a related study, Rotello and co-workers formed monolayer protected Au nanoparticles using alkanethiols functionalized with a variety of amides and esters with branched end groups. The authors evaluated the strength of intramonolayer hydrogen bonding as a function of endgroup steric bulk, using FTIR, and the corresponding stability of the monolayer-protected particles to cyanide etching.[86] The authors found that while extremely bulk groups lead to decreased hydrogen bonding between chains, moderately bulky end groups lead to an increased hydrogen bonding ability due to space filling and monolayer surface packing. This correlates with the observed CN^- induced decomposition of the particles in which the lowest decomposition rates were associated with the largest degree of intermolecular interactions. They hypothesized that "cone-shaped", branched molecules would more effectively occupy the volume available at the outer edge of the monolayer than simple *n*-alkanethiolates, which have a linear geometry when extended in an all-trans conformation (Figure 1.9).

1.9.5. Chain ordering and disordering with temperature

The temperature-dependent phase behavior and dynamics of SAMS are intimately related to their conformational order[95] Due to the comparable size of the metal core and chain length as well as the highly curved geometry of the metal core, how chain ordering arises is not well understood. Order-disorder transitions of the ligand shell have been studied using differential scanning calorimetry (DSC), variable temperature IR and NMR spectroscopies, as well as variable temperature neutron scattering experiments.[80, 96] All clusters with chain lengths of more than C_8 show a broad endotherm in DSC at 330 K, indicating a phase transition.

1.9.5.1 DSC and FTIR studies

Ligand shell melting transitions, and their associated temperatures and heats of enthalpy, are believed to reflect the formation of crystalline alkanethiolate domains on the cluster surface and/or the interdigitation of domains on adjacent particles. Lennox and coworkers examined ligand shell phase transitions on nanoparticles using variable temperature FTIR to study the increase in gauche defect concentrations with melting and found that the melting transition temperatures increase with methylene chain length[81] as do the transition enthalpies indicating increased interchain interactions, and hence packing, with increasing chain length.[80] Furthering this research by combining FTIR and DSC data of 3-D monolayer protected nanoparticles and comparing with 2-D monolayers, Murray found that as the size of the particle increases, the properties of the 3-D SAM become more similar to the 2-D SAM on a planar surface. Particles with a core diameter greater than 4.4 nm, coated with a SAM of dodecanethiolates (C_{12}), have spectroscopic and physical properties approximating that of a planar SAM.[34] This result is supported by DSC studies which found very small SAM melting enthalpies (fewer trans to gauche transitions) for larger clusters, as compared to large heats of melting for small clusters, indicating a highly crystalline monolayer on the larger particles. The authors propose that for 4.4 nm and larger particles, the majority of the surface comprises flat [84] terraces rather than edges and corners, and that this geometry leads to "bundles" of ordered alkanethiolates with gaps (areas with a disordered organic layer) at the corners and vertexes (Figures 1.10 and 1.11)—a configuration also suggested through NMR, TEM, and neutron scattering experiments.[80, 97] These "bundles" have been hypothesized to play an important role in the solid-state packing of nanoparticles into lattices (Figure 1.11). Indeed, combining the FTIR and DSC data with TEM images, Badia suggests that chain ordering arises from the interdigitation of chain domains between neighboring particles, with phase transition temperatures reflecting the extent of the van der Waals interactions between particles.[81]

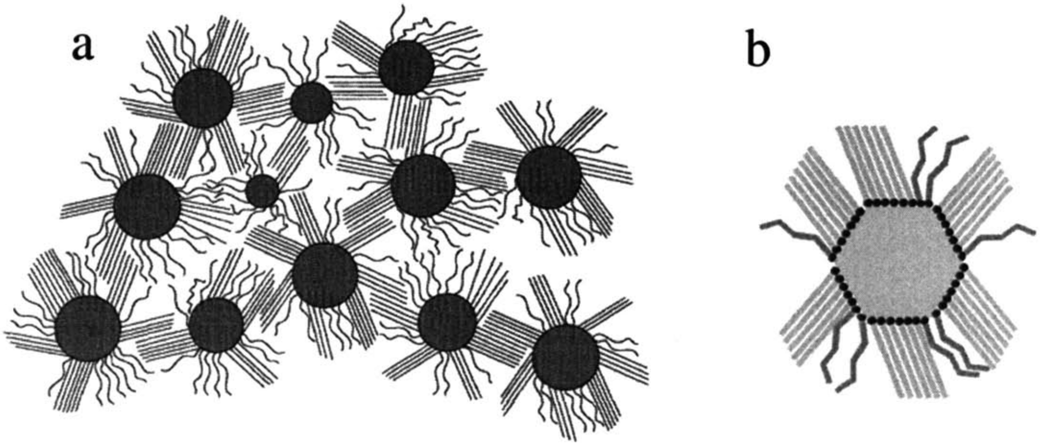

Figure 1.11 (a) A schematic 2-D representation of the Au nanoparticle packing structure in the solid state. As can be seen, crystalline bundles of ligands on the particle interdigitate with one another, resulting in closely packed nanoparticles. (b) Single nanoparticle from (a) showing the faceted nature of the core with crystalline domains on the particle facets and the presence of non-crystalline, mobile ligands at the edges of and in between the bundles. Image taken from: Badia, A.; Cuccia, L.; Demers, L.; Morin, F.; Lennox, R. B. J Am Chem Soc 1997, 119, 2682-2692.

1.9.5.2 NMR studies

^{1}H and ^{13}C NMR are particularly sensitive probes of the structure and composition of monolayers on nanoparticles. IR measurement is essentially a "snapshot" of the different bond conformations existing at a given instant averaged out over the area of irradiation.[35] Thus, while FTIR spectroscopy reveals the equilibrium *trans* and *gauche* bond populations as a function of temperature, it does not provide any insight about the motional processes which accompany chain disordering. For this reason, the long time scale probed by ^{2}H NMR (typically 10^{-6}-10^{-4} s)[35] can be used to study the temperature dependence of the alkanethiolate chain dynamics. Due to its sensitivity to small changes in a molecule's local environment it is particularly well suited to examining changes in packing with temperature. Badia and coworkers studied the reversible chain disordering of ~3 nm particles, coated with deuterated octadecanethiols (C_{18}). Combining NMR with DSC, they attribute the broadness of the DSC peak to a chain-disordering process that is progressive—that is occuring from chain terminus down. At high temperature, these defects progress toward the interior, and after the melting point, both the outer and interior chains appear the same.[31] This is supported by (DSC) and variable-temperature IR and NMR measurements.

1.9.5.3 Neutron scattering experiments

Pradeep and coworkers used variable temperature neutron scattering to study chain dynamics on Au and Ag nanoparticle surfaces.[96] At 340 K and above, quasielastic (QE) broadening is observed in octadecanethiol-protected Au clusters, which is explained due to the melting of the alkyl chain.[96] It has been found that the principal rotational motion of the chains is the uniaxial motion, and that the alkyl chains are held rigidly with an interchain distance of 4.4 Å, suggesting close packing of chains and resulting in a higher packing density than on planar monolayers. [96] While longer chain monolayers (above C_8) on Au clusters are rotationally frozen at room temperature, dynamic freedom exists in lower chain lengths.[98] Examining the evolution of chain dynamics with temperature, the authors found distinctly different behavior for different chain lengths—

for longer chain systems such as C_{12}, the chain dynamics arises abruptly at the melting temperature similar to 2-D SAMs, but for C_6 and C_8, it evolves with temperature. The authors invoke the model of a well packed monolayer on each nanoparticle core facet, with less ordered ligands on edges (Figure 1.11), and the concept of fractional dynamics to interpret their data—that is, only a fraction of the alkyl chains are undergoing motions. In the case of monolayers forming pillars on the surface of the planes, it is expected that the chains on the edges of the monolayer assembly (or the free chains not part of the assembly) will become dynamic first, as they are the ones with less interchain interactions. As they become detached from the bulk monolayer assembly, they acquire dynamical freedom. It is easier for the shorter chain monolayers to detach from the assembly earlier than the longer chains due to fewer intermolecular interactions. In the longest chain systems, the chains are all-trans and completely extended, and as a result detachment may result in a free chain, which is free to be dynamically active.[98]

1.9.6. AFM and STM studies

AFM and STM are currently the only techniques for direct visualization of the entire nanoparticle (core plus ligand shell). Typically the particles are immobilized on HOPG or an alkanethiol monolayer on Au(111). During STM imaging of particles, two tunnel junctions are formed between the tip and particle and between the particle and the surface. In order to pass an electron from the tip to the sample and thus to image the particles, an energy of $E_c=e^2/2C$ is required. One of the first groups to image particles by STM was that by Whetten and coworkers.[99] Gold nanoparticles, ~1.68 nm in diameter coated with dodecanethiol were deposited on highly oriented pyrolytic graphite (HOPG) or Au(111) on mica (Figure 1.12). The researchers found that the particles tended to form close packed aggregates on the substrate. Pileni and coworkers examined the effect of nanoparticle packing on the resulting IV characteristics of dodecanethiol coated, 4.3 nm, Ag particles.[100] For example, while isolated, single particles on Au(111) showed a typical Coulomb blockade at 1 V, a single layer of hexagonally packed particles has an order of magnitude lower current at large biases and a Coulomb blockade which occurs at a reduced bias of 0.22 V. (see Figure 1.13). The change in behavior between isolated and aggregate forms is believed to be due to lateral electron transport between neighboring particles, and thus makes the effective capacitance between the particles and substrate larger.

Terrill and coworkers found that their STM images of nanoparticles on HOPG show a larger diameter than TEM or SAXS, but convolution of the particle size with STM tip may cause and overestimation of the true particle size.[82] However, their size estimates agreed with the experimentally observed hydrodynamic radii. Additionally, Terrill used tapping mode AFM to image the particles on mica and found that the height measurements gave a slightly smaller particle, while lateral measurements gave much broader dimensions, again likely due to tip shape.[82] While STM and AFM imaging of nanoparticles is becoming more widespread, there have been no reports in the literature of attaining molecular resolution of the ligand shell, as there have been for flat surfaces.[59, 64] Indeed, it was not until the advent of AFM and ATM that phase separated domains were able to be confirmed and detected in SAMs.[55, 59, 61]

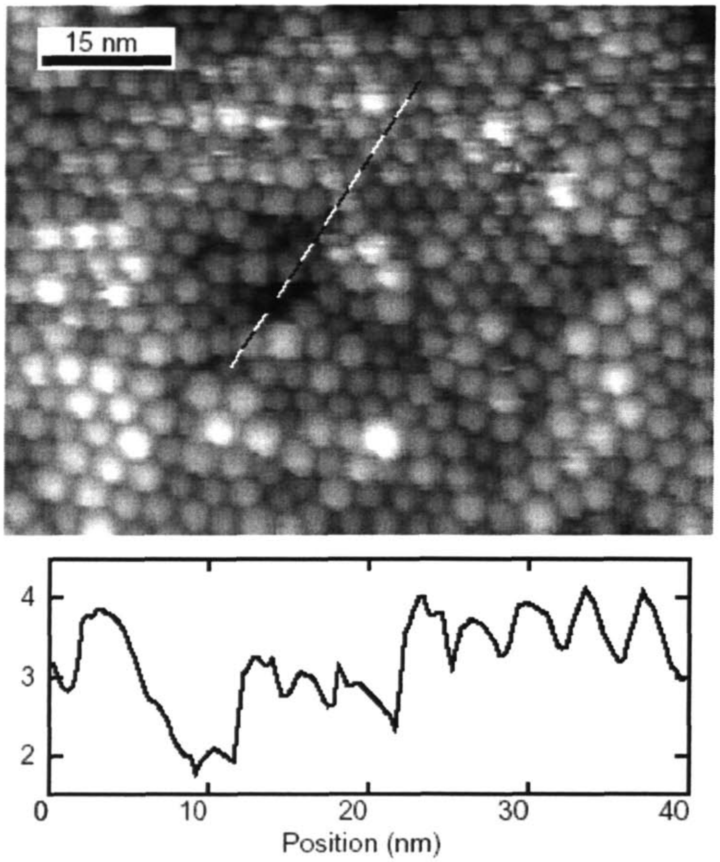

Figure 1.12 Top: STM height image of dodecanethiol coated Au nanoparticles on graphite, in which local ordering of the particles can be seen. Bottom: height profile along the line marked in the top image. Image taken from: Bigioni, T. P.; Harrell, L. E.; Cullen, W. G.; Guthrie, D. E.; Whetten, R. L.; First, P. N. *Eur Phys J D* 1999, *6*, 355-364.

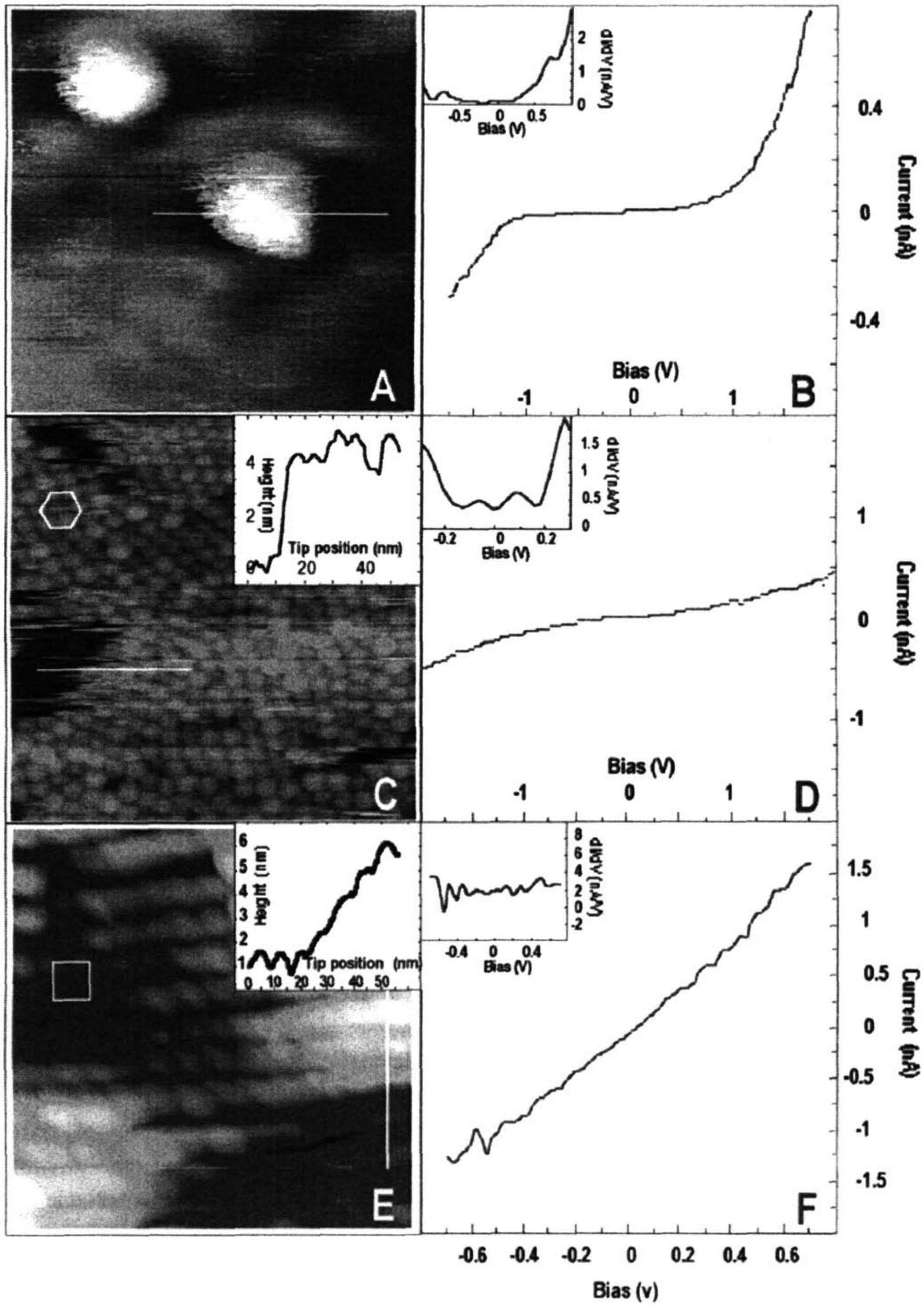

Figure 1.13 Constant current mode STM images of silver nanoparticles with various film morphologies: (a) isolated nanoparticles, (c) double layer of hexagonal close packed film of nanoparticles, and (e) fcc packed particles. (b), (d), and (f) are I-V curves of the various films, repectively. All substrates were Au (111) on mica.

1.9.7. Theoretical studies of ligand ordering on nanoparticles

Although the number of theoretical studies and models of ligand coated nanoparticles are sparse, they are invaluable tools for understanding and probing the thermodynamics and structure of the ligand shell as a function of core size and shape and ligand functionality. Using Molecular dynamics simulations, Luedtke and Landman examined the packing on dodecanethiolate coated Au_{140} (core structure: TO^{+}—truncated octahedron with 4 atoms at the intersecting edge of (111) facets and 2 atoms at an edge adjoining a (111) and (100) facet) and Au_{1289}(core structure: TO—truncated octahedron with 5 atoms along all adjoing facets) gold cores .[97] The authors found that the packing on the (111) and (100) facets of the core differed from those found on extended flat Au surfaces and depend on the size of the core. For $Au_{1289}(C_{12}H_{25}S)_{258}$, the distribution of S-S distances on the (111) facets is broad, with a peak at ~4 Å, and skewed to larger values; the average value from this distribution is 4.4 ± 0.4 Å—smaller than the 4.99 Å spacing found on extended flat Au(111). The distances suggest ~12% contraction of the mean nearest neighbor distance between absorbed sulfur atoms on a planar Au(111) surface, resulting in an ~30% increase in packing density—a result which coincides with that experimentally observed using TGA and TEM by Murray.[34] Additionally, on the (111) facets the sulfurs form a distorted hexagonal lattice, occupying both hollow and bridge sites between the gold surface atoms; the ratio of surface gold atoms to sulfur atoms being 1.87 (as compared to 3 for a flat Au(111) surface), resulting in a packing density of ~53% . On the (100) facets of the nanocrystallite the average sulfur-sulfur distance is 4.1 ± 0.3 Å, with the sulfurs occupying the hollow sites. For $Au_{140}(C_{12}H_{25}S)_{62}$, the distortion of the sulfur lattice is greater, with the inequivalent sulfur-sulfur distances are 3.9 and 4.5 Å (on the (111) facets). The sulfurs bind in the hollow sites of the small (100) facets, and on the (111) facets their arrangement is hexagonally distorted, binding in the middle hollow sites as well as off the hollow sites. The ratio of gold surface atoms to absorbed sulfur atoms is 1.55 as compared to 3 on extended gold surfaces.

Not only did Leudtke and Landman find that the binding behavior of ligands on the core surface differ from that of flat monolayers, but also the packing and thermodynamic behavior of the chains was found to differ significantly. The authors find that below the ligand shell melting temperature, the ligand arrange themselves into preferentially oriented molecular bundles, with more ordered interchain packing seen for large particles (Figure 1.14) . At higher temperatures disordering of the chains occurs and lose their oriented bundling behavior, with disordering occurring from the chain terminus inward—agreeing with the mechanism that has been seen experimentally.[80, 81] Additionally the authors find that it is those chains at the boundaries of the bundle which melt and disorder first upon heating (even below the T_M of the ligand shell)—a result which agrees with that found experimentally by Lennox in variable temperature deuterium NMR studies [80]

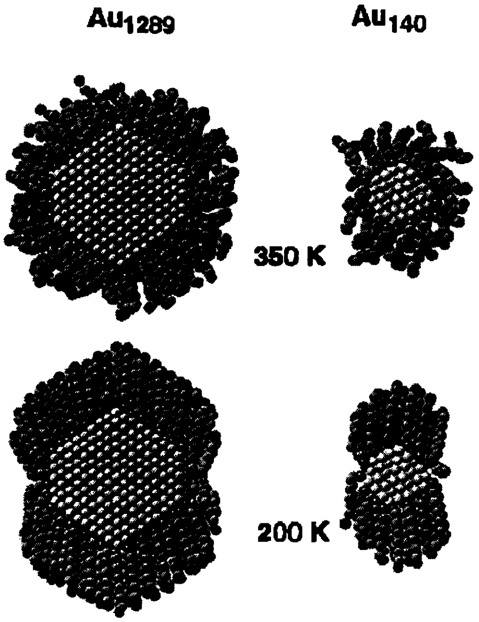

Figure 1.14 Equilibrium configurations of passivated $Au_{140}(C_{12}H_{25}S)_{62}$ and $Au_{1289}(C_{12}H_{25}S)_{258}$, right and left, respectively. The images were obtained via a cut through the cluster. In each case the ligand shell molecular configurations are shown below (T = 200 K) and above (350 K) the chain-melting temperature. The dark grey spheres depict alkyl segments and the lighter ones correspond to gold atoms. Black spheres near the gold nanocrystallite correspond to sulfur atoms, and the very dark grey spheres on the outside periphery depict terminal methyl groups of the dodecanethiols. Note the preferentially oriented molecular bundles at the lower temperature. Image Taken from Luedtke, W. D.; Landman, U. *J Phys Chem B* 1998, *102*, 6566-6572.

In a related study using classical molecular and quantum mechanics approximations to calculate the role of thiol molecules on the kinetics of the superlattice formation and in the structure of the nanoparticles, Guttierez-Wing and coworkers found that thiol covered gold particles with a size of ~5 nm present a rounded shape suggesting that thiol molecules might induce an isotropic.[37] The authors examined dodecanethiol coated Au_{147} nanoparticles and calculate the most stable structure of n-alkylthiol molecules on the core surface and particularly the distribution of sulfur pairs.[37] Figure 1.15b shows the distribution of chains around an FCC cluster. As can be seen from the figure, there is some sulfur-sulfur pairing around the cluster indicating that at least partially the molecules formed are in the form of disulfide. This possibility of producing a disulphide array is obtained when the number of thiol molecules around a gold nanoparticle is enough to saturate the flat planes. When the number of sulfur atoms are not enough completely coat the core, thiolate behavior can be observed (Figure 1.15a); the sulfur atoms try to distribute over the flat planes and avoid the edge of the nanocrystal. Similar findings of disulfide formation for alkanethiol monolayers on flat Au(111)on were reported by Fenter and coworkers.[101] Using grazing incidence x-ray, a sulfur-sulfur distance of 2.2 Å was reported, implying the existence of a sulfur-sulfur bond. However, the reader should note that the results by Fenter are highly controversial, with other authors reporting spacings closer to 5 Å using different techniques. It has been suggested that the use of x-rays to measure ligand spacing results in an excited state of the thiol molecules, causing them to move from their Au-S, ground state form to the higher energy disulfide state.

In sum, the ligand model that has been inferred from experiment and theory is as follows: ligands pack tightly on each facet of the core, likely with a sulfur-sulfur spacing smaller than that for comparable 2-D monolayers. The chains tend to be highly crystalline, forming bundles in which all chains assume the same tilt angle over single and/or multiple facets. Additionally the ligands posses a large degree of head group mobility, accompanied by significant numbers of defects, due to the decreasing packing density that occurs radially from the core surface.

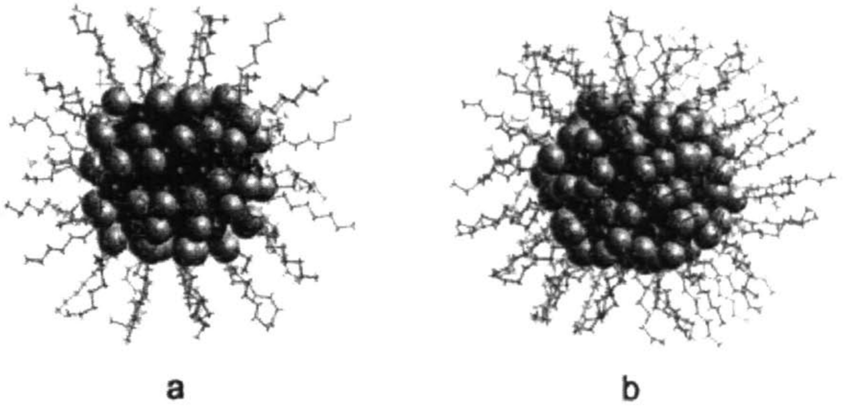

Figure 1.15 Calculation of the stable structure of dodecanthiol ligands on Au_{147} nanoparticles with either (a) 60 molecules (not a full monolayer) in which a Au-S bond is formed for each molecule, or (b) 85 thiols (a complete monolayer, 3:1 gold atoms:sulfur atoms) in which disulfides form between some of the molecules. Taken from: Gutierrez-Wing, C.; Ascencio, J. A.; Perez-Alvarez, M.; Marin-Almazo, M.; Jose-Yacaman, M. *J Clust Sci* 1998, *9*, 529-545.

1.10. References

1. De Wall, S. L.; Painter, C.; Stone, J. D.; Bandaranayake, R.; Wiley, D. C.; Mitchison, T. J.; Stern, L. J.; Dedecker, B. S., Noble metals strip peptides from class II MHC proteins. *Nature Chemical Biology* **2006,** 2, (4), 197-201.
2. Daniel, M. C.; Astruc, D., Gold nanoparticles: Assembly, supramolecular chemistry, quantum-size-related properties, and applications toward biology, catalysis, and nanotechnology. *Chemical Reviews* **2004,** 104, (1), 293-346.
3. Kunckels, J., *Nuetliche Observationes oder Anmerkungen von Auro und Argento Potabile*. Schutzens: Hamburg, 1676.
4. Helcher, H. H., *Aurum Potabile oder Gold Tinstur*. J. Herbord Klossen: Breslau and Leipzig, 1718.
5. Savage, G., *Glass and Glassware*. Octopus Book: London, 1975.
6. Ostwald, W., Zur Geschichte des Colloiden Goldes. *Kolloid Z* **1909,** 4, 5.
7. Graham, T., *Philosophical Transactions of the Royal Society* **1861,** 151, 183-190.
8. Faraday, M., Experimental Relations of Gold (and other Metals) to Light. *Philos. Trans.* **1857,** 147, 145-181.
9. Schmid, G., Developments in Transition-Metal Cluster Chemistry - the Way to Large Clusters. *Structure and Bonding* **1985,** 62, 51-85.
10. Schmid, G.; Pfeil, R.; Boese, R.; Bandermann, F.; Meyer, S.; Calis, G. H. M.; Vandervelden, W. A., Au55[P(C6h5)3]12cl6 - a Gold Cluster of an Exceptional Size. *Chemische Berichte-Recueil* **1981,** 114, (11), 3634-3642.
11. Brust, M.; Walker, M.; Bethell, D.; Schiffrin, D. J.; Whyman, R., Synthesis of Thiol-Derivatized Gold Nanoparticles in a 2-Phase Liquid-Liquid System. *Journal of the Chemical Society-Chemical Communications* **1994**, (7), 801-802.
12. Schmid, G.; Baumle, M.; Geerkens, M.; Helm, I.; Osemann, C.; Sawitowski, T., Current and future applications of nanoclusters. *Chemical Society Reviews* **1999,** 28, (3), 179-185.
13. Love, J. C.; Estroff, L. A.; Kriebel, J. K.; Nuzzo, R. G.; Whitesides, G. M., Self-assembled monolayers of thiolates on metals as a form of nanotechnology. *Chemical Reviews* **2005,** 105, (4), 1103-1169.
14. Efros, A. L.; Efros, A. L., Interband Absorption of Light in a Semiconductor Sphere. *Soviet Physics Semiconductors-Ussr* **1982,** 16, (7), 772-775.
15. Brus, L. E., A Simple-Model for the Ionization-Potential, Electron-Affinity, and Aqueous Redox Potentials of Small Semiconductor Crystallites. *Journal of Chemical Physics* **1983,** 79, (11), 5566-5571.
16. Norris, D. J.; Efros, A. L.; Rosen, M.; Bawendi, M. G., Size dependence of exciton fine structure in CdSe quantum dots. *Physical Review B* **1996,** 53, (24), 16347-16354.
17. Norris, D. J.; Bawendi, M. G., Measurement and assignment of the size-dependent optical spectrum in CdSe quantum dots. *Physical Review B* **1996,** 53, (24), 16338-16346.
18. Zheng, J.; Zhang, C. W.; Dickson, R. M., Highly fluorescent, water-soluble, size-tunable gold quantum dots. *Physical Review Letters* **2004,** 93, (7), -.

19. Belloni, J., Metal nanocolloids. *Current Opinion in Colloid & Interface Science* **1996,** 1, (2), 184-196.
20. Kreibig, U.; Vollmer, M., *Optical Properties of Metal Clusters.* Springer: Berlin, 1995.
21. Link, S.; El-Sayed, M. A., Spectral properties and relaxation dynamics of surface plasmon electronic oscillations in gold and silver nanodots and nanorods. *Journal of Physical Chemistry B* **1999,** 103, (40), 8410-8426.
22. Katz, E.; Willner, I., Integrated nanoparticle-biomolecule hybrid systems: Synthesis, properties, and applications. *Angewandte Chemie-International Edition* **2004,** 43, (45), 6042-6108.
23. Teo, B. K.; Zhang, H., Magic Numbers in Clusters. In *Metal Nanoparticles*, Feldhaim, D. L.; Foss, C. A., Eds. Marcel Dekker, INC.: New Yorl, 2002.
24. Zhang, H.; Wang, X. M.; Zhang, K. C.; Teo, B. K., Functional crystals: Search criteria and design principles. *Journal of Solid State Chemistry* **2000,** 152, (1), 191-198.
25. Teo, B. K.; Strizhev, A.; Elber, R.; Zhang, H., Iconography of icosahedra. Calculations of metallic energies and relative stabilities of stereoisomers of binary icosahedral clusters. *Inorganic Chemistry* **1998,** 37, (10), 2482-2495.
26. Teo, B. K.; Zhang, H., Clusters of Clusters - Self-Organization and Self-Similarity in the Intermediate Stages of Cluster Growth of Au Ag Supraclusters. *Proceedings of the National Academy of Sciences of the United States of America* **1991,** 88, (12), 5067-5071.
27. Zhang, Z.; Hu, W. Y.; Xiao, S. F., Shell and subshell periodic structures of icosahedral nickel nanoclusters. *Journal of Chemical Physics* **2005,** 122, (21), -.
28. Wang, Y. T.; Teitel, S.; Dellago, C., Melting of icosahedral gold nanoclusters from molecular dynamics simulations. *Journal of Chemical Physics* **2005,** 122, (21), -.
29. Wang, Y. T.; Teitel, S.; Dellago, C., Melting and equilibrium shape of icosahedral gold nanoparticles. *Chemical Physics Letters* **2004,** 394, (4-6), 257-261.
30. Mackay, A. L., *Acta Crystallographica* **1962,** 15, 916.
31. Mandich, M. L., *Atomic, Molecular, & Optical Physics Handbook.* AIP Press: New York, 1996.
32. Hakkinen, H.; Moseler, M., 55-atom clusters of silver and gold: Symmetry breaking by relativistic effects. *Computational Materials Science* **2006,** 35, (3), 332-336.
33. Zanchet, D.; Hall, B. D.; Ugarte, D., Structure population in thiol-passivated gold nanoparticles. *Journal of Physical Chemistry B* **2000,** 104, (47), 11013-11018.
34. Hostetler, M. J.; Wingate, J. E.; Zhong, C. J.; Harris, J. E.; Vachet, R. W.; Clark, M. R.; Londono, J. D.; Green, S. J.; Stokes, J. J.; Wignall, G. D.; Glish, G. L.; Porter, M. D.; Evans, N. D.; Murray, R. W., Alkanethiolate gold cluster molecules with core diameters from 1.5 to 5.2 nm: Core and monolayer properties as a function of core size. *Langmuir* **1998,** 14, (1), 17-30.
35. Nuzzo, R. G.; Dubois, L. H.; Allara, D. L., Fundamental-Studies of Microscopic Wetting on Organic-Surfaces .1. Formation and Structural Characterization of a Self-Consistent Series of Polyfunctional Organic Monolayers. *Journal of the American Chemical Society* **1990,** 112, (2), 558-569.
36. Schlenoff, J. B.; Li, M.; Ly, H., Stability and self-exchange in alkanethiol monolayers. *Journal of the American Chemical Society* **1995,** 117, (50), 12528-12536.

37. Gutierrez-Wing, C.; Ascencio, J. A.; Perez-Alvarez, M.; Marin-Almazo, M.; Jose-Yacaman, M., On the structure and formation of self-assembled lattices of gold nanoparticles. *Journal of Cluster Science* **1998,** 9, (4), 529-545.

38. Shaffer, A. W.; Worden, J. G.; Huo, Q., Comparison study of the solution phase versus solid phase place exchange reactions in the controlled functionalization of gold nanoparticles. *Langmuir* **2004,** 20, (19), 8343-8351.

39. Turkevitch, J.; Stevenson, P. C.; Hillier, J., Nucleation and Growth Process in the Synthesis of Colloidal Gold. *Discuss. Faraday Soc.* **1951,** 11, 55-75.

40. Frens, G., Controlled Nucleation for Regulation of Particle-Size in Monodisperse Gold Suspensions. *Nature-Physical Science* **1973,** 241, (105), 20-22.

41. Murray, C. B.; Kagan, C. R.; Bawendi, M. G., Synthesis and characterization of monodisperse nanocrystals and close-packed nanocrystal assemblies. *Annual Review of Materials Science* **2000,** 30, 545-610.

42. Kim, J. U.; Cha, S. H.; Shin, K.; Jho, J. Y.; Lee, J. C., Synthesis of gold nanoparticles from gold(I)-alkanethiolate complexes with supramolecular structures through electron beam irradiation in TEM. *Journal of the American Chemical Society* **2005,** 127, (28), 9962-9963.

43. Dance, I. G.; Fisher, K. J.; Banda, R. M. H.; Scudder, M. L., Layered Structure of Crystalline Compounds Agsr. *Inorganic Chemistry* **1991,** 30, (2), 183-187.

44. Alvarez, M. M.; Khoury, J. T.; Schaaff, T. G.; Shafigullin, M. N.; Vezmar, I.; Whetten, R. L., Optical absorption spectra of nanocrystal gold molecules. *Journal of Physical Chemistry B* **1997,** 101, (19), 3706-3712.

45. Mcneillie, A.; Brown, D. H.; Smith, W. E.; Gibson, M.; Watson, L., X-Ray Photoelectron-Spectra of Some Gold Compounds. *Journal of the Chemical Society-Dalton Transactions* **1980**, (5), 767-770.

46. Brust, M.; Fink, J.; Bethell, D.; Schiffrin, D. J.; Kiely, C., Synthesis and Reactions of Functionalized Gold Nanoparticles. *Journal of the Chemical Society-Chemical Communications* **1995**, (16), 1655-1656.

47. Kang, S. Y.; Kim, K., Comparative study of dodecanethiol-derivatized silver nanoparticles prepared in one-phase and two-phase systems. *Langmuir* **1998,** 14, (1), 226-230.

48. Bigelow, W. C.; Pickett, D. L.; Zisman, D. L., Oleophobic Monolayers. *J. Colloid INterface Sci.* **1946,** 1, 513-538.

49. Ulman, A., Formation and structure of self-assembled monolayers. *Chemical Reviews* **1996,** 96, (4), 1533-1554.

50. Ulman, A.; Eilers, J. E.; Tillman, N., Packing and Molecular-Orientation of Alkanethiol Monolayers on Gold Surfaces. *Langmuir* **1989,** 5, (5), 1147-1152.

51. Thomas, R. C.; Sun, L.; Crooks, R. M.; Ricco, A. J., Real-Time Measurements of the Gas-Phase Adsorption of Normal-Alkylthiol Monolayers and Multilayers on Gold. *Langmuir* **1991,** 7, (4), 620-622.

52. Xu, C. J.; Sun, L.; Kepley, L. J.; Crooks, R. M.; Ricco, A. J., Molecular-Interactions between Organized, Surface-Confined Monolayers and Vapor-Phase Probe Molecules .6. In-Situ Ftir External Reflectance Spectroscopy of Monolayer Adsorption and Reaction Chemistry. *Analytical Chemistry* **1993,** 65, (15), 2102-2107.

53. Zhong, C. J.; Porter, M. D., Designing Interfaces at the Molecular-Level. *Analytical Chemistry* **1995,** 67, (23), A709-A715.

54. *CRC Handbook of Chemistry and Physics.* 71 ed.; CRC Press: Boca Raton, 1990.
55. Stranick, S. J.; Parikh, A. N.; Tao, Y. T.; Allara, D. L.; Weiss, P. S., Phase-Separation of Mixed-Composition Self-Assembled Monolayers into Nanometer-Scale Molecular Domains. *Journal of Physical Chemistry* **1994,** 98, (31), 7636-7646.
56. Hostetler, M. J.; Stokes, J. J.; Murray, R. W., Infrared spectroscopy of three-dimensional self-assembled monolayers: N-alkanethiolate monolayers on gold cluster compounds. *Langmuir* **1996,** 12, (15), 3604-3612.
57. Collard, D. M.; Fox, M. A., Use of Electroactive Thiols to Study the Formation and Exchange of Alkanethiol Monolayers on Gold. *Langmuir* **1991,** 7, (6), 1192-1197.
58. Yang, G. H.; Amro, N. A.; Starkewolfe, Z. B.; Liu, G. Y., Molecular-level approach to inhibit degradations of alkanethiol self-assembled monolayers in aqueous media. *Langmuir* **2004,** 20, (10), 3995-4003.
59. Stranick, S. J.; Atre, S. V.; Parikh, A. N.; Wood, M. C.; Allara, D. L.; Winograd, N.; Weiss, P. S., Nanometer-scale phase separation in mixed composition self-assembled monolayers. *Nanotechnology* **1996,** 7, (4), 438-442.
60. Hickman, J. J.; Ofer, D.; Zou, C. F.; Wrighton, M. S.; Laibinis, P. E.; Whitesides, G. M., Selective Functionalization of Gold Microstructures with Ferrocenyl Derivatives Via Reaction with Thiols or Disulfides - Characterization by Electrochemistry and Auger-Electron Spectroscopy. *Journal of the American Chemical Society* **1991,** 113, (4), 1128-1132.
61. Folkers, J. P.; Laibinis, P. E.; Whitesides, G. M.; Deutch, J., Phase-Behavior of 2-Component Self-Assembled Monolayers of Alkanethiolates on Gold. *Journal of Physical Chemistry* **1994,** 98, (2), 563-571.
62. Schessler, H. M.; Karpovich, D. S.; Blanchard, G. J., Quantitating the balance between enthalpic and entropic forces in alkanethiol/gold monolayer self assembly. *Journal of the American Chemical Society* **1996,** 118, (40), 9645-9651.
63. Trevor, J. L.; Lykke, K. R.; Pellin, M. J.; Hanley, L., Two-laser mass spectrometry of thiolate, disulfide, and sulfide self-assembled monolayers. *Langmuir* **1998,** 14, (7), 1664-1673.
64. Bumm, L. A.; Arnold, J. J.; Charles, L. F.; Dunbar, T. D.; Allara, D. L.; Weiss, P. S., Directed self-assembly to create molecular terraces with molecularly sharp boundaries in organic monolayers. *Journal of the American Chemical Society* **1999,** 121, (35), 8017-8021.
65. Bain, C. D.; Biebuyck, H. A.; Whitesides, G. M., Comparison of Self-Assembled Monolayers on Gold - Coadsorption of Thiols and Disulfides. *Langmuir* **1989,** 5, (3), 723-727.
66. Bain, C. D.; Troughton, E. B.; Tao, Y. T.; Evall, J.; Whitesides, G. M.; Nuzzo, R. G., Formation of Monolayer Films by the Spontaneous Assembly of Organic Thiols from Solution onto Gold. *Journal of the American Chemical Society* **1989,** 111, (1), 321-335.
67. Kang, J. F.; Liao, S.; Jordan, R.; Ulman, A., Mixed self-assembled monolayers of rigid biphenyl thiols: Impact of solvent and dipole moment. *Journal of the American Chemical Society* **1998,** 120, (37), 9662-9667.
68. Whitesides, G. M.; Laibinis, P.; Folkers, J.; Prime, K.; Seto, C.; Zerkowski, J., Self-Assembly - Alkanethiolates on Gold and Hydrogen-Bonded Networks. *Abstracts of Papers of the American Chemical Society* **1991,** 201, 103-Inor.

69. Tamada, K.; Hara, M.; Sasabe, H.; Knoll, W., Surface phase behavior of n-alkanethiol self-assembled monolayers adsorbed on Au(111): An atomic force microscope study. *Langmuir* **1997,** 13, (6), 1558-1566.
70. Lee, L. Y. S.; Sutherland, T. C.; Rucareanu, S.; Lennox, R. B., Ferrocenylalkylthiolates as a probe of heterogeneity in binary self-assembled monolayers on gold. *Langmuir* **2006,** 22, (9), 4438-4444.
71. Phong, P. H.; Ooi, Y.; Hobara, D.; Nishi, N.; Yamamoto, M.; Kakiuchi, T., Phase separation of ternary self-assembled monolayers into hydrophobic 1-dodecanethiol domains and electrostatically stabilized hydrophilic domains composed of 2-aminoethanethiol and 2-mercaptoethanesulfonic acid on Au(111). *Langmuir* **2005,** 21, (23), 10581-10586.
72. Smith, R. K.; Reed, S. M.; Lewis, P. A.; Monnell, J. D.; Clegg, R. S.; Kelly, K. F.; Bumm, L. A.; Hutchison, J. E.; Weiss, P. S., Phase separation within a binary self-assembled monolayer on Au{111} driven by an amide-containing alkanethiol. *Journal of Physical Chemistry B* **2001,** 105, (6), 1119-1122.
73. Marks, L. D., Experimental Studies of Small-Particle Structures. *Reports on Progress in Physics* **1994,** 57, (6), 603-649.
74. Iijima, S.; Ichihashi, T., Structural Instability of Ultrafine Particles of Metals. *Physical Review Letters* **1986,** 56, (6), 616-619.
75. Barnard, A. S.; Lin, X. M.; Curtiss, L. A., Equilibrium morphology of face-centered cubic gold nanoparticles > 3 nm and the shape changes induced by temperature. *Journal of Physical Chemistry B* **2005,** 109, (51), 24465-24472.
76. Cleveland, C. L.; Landman, U.; Shafigullin, M. N.; Stephens, P. W.; Whetten, R. L., Structural evolution of larger gold clusters. *Zeitschrift Fur Physik D-Atoms Molecules and Clusters* **1997,** 40, (1-4), 503-508.
77. Cervellino, A.; Giannini, C.; Guagliardi, A.; Zanchet, D., Quantitative analysis of gold nanoparticles from synchrotron data by means of least-squares techniques - Least-squares analysis of gold nanoparticles. *European Physical Journal B* **2004,** 41, (4), 485-493.
78. Zhang, P.; Sham, T. K., X-ray studies of the structure and electronic behavior of alkanethiolate-capped gold nanoparticles: The interplay of size and surface effects. *Physical Review Letters* **2003,** 90, (24), -.
79. Ascencio, J. A.; Perez, M.; Jose-Yacaman, M., A truncated icosahedral structure observed in gold nanoparticles. *Surface Science* **2000,** 447, (1-3), 73-80.
80. Badia, A.; Cuccia, L.; Demers, L.; Morin, F.; Lennox, R. B., Structure and dynamics in alkanethiolate monolayers self-assembled on gold nanoparticles: A DSC, FT-IR, and deuterium NMR study. *Journal of the American Chemical Society* **1997,** 119, (11), 2682-2692.
81. Badia, A.; Singh, S.; Demers, L.; Cuccia, L.; Brown, G. R.; Lennox, R. B., Self-assembled monolayers on gold nanoparticles. *Chemistry-a European Journal* **1996,** 2, (3), 359-363.
82. Terrill, R. H.; Postlethwaite, T. A.; Chen, C. H.; Poon, C. D.; Terzis, A.; Chen, A. D.; Hutchison, J. E.; Clark, M. R.; Wignall, G.; Londono, J. D.; Superfine, R.; Falvo, M.; Johnson, C. S.; Samulski, E. T.; Murray, R. W., Monolayers in three dimensions: NMR, SAXS, thermal, and electron hopping studies of alkanethiol stabilized gold clusters. *Journal of the American Chemical Society* **1995,** 117, (50), 12537-12548.

83. Templeton, A. C.; Hostetler, M. J.; Kraft, C. T.; Murray, R. W., Reactivity of monolayer-protected gold cluster molecules: Steric effects. *Journal of the American Chemical Society* **1998,** 120, (8), 1906-1911.
84. Badia, A.; Demers, L.; Dickinson, L.; Morin, F. G.; Lennox, R. B.; Reven, L., Gold-sulfur interactions in alkylthiol self-assembled monolayers formed on gold nanoparticles studied by solid-state NMR. *Journal of the American Chemical Society* **1997,** 119, (45), 11104-11105.
85. Hong, R.; Fernandez, J. M.; Nakade, H.; Arvizo, R.; Emrick, T.; Rotello, V. M., In situ observation of place exchange reactions of gold nanoparticles. Correlation of monolayer structure and stability. *Chemical Communications* **2006,** (22), 2347-2349.
86. Paulini, R.; Frankamp, B. L.; Rotello, V. M., Effects of branched ligands on the structure and stability of monolayers on gold nanoparticles. *Langmuir* **2002,** 18, (6), 2368-2373.
87. Wuelfing, W. P.; Templeton, A. C.; Hicks, J. F.; Murray, R. W., Taylor dispersion measurements of monolayer protected clusters: A physicochemical determination of nanoparticle size. *Analytical Chemistry* **1999,** 71, (18), 4069-4074.
88. Hostetler, M. J.; Templeton, A. C.; Murray, R. W., Dynamics of place-exchange reactions on monolayer-protected gold cluster molecules. *Langmuir* **1999,** 15, (11), 3782-3789.
89. Hasan, M.; Bethell, D.; Brust, M., The fate of sulfur-bound hydrogen on formation of self-assembled thiol monolayers on gold: H-1 NMR spectroscopic evidence from solutions of gold clusters. *Journal of the American Chemical Society* **2002,** 124, (7), 1132-1133.
90. Chechik, V., Reduced reactivity of aged Au nanoparticles in ligand exchange reactions. *Journal of the American Chemical Society* **2004,** 126, (25), 7780-7781.
91. Wellsted, H.; Sitsen, E.; Caragheorgheopol, A.; Chechik, V., Polydisperse composition of mixed mono layer-protected, spin-labeled Au nanoparticles. *Analytical Chemistry* **2004,** 76, (7), 2010-2016.
92. Song, Y.; Heien, M. L. A. V.; Jimenez, V.; Wightman, R. M.; Murray, R. W., Voltammetric detection of metal nanoparticles separated by liquid chromatography. *Analytical Chemistry* **2004,** 76, (17), 4911-4919.
93. Nuzzo, R. G.; Zegarski, B. R.; Dubois, L. H., Fundamental-Studies of the Chemisorption of Organosulfur Compounds on Au(111) - Implications for Molecular Self-Assembly on Gold Surfaces. *Journal of the American Chemical Society* **1987,** 109, (3), 733-740.
94. Boal, A. K.; Rotello, V. M., Intra- and intermonolayer hydrogen bonding in amide-functionalized alkanethiol self-assembled monolayers on gold nanoparticles. *Langmuir* **2000,** 16, (24), 9527-9532.
95. Ulman, A., Thermal-Stability of Langmuir-Blodgett and Self-Assembled Films - a Possible Scenario for Order-Disorder Transitions. *Advanced Materials* **1991,** 3, (6), 298-303.
96. Mitra, S.; Nair, B.; Pradeep, T.; Goyal, P. S.; Mukhopadhyay, R., Alkyl chain dynamics in monolayer-protected clusters (MPCs): A quasielastic neutron-scattering investigation. *Journal of Physical Chemistry B* **2002,** 106, (15), 3960-3967.

97. Luedtke, W. D.; Landman, U., Structure and thermodynamics of self-assembled monolayers on gold nanocrystallites. *Journal of Physical Chemistry B* **1998,** 102, (34), 6566-6572.

98. Pradeep, T.; Mitra, S.; Nair, A. S.; Mukhopadhyay, R., Dynamics of alkyl chains in monolayer-protected Au and Ag clusters and silver thiolates: A comprehensive quasielastic neutron scattering investigation. *Journal of Physical Chemistry B* **2004,** 108, (22), 7012-7020.

99. Bigioni, T. P.; Harrell, L. E.; Cullen, W. G.; Guthrie, D. E.; Whetten, R. L.; First, P. N., Imaging and tunneling spectroscopy of gold nanocrystals and nanocrystal arrays. *European Physical Journal D* **1999,** 6, (3), 355-364.

100. Taleb, A.; Silly, F.; Gusev, A. O.; Charra, F.; Pileni, M. P., Electron transport properties of nanocrystals: Isolated, and "supra"-crystalline phases. *Advanced Materials* **2000,** 12, (9), 633-+.

101. Fenter, P.; Eberhardt, A.; Eisenberger, P., Self-Assembly of N-Alkyl Thiols as Disulfides on Au(111). *Science* **1994,** 266, (5188), 1216-1218.

2. STM imaging of nanoparticles

2.1. Introduction to STM

Scanning Tunneling Microscopy (STM) relies on detecting variations in tunneling current between a metallic tip and conductive sample to map a sample surface. As the tip scans across a surface, it measures changes in tunneling current that result either from changes in sample height or chemical functionality, and maps these changes, creating either a topographic height or current map of the substrate. In the case of monolayer protected nanoparticles, typically the mixtures of ligands differ in height and chemical functionality (so chosen to drive phase separation); thus, the resulting height image of such phase separated domains is due to both a chemical and length difference.

However, in order to accurately derive the 'true' molecular configuration of the ligands surrounding the core from the resulting STM image (height or current), one must also understand how such an image is generated (that is, how the variations in the current that the tip detects are translated to an image). In simple terms, a voltage is applied between tip and sample, a resulting tunneling current flows, and changes in this current are detected (Figure 2.1). The tip then adjusts its height according to the values of the feedback gains, in response to both the rate of change of tunneling current and the magnitude of the change in order to maintain the current at its preset value. Both the current and height changes can be mapped allowing for us, the user, to determine where variations in topography and/or chemical functionality occur on the substrate. It is important to emphasize that the resulting images that one views are 'maps' (or, as an analogy, 'shadows'), not exact replicas, of the substrate—the final image is dependent on both how the map (or shadow) is formed (there can be different maps drawn for the same substrate), as well as the convolution of height and chemical differences. While one may speak of 'visualization' of a substrate, he is seeing only what the mapping function, (which includes the user determined feedback gains) within the STM, has produced. From these images, knowledge of the substrate, and knowledge from other characterization techniques, we must then reconstruct the true nature of the substrate. This is the challenge of STM. In the following sections I will detail how one can extract the molecular configurations of ligands around the nanoparticle core using STM, starting from sample preparation to imaging controls to image interpretation.

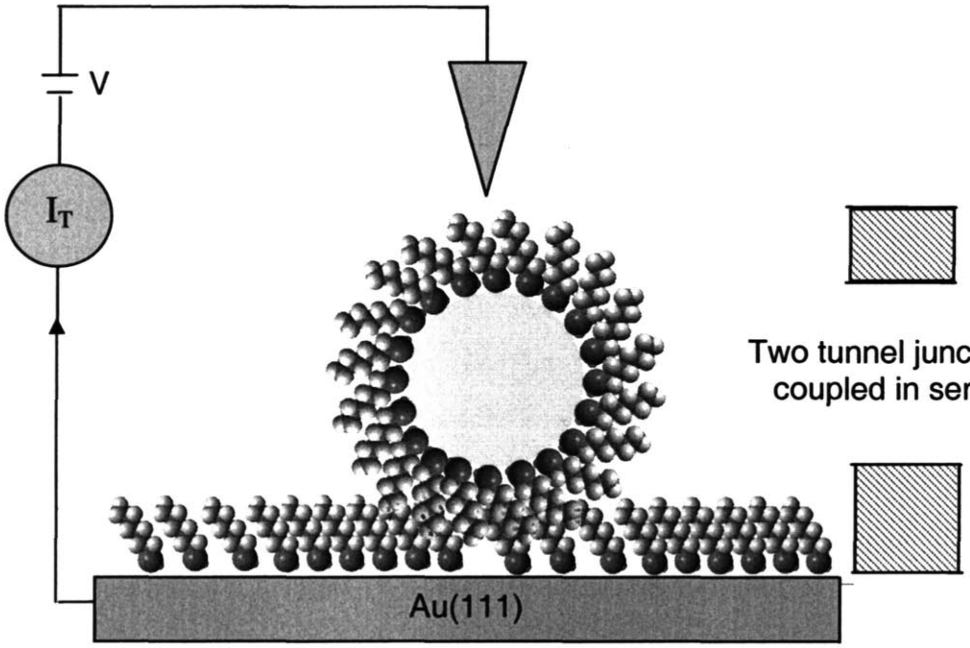

Figure 2.1 Schematic of STM configuration for imaging of a monolayer protected metal nanoparticle. Note that the SAM on the substrate serves to stabilize the nanoparticle through van der Waals interactions, but also increases the tunneling distance between the nanoparticle core and Au substrate.

2.2. Sample preparation

2.2.1. Nanoparticles

Because STM imaging relies only on differences in tunneling current, any contamination of the tip or nanoparticle will complicate and/or obstruct visualization of the molecular packing and domains. The contamination can range from an impurity introduced into the ligand shell during synthesis (e.g. tetraoctylammonium bromide (TOABr)) (Figure 2.2),[1] during sample preparation (e.g. dust or dirt), or from a contaminated or poorly shaped tip. Thus, nanoparticles must be clean from their synthesis onwards. This may mean the use of Soxhlet extraction to remove any remaining TOABr in the case of 2-phase synthesized particles,[1] as well as significant washing in the case of all syntheses to remove unreacted thiols and any other contaminants remaining in the product solution.

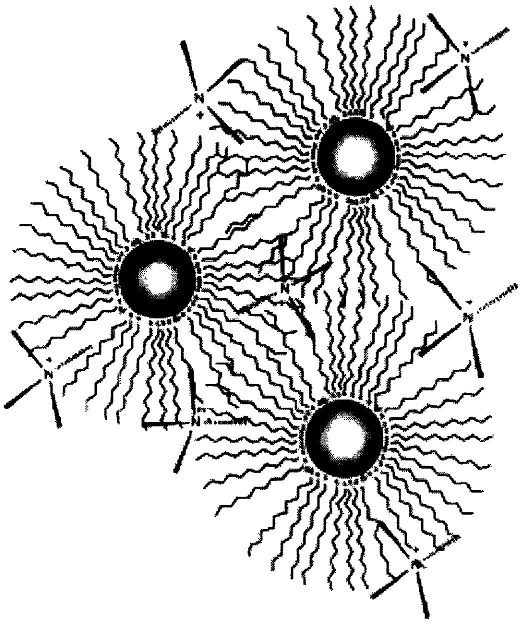

Figure 2.2 Schematic of dodecanethiol gold nanoparticles synthesised by a two-phase method showing a significant amount of tetraoctylammonium bromide (TOABr), the quaternary ammonium salt used as the phase transfer reagent, as a persistently retained impurity. Note that the long chains of the last obscure the headgroups of the ligand shell. Image taken from Waters, C. A.; Mills, A. J.; Johnson, K. A.; Schiffrin, D. J. *Chem Commun* 2003, 540-541.

2.3. Nanoparticle film formation

Substrates should be prepared so that they fulfill two conditions: 1) The particles form a nearly flat layer—allowing the tip to effectively track the surface (discussed further in section 3.4.1), and 2) They are closely packed—resulting in immobilization of the particles by physically constraining them to a small area as well as through the possible interdigitation of ligands between ligand shells, further serving to stabilize and lock the particles into place. We focus here on the two forms of particle immobilization—surface immobilization and interparticle immobilization. In regards to surface immobilization of particles, the typical method is to use dithiol chemistry to bind gold nanoparticles to a gold substrate and sometimes to one another (referred to as **Method 1**) or, more simply, to form an alkanethiolate monolayer on the gold substrate first and rely upon van der Waals interactions between the surface SAM and the ligand shell, as well as between particles, to help hold the particles in place (**Method 2**). One consideration to keep in mind is that the detected STM tunneling current is exponentially dependent on the distance that the electrons must flow; thus, using a long moleculecular linker between the nanoparticle and substrate can significantly decrease the tunneling current, making imaging difficult.

There are 3 basic methods that are used to immobilize particles: **Method 1**—use dithiols to link nanoparticles to the surface and/or each other; **Method 2**—use VDW interactions between nanoparticles and an alkanethiolate SAM on the surface; and **Method 3**—use a bare gold substrate and rely only on interparticle interactions to anchor particles. Note that due to differences in the ligand shell composition of the particles, one method may work better than another in immobilizing the particles. Additionally variations of all of these methods are also employed. In the case of **Method 1**, alkanedithiol molecules are used to act as linkers, binding the nanoparticles to the underlying substrate, and sometimes to one another, creating a dense network of nanoparticles. However, care should be taken not to introduce dithiol indiscriminately into the ligand shell in order to ensure preservation of the ligand shell composition. This is especially important in the case of very small nanoparticles (<2 nm core diameter) which have been shown to be highly reactive in regards to place exchange.[2] The method is as follows: a SAM of 1,8 octanedithiol (ODiT) or 1,10 Decanedithiol (Ddit) (the length of linker used is based upon the length of the molecular chains within the nanoparticle ligand shell) is first formed by immersing the gold substrate in a 100-200 μM ethanolic solution overnight, ~24 h prior to nanoparticle layer formation, after which it is immediately rinsed and stored in ethanol. In the case of **Method 2**, an alkanethiolate SAM is formed on the substrate in place of a dithiol monolayer. In **Method 3**, no monolayer is formed.

Next, ~2-10 mg nanoparticles (determined based upon the particles affinity towards the substrate, packing behavior, solubility in solvent, desired surface coverage, and method of attachment to substrate) are dissolved in 10 ml of the appropriate solvent (e.g. typically toluene or ethanol depending on the nanoparticle solubility), and then filtered through a 0.2 μm PTFE filter to remove any large aggregates. The particles can then be exposed and attached to the substrate using one of three methods, denoted as **attach1**, **attach2**, and **attach3**. For **attach1,** the substrate is immersed in the nanoparticle solution allowing for particles to self-assemble on the surface; this is typically driven by favorable enthalpic interactions between the SAM on the substrate and the 3-D SAM on the nanoparticle. In the case of a dithiol SAM, the nanoparticle may actually form a Au-S bond with the substrate monolayer. This method works very well for particles which have a high affinity for the substrate.[a] In **attach2** the particles are cast onto the substrate and the solvent allowed to slowly evaporate in the presence of a saturated solvent atmosphere (note that the substrate must be level to allow for even evaporation). This method allows for the creation of an ordered film of particles through self-assembly; however, unless the evaporation conditions are highly controlled and known, large aggregates of particles may form on the substrate and/or some regions are completely devoid of particles. The last technique is **attach3**—the particles are cast onto a substrate and the solvent allowed to quickly evaporate (the substrate may be heated to encourage solvent evaporation). This method aids in circumventing the formation of large aggregates on the substrate as well as instances where, due to nanoparticle functionality, the particles are not attracted to the sample surface (e.g. in the case of extensive amounts of ligand charge) and essentially

---

[a] Alternatively, equivalent samples could also be prepared by simply immersing the substrate in 20 mL of a 5.6 10^{-2} mM toluene solution of ODiT or DdiT containing 2 mg nanoparticles for 24 h. However, immersion of the nanoparticles in the dithiol solution carries the risk of an unknown amount of place exchange of dithiols into the ligand shell possibly affecting the ligand shell composition.

‘freezes’ the particles in place on the substrate. Exposure methods **attach2** and **attach3** can be used with all prior substrate preparation methods. However, note that in the case of substrate preparation **Method 3**, where a bare Au substrate is used, casting (**attach2** and **attach3**) is the only method used to form a nanoparticle film. After particle deposition, samples are cleaned to remove loosely bound particles and ligands. Often this involves rinsing with a poor solvent (i.e. one that the particles are soluble in—typically acetone) and then drying under a stream of nitrogen or air.

2.3.1. Substrate types: Au foil, Au on mica, Au on glass

The nature of the underlying gold substrate can have a large impact on the resulting morphological features of the resulting nanoparticle film. Three types of substrates were used over the course of the study: Au foil, Au(111) on Mica, and Au on glass (formed from Au(111) on mica). Each of these substrates has its benefits and disadvantages in regards to flatness, as received surface purity, ease of sample preparation, post cleaning and cost. Au foil is an inexpensive, easy to clean substrate (e.g. it can be sonicated and immersed in a variety of solvents) suitable for rough characterizations of nanoparticles (e.g. to determine if the particles are clean, pack well and are easily imageable). Its main drawback is lack of flatness; often the foil surface contains regions composed of hemispherical undulations ranging from ~7-20 nm in diameter (Figure 2.3 (d)). These variations in topology can lead to large variations in height of the resulting nanoparticle monolayer, complicating imaging (Figure 2.3). Additionally, if one does not know the nanoparticle diameter and has not formed a confluent multilayer over the substrate, it can sometimes be difficult for a novice to distinguish nanoparticles on the Au foil surface from natural hemispherical bumps on the substrate (although these tend to be much larger than nanoparticles). However, it is these same micro/nanoscopic variations in surface topography which can serve to 'trap' nanoparticles—making this substrate a last resort if, for some reason, particles cannot be deposited onto other substrates. Additionally, because the gold foil can be brought into direct contact with a conducting surface, the electrical transport properties of the sample tend to be high, allowing for easier imaging.

Au(111) on mica consists of atomically flat terraces of gold ~50-200 nm in size—the large degree of flatness being its main advantage. However, as received, it is prone to contamination from the deposition process and often needs to be flame annealed (a difficult process) if one wants to ensure consistent surface cleanliness. For our purposes, and assuming that the gold has not been significantly contaminated, briefly rinsing the gold in boiling acetone is generally sufficient for later creation of nanoparticle monolayers. The observed nanoparticle film morphologies on Au on mica range from the absence of particles (due either to contamination or insufficient particle stabilization), isolated nanoparticles, sparse islands of nanoparticle aggregates and large closely packed layers of particles (Figure 2.4). Whether these variations in nanoparticle film morphology are due to the gold substrate (through contamination) or due to the dispersity, cleanliness, and chemical functionality of the nanoparticles is difficult to understand. For example, Dr. Ying Hu has demonstrated that while nonanethiol/methyl-benzenethiol (NT/MBT) 2:1 nanoparticles synthesized using the Stucky method[3] will form ordered arrays when cast from solvent onto bare Au(111) on mica, 1-phase synthesized particles of the same composition do not consistently form well packed arrays, and sometimes cannot be detected on the gold surface. Additionally, it has also been observed that resulting nanoparticle monolayer morphologies are often not consistent over different Au on mica sample batches despite efforts to keep the sample preparation procedures identical. Thus it is likely, in the case of Au(111) on mica, that the strongest effect on nanoparticle packing is due to the nanoparticles themselves and then, to second order, the nature of the substrate. Furthermore, in the case of isolated particles on the gold surface, the abrupt height changes from flat gold terraces to the curved nanoparticles often results in noisy regions surrounding the nanoparticles, making precise imaging of the ligand shell difficult (Figure 2.4 a and c).

Au on glass formed from Au(111) on mica results in a nearly impurity free and flat surface that is created, as described by Ulman and coworkers [4] through the formation of a SAM at the mica/Au interface on a Au on mica substrate. Briefly, a Au(111) on mica substrate is placed facedown onto a glass slide coated with an epoxy resin, sandwiching the Au film between the glass and the mica. The mica is then removed by placing the sample in an organothiol ethanol solution, so that the molecules intercalcate between the gold and the mica, separating the two surfaces and forming a SAM. While the creation an ultraflat and ultraclean surface is possible and desirable, often the procedure results in a rough surface due to imperfect separation of the Au and mica. Additionally, the presence of an epoxy layer limits the solvents to which the substrate can be exposed, and the epoxy could possibly swell and/or contaminate the nanoparticles. Thus, the use of Au on glass in these studies been limited, but may be a viable substrate for future studies where drop casting of, and not immersion into, nanoparticle solutions to form monolayers is used. Nanoparticle monolayers formed on gold on glass tend to form well ordered, typically hexagonally packed, long range arrays (>500 nm) (Figure 2.5). Typically the films were 1-2 layers thick and, for the compositions examined, no large mountains were observed—although it should be noted that some nanoparticle compositions are more prone to forming clusters regardless of substrate type.

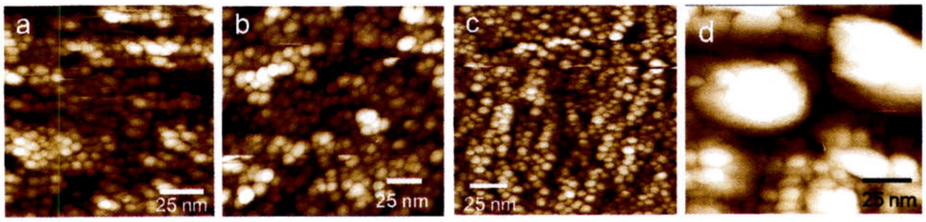

Figure 2.3 (a)-(c) STM images illustrating nanoparticle film morphologies seen on Au foil. Large height variations due to the inherent roughness of the Au foil are evident; (a) OT 1-phase synthesized nanoparticles. (b) Nonanethiol/Mercaptohexanol 2:1, 1-phase synthesized nanoparticles, (c) Nonanethiol/Methylbenzenthiol 2:1, 1-phase synthesized nanoparticles. (d) bare Au foil showing undulations and hemispheres across its surface. Note that the morphology, size, and size distribution of nanoparticles vs. inherent hemispheres on Au foil differ significantly allowing for differentiation between substrate and nanoparticles. Also note that multilayers of nanoparticles on the gold foil serve to 'smooth out' the inherent surface roughness.

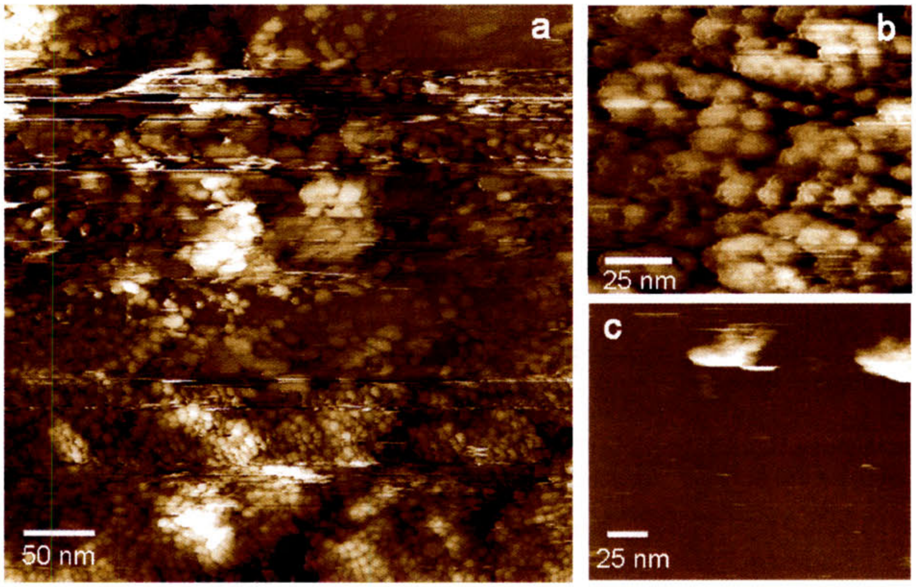

Figure 2.4 STM images of nanoparticle films on Au(111) on mica illustrating the wide range of film morphologies that are observed. (a) OT/MPA 2:1 2-phase synthesized particles showing a wide range of np film morphologies ranging from close packed, uniformly sized particles in the lower third of the scan image to isolated particles and islands towards the top of the image. Streakiness in top of (a) is attributed the loosely packed particles. (b) OT/MPA 2:1 1-phase synthesized nanoparticles showing loosely packed particles. (c) Nonanethiol/Mercaptohexanol 2:1, 1-phase synthesized nanoparticles showing only large islands of aggregates. Streakiness is likely due to the large height difference between the clusters of particles and the substrate.

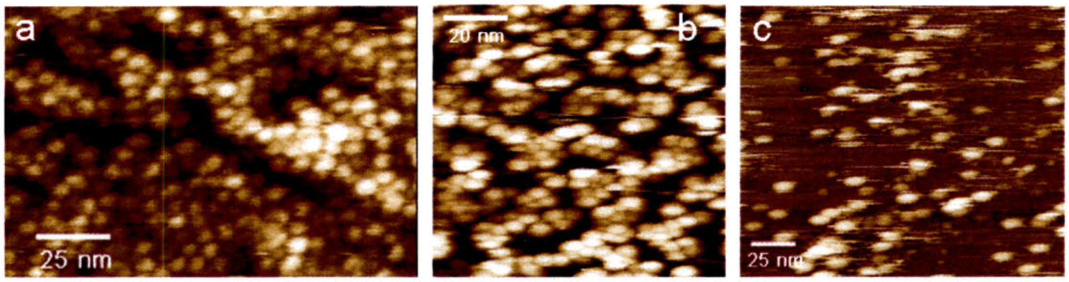

Figure 2.5 STM height images of Au on glass substrates showing: (a) Nonanethiol/mercaptohexanol 2:1, 1-phase synthesized particles forming nearly uniform film of hexagonally packed nanoparticles; (b) OT/MPA 2:1 1-phase synthesized nanoparticles; and (c) same particles as (a) in which only a sub-monolayer was formed resulting in streakiness which is attributed the loosely packed particles.

2.4. Methodology for obtaining an image

In the following sections, I provide a guide to obtaining STM images of nanoparticles. Imaging of nanoparticles, and imaging in general, is as much as an art as it is a science. The most important factors are patience, persistence, and creativity (e.g. trying new parameters and new sample preparation methods). Often if one fails to obtain an image, it is challenging to determine the cause as well as how to amend the problem. The possibilities include contaminated particles, tip or substrate, as well as ligands that are not amenable to imaging due to substantial conformational freedom (obscuring the surrounding ligands), chemical functionality, or length (creating too large of a tunneling barrier). Thus, the basic procedure outlined is not guaranteed to produce results, but will aid immensely in at least visualizing the particles and determining if it is possible to see the ligand shell configuration in that sample. Lastly none of the parameters or following imaging guidelines are hard and set rules—each user will determine his own unique style of imaging, and different parameters can yield the same results.

2.4.1. Effect of feedback gains

As was mentioned previously, when the STM senses a change in tunneling current, it adjusts the tip height according to the user defined feedback parameters. Essentially, the Integral gain and Proportional gain control the response time of the feedback loop by magnifying the difference between the setpoint current and actual current read at the A/D convertor—note that this implies that as tip speed varies, the gains must be adjusted to compensate for the increased/decreased reaction time towards the substrate. Greater gains cause a larger voltage to be sent to the Z piezo than is truly needed. High gains allow for the tip to change its distance from the substrate radically when it encounters a change in height (as one would want for encountering a large step in the substrate). When feedback gains are set low, close to the 'constant current regime', the tip's height is adjusted only slightly in response to variations in current, with most of the changes in sample height registered in the current signal—this is the optimal setting for a flat substrate with small, closely spaced variations in height to be detected, where the tip just skims the surface. This results in a conflict for the optimal feedback parameters for imaging domains on mixed-ligand nanoparticles, or even more challenging—molecular headgroups on homoligand nanoparticles. If the feedback gains are set too high for small, closely spaced variations in height, the tip will not be able to track the surface due to 'over-reacting' and poorly tracking the fine variations in the surface. Each nanoparticle represents a large step from substrate to particle, but the ripples are essentially very fine, closely spaced steps. The desired feedback parameters for imaging each of these (particle vs. ripples) are in conflict—one situation requires high gain feedback, the other, low. As discussed briefly above, forming a nearly flat film of closely packed particles serves to 'smooth out' the substrate. Instead of the tip having to move from the substrate to the nanoparticle, the tip can now scan along the tops of the particles significantly reducing large changes in tip height. Thus the gains can be set so that they are closer to the optimal ones needed for imaging molecular conformations.

2.4.2. DI ambient conditions imaging parameters

For imaging gold nanoparticles (typically 2-8 nm in core diameter) the imaging parameters are crucial to obtaining molecular resolution. Factors such as tip speed and gains, as discussed previously, play a large role in tracking the surface. For example, as tip speed increases, there is essentially 'less time' for the tip to respond to the surface topography accurately, and, often, above 1.2 μm/s a strong noise signal will appear in the image. Additionally, the current setpoint should be set low enough that the tip does not become buried within the monolayer, but large enough (>300 pA) that it can track the surface. The bias voltage must be set so that it is above the coulomb blockade of the particles (typically ~1 V). Typical values for these parameters in normal current mode are: tip speed: 0.4-1.2 μm/s, setpoint current: ~400 pA, integral gain: 0.4-0.8 (initial), proportional gain: 0.5-0.8 (initial), and bias voltage: 1200 mV.

When initially imaging a substrate, one should begin with a large scan size, 200-400 nm, in order to locate areas on the substrate where the nanoparticles are most evenly dispersed (no large mountains or deep valleys), appear the cleanest, and are best packed. The next step is to focus in on one of these areas, reducing the scan size to ~100-150 nm. If the area still appears to be easy to image and the nanoparticles appear clean, proceed to optimize the scan parameters.

In order to increase the resolution of the scanner there are two important parameters to consider: Z-limit and scan size. The Z-limit sets the vertical range sampling intervals, and hence the Z-resolution, by limiting the amount of drive voltage available to the Z piezo circuit (typically 440 V). The Z control system uses a 16-bit D/A converter which drives an amplifier that is capable of outputting voltages from +220 V to -220 V. This means that the resolution of the control over the Z direction is approximately 6.7 mV per bit (440 V divided by 2^{16} (=65536)). Typically the Z-limit can be reduced to 120-80 V if the sample has a very low roughness (no peaks greater than 10 nm). By reducing the Z-limit from its initial value of 440 V, the 16 bits are converted over a smaller range of available voltage to the piezo, resulting in a smaller Z-scan range, but greater Z resolution. For example, reducing the Z limit to 55 V results in eight times finer control over the Z direction of the scanner.

Horizontal pixelation can also affect resolution at large scan sizes, as features smaller than the pixel size of the image cannot be resolved. This can be overcome by reducing the scan size and ensuring that the Samples/line is set at 512. Thus, at a 100 nm scan size, with 512 samples/line, the fast scan resolution of the STM is ~2 Å. Furthermore, to allow for better tip tracking of the surface, as well as to reduce noise and increase the signal from the ligands, the gains can be adjusted incrementally—decreasing the integral down to ~0.5-0.4 and setting the proportional anywhere between 0.7-0.3, depending on the sample. During all of these adjustments, it is helpful to switch back and forth between the height images to the line scans to see how one is affecting the scans and if there is any noise.

Once a low noise and high resolution image is obtained, further reduction of the Z-limit to 80-50 V will increase resolution, and the gains should be further adjusted to decrease any noise and improve the signal—this may mean reducing the integral gain to a value of 0.3. However, every sample is different and so requires different parameters. Sometimes it is necessary to use higher gains or slower scan speeds.

If during imaging the image quality deteriorates, it is possible that the tip has become contaminated either with dust, free ligands or contaminants within the ligand shell, or a nanoparticle itself. It is possible to try and clean the tip, by moving the tip to another area of the sample and applying a voltage pulse to the tip by increasing the bias to ~3-6 V for a second (along with possibly increasing the current to ~2 nA as well). This can help to eject matter from the tip, and sometimes part of the tip itself. However, it should be noted that this procedure often contaminates or ruins the current scan area of the sample. This does not always work, and may take a few tries. Alternatively, the procedure can be done over clean gold or graphite (this can be done as well as before imaging to check the tip quality).

2.5. Ultra high vacuum, variable temperature STM imaging

For certain samples, it may be optimal to obtain images at UHV and low/high temperature. In these cases Ultra High Vacuum (UHV), Variable Temperature (VT) Omicron STM can be used. Obtaining an image using an UHV/VT STM can be considerably more challenging due to the inability to change tips/samples easily due to the UHV environment, as well as the inherent control differences between the DI STM and Omicron systems.

For low temperature imaging of nanoparticles, typically a bias voltage of 1.4 to 2.4 V, a tunneling current value of ~0.58 nA, and a tip speed of 185 to 290 nm/s are used. Additionally, the single gain parameter should be unlocked so as to have control over both the integral and proportional gains with typical values of 3.7% and 3.28%, respectively. Unlocking the gains results in the ability to produce more stable imaging and higher resolution images. The STM is cooled using liquid nitrogen and images can be acquired at a substrate temperature of ~96 K. Note that it is imperative that the samples be checked prior to VT/UHV imaging using the DI STM to ensure sample cleanliness and presence of well packed particles.

2.6. STM imaging of ligand shell: critical analyses during imaging

2.6.1. Overview

The critical challenge and key in STM imaging of ligand coated nanoparticles is the ever elusive, showing clear headgroups, 'nail in the coffin' image, with subsequent images at various tip speeds. Once these images are obtained the molecular structure and arrangements become clear. However, it is more often the case that the images obtained seem to be covered by a 'fog'—the basic structure and hint of ripple may be seen, but that is all, and we are left wondering if what we are seeing is the true structure. By varying the scan speed, angle, and size, we can begin understand if what we are observing is the true structure, but often effects of noise can make this distinction difficult.

STM, as with any scanning probe technique, is subject to noise—acoustic, electrical, or internal—and attempts must be made to recognize and mitigate such noise. For example, acoustic noise can be mitigated through proper environmental isolation and electrical noise, through grounding, dedicated low noise power outlets, and isolation of cables. In order to recognize noise that may manifest itself in STM images, and thereby complicate and dominate the true signal, it is necessary to vary the scan parameters such as scan angle (where the noise direction will not be affected) and tip velocity (where its spacing will vary linearly and extrapolate to zero at zero scan speed). These parameters are discussed in more detail below.

2.6.2. Variation of tip speed

As was mentioned above, often there is a 'sweet-spot' in the imaging parameters (e.g. tip speed, current, gains) for each sample that allows for the best resolution—outside of this range, images may become blurry and molecular resolution lost. However, in order to unambiguously assign the observed structure to the molecular arrangements on the nanoparticle as opposed to noise (or a convolution of noise and true structure) one must obtain images at different speeds. Because noise typically occurs with a fixed frequency, by varying the tip speed, the periodicity of such noise, as manifested in the map of the substrate, will change proportionally with tip speed, extrapolating to zero at zero tip speed. The molecular spacing on the nanoparticles is constant and the measured spacing should not significantly vary with tip speed; however, it is not unexpected that the image quality will vary. An example of such spacing measurements for nanoparticles and noise as a function tip speed is illustrated in Figure 2.6. As is shown, the noise measurements vary linearly with tip speed and extrapolate to zero. The measurement values of headgroup spacing do vary slightly with tip speed (an effect we believe that is due to the variations in the accuracy with which the tip tracks the sample with increasing tip speed at a set gain), but when fit with a linear line, such a line does not pass through zero. A further example is shown in Figure 2.7 where headgroup spacing as a function of core nanoparticle diameter for octanethiol/mercaptopropionic acid (OT/MPA) 1:1 nanoparticles obtained at two different tip speeds is plotted. As shown, the two plots coincide indicating that the average spacing measurements are not affected by tip speed. Figure 2.8 shows a tip speed experiment for OT homoligand nanoparticles in which variation in image quality is seen to vary with tip speed.

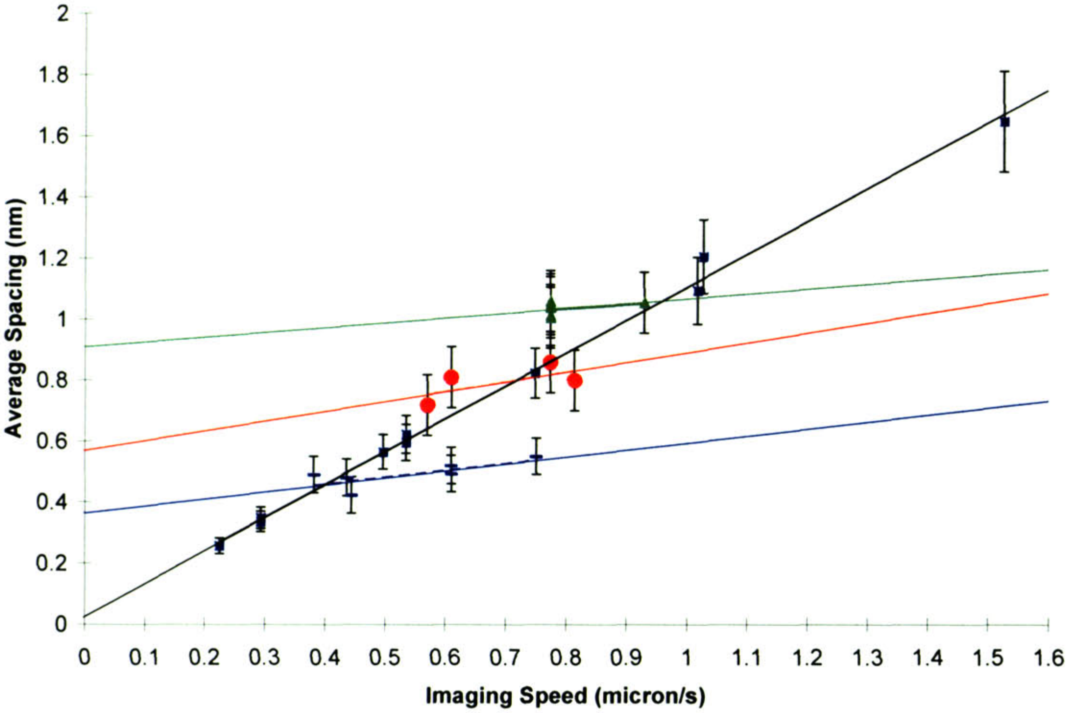

Figure 2.6 Plot of STM observed nanoparticle headgroup and noise peak to peak spacing as a function of imaging speed for various compositions of nanoparticles, with each data set fit by a linear line. Black squares: noise observed on a SAM. Green diamonds: OT/MPA 2:1 nanoparticles. Orange circles: OT/MPA 1:1 nanoparticles. Blue lines: OT/MPA 30:1 nanoparticles. Note that only the linear fit of the noise extrapolates to zero. It is also interesting to note that the slight slope observed for all nanoparticle measurements is roughly equal indicating that tip speed has some effect on the resulting measurement. OT/MPA 2:1 data is taken from that presented in Jackson, A. M.; Hu, Y.; Silva, P. J.; Stellacci, F. *J Am Chem Soc* 2006, *128*, 11135-11149. OT/MPA 1:1, 30:1 and noise data is taken from that presented in Jackson, A. M.; Myerson, J. W.; Stellacci, F. *Nat Mater* 2004, *3*, 330-336, except for the OT/MPA 2:1 data which is taken from: Jackson, A. M.; Hu, Y.; Silva, P. J.; Stellacci, F. *J Am Chem Soc* 2006, *128*, 11135-11149.

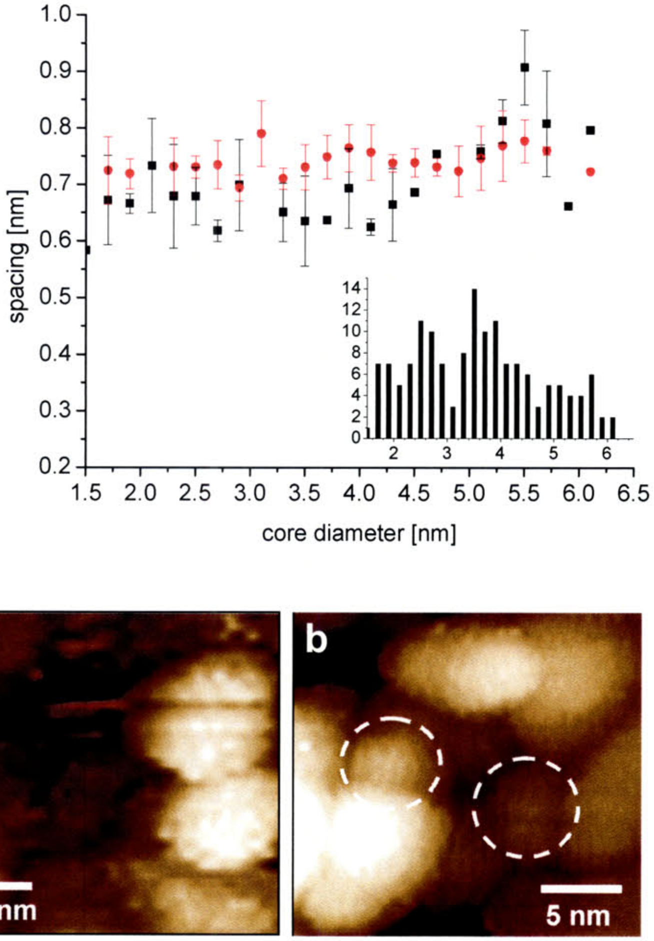

Figure 2.7 Comparison of the STM observed headgroup spacing of OT/MPA 1:1 nanoparticles for varying STM tip speeds. Top: Plot of the observed headgroup spacing as a function of core diameter from two scan images: one taken at 0.57 µm/s (black squares) and the other at 0.814 µm/s (red circles). Note that the error bars are ± 1 standard deviation of the average of all of the average spacings for particles of a given diameter. Inset: histogram of the number of nanoparticles measured per nanoparticle diameter. Bottom: Comparison of Height Images of OT/MPA 1:1 nanoparticles imaged at varying tip speeds. (a) STM height image of a cluster of two nanoparticles showing ripples imaged at 0.57 µm/s. The top particle has a diameter of 5.1 nm and an average ripple spacing of 0.70 nm. The bottom particle has a diameter of 4.8 nm and a corresponding average ripple spacing of 0.67 nm. (b) STM height image of another cluster of nanoparticles imaged at 0.814 µm/s showing a comparable spacing to that in (a). The left, circled nanoparticle has an observed diameter of 4.2 nm and an average ripple spacing of 0.70 nm. The right, circled particle has an observed diameter of 6.0 nm and an average ripple spacing of 0.71 nm. The large particle beneath the smaller, top left particle was not used to determine ripple spacing as its ripples are not easily discernable. It is likely that the nanoparticle is rotated with respect to the scan direction thus obscuring ripple direction.

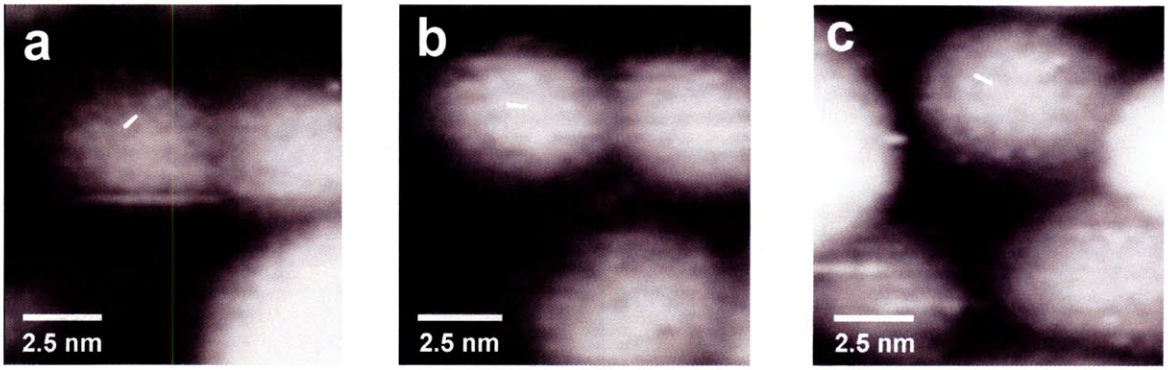

Figure 2.8 STM height images of an OT homoligand nanoparticle monolayer on Au foil illustrating consistency of headgroup spacing with tip velocity, but also showing image resolution changes with tip velocity. (a) Image of a group of nanoparticles whose headgroups are clearly visible when imaged at a tip velocity of 0.695 µm/s. The headgroup spacing on the nanoparticles ranges from 0.57 to 0.60 nm. (b) and (c) Images are of two different areas from a single scan that was imaged at 0.868 µm/s. (b) Image of same particles as in (a). In this case the imaging conditions are no longer optimal, and it is difficult to recognize individual headgroups on the nanoparticle. The few headgroups which can be recognized show a spacing of ~0.6 nm. (c) A separate group of nanoparticles whose headgroups are clearly visible, even at this increased scan speed, and that show spacings from 0.56 to 0.65 nm. The short, white lines in each image represent a single headgroup spacing measurement.

One can also use comparisons between areas of bare substrate and the nanoparticles to recognize noise. For example, with respect to the imaging of ripples, in Figure 2.9 some areas of the underlying gold foil (e.g. within the solid circle) exhibit a curvature comparable to that of the nanoparticle core (e.g. within the dotted circle). While that nanoparticle show clear ripples, no nanostructuring is observed on the gold foil, indicating that ripples are not the result of the STM tip scanning over an area of high curvature. Similarly, one can combine surface/particle comparisons with tip speed variations to recognize noise. For example, as shown in Figure 2.10 which compares spacing on OT/MPA 2:1 nanoparticles to spacing on the gold foil, while the observed features on the gold foil change spacing linearly with tip speed (extrapolating to zero spacing at zero tip speed), the features on the nanoparticles are tip speed independent—indicating that they represent the true nanostructuring. Note that often these two types of features—tip speed dependent and tip speed independent—also show different amplitudes, with independent features showing a greater amplitude and thus dominating the signal on the particles and noise only being seen on the substrate where there is no nanostructuring that can dominate the noise. This technique is useful for characterizing any underlying noise in the signal so that it can be recognized.

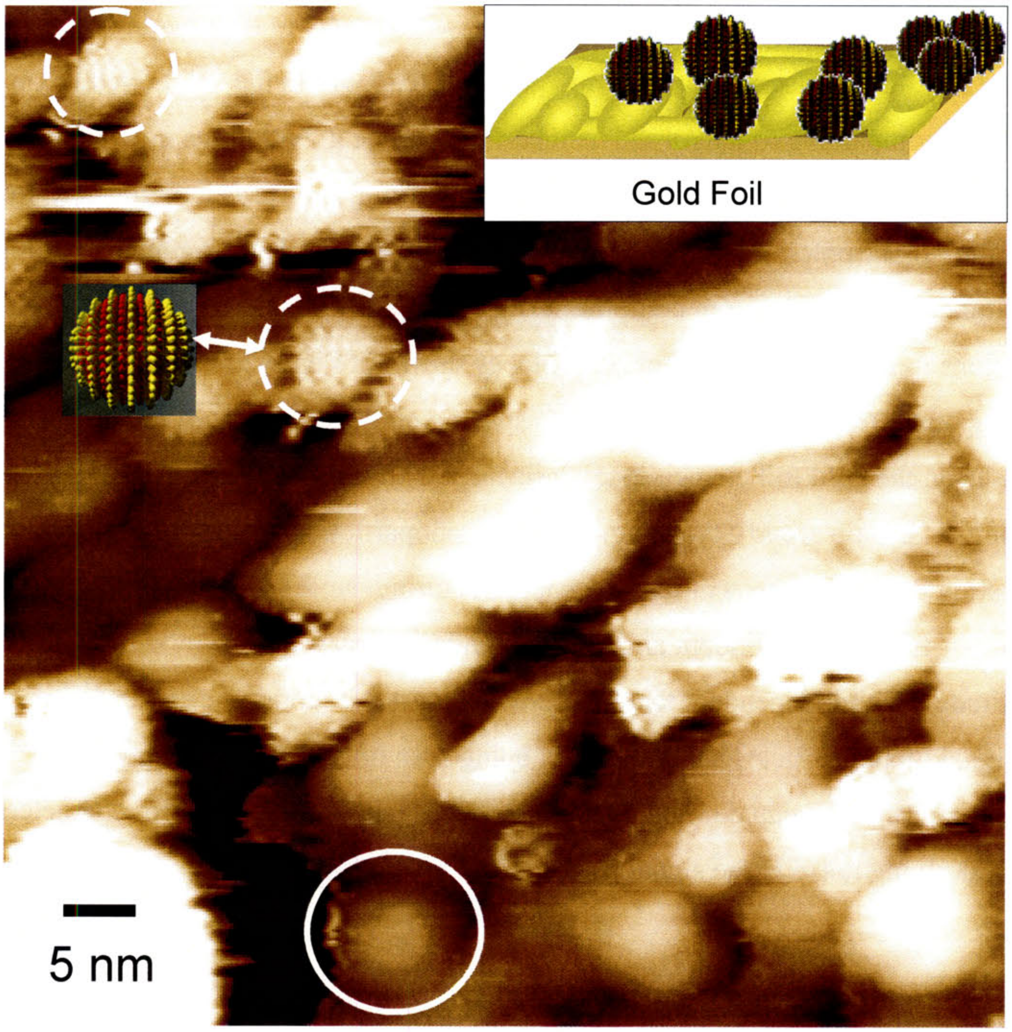

Figure 2.9 STM images of OT/MPA 2:1 gold nanoparticles (two are indicated by dotted circles) on a gold foil substrate. A feature that one should recognize in the image is that, while in some areas (such as the one demarcated by the solid white circle) the underlying gold foil exhibits a curvature comparable to that of the nanoparticles, no hint of ripples is observed, indicating that ripples are not the result of the STM tip scanning over an area of high curvature.

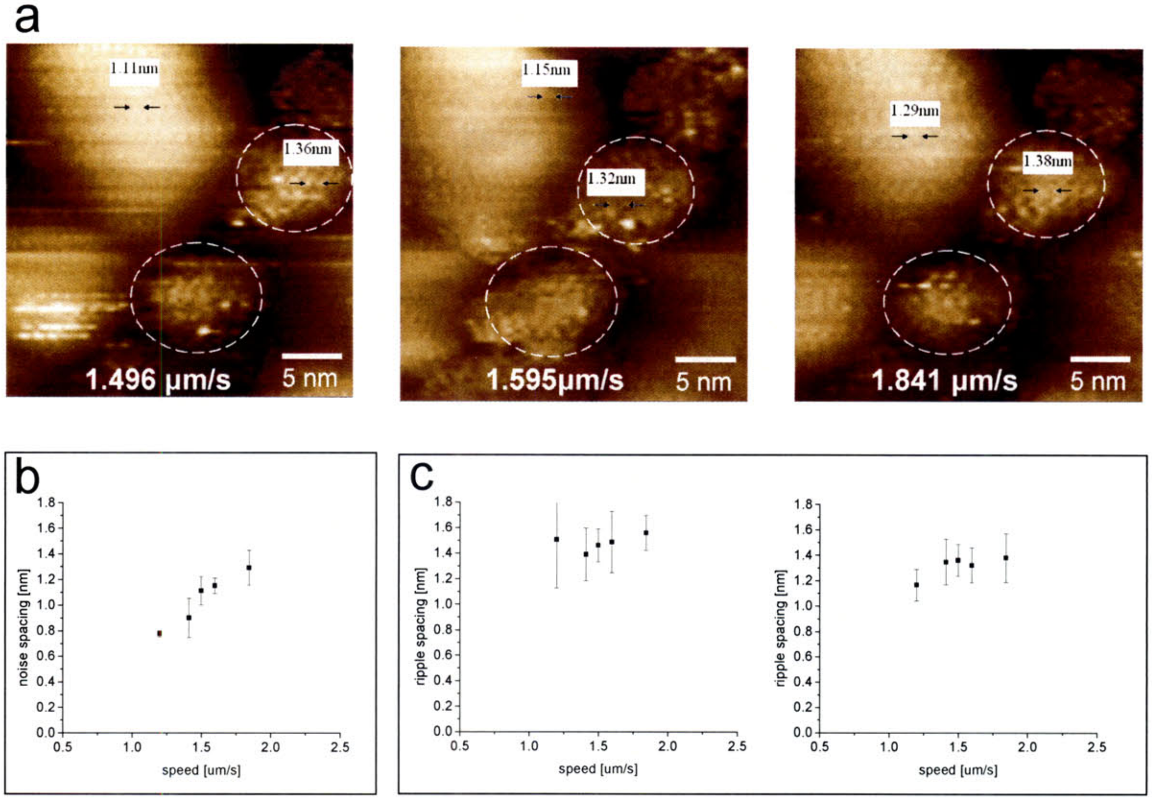

Figure 2.10 (a) STM images of two (circled) OT/MPA 2:1 gold nanoparticles cast onto a gold foil substrate. These images show how, at times, ripples can look similar to noise in our images, but, when comparing images taken at different tip speeds, it is apparent that ripple spacing remains constant while noise spacing scales linearly with speed. Spacing measurements at three different tip speeds for one of the nanoparticles and for the gold foil are indicated on the three images. (b) Plot of spacing measurements as a function of tip speed for the noise, and (c) for the ripples of each particle. It is immediately obvious how different the behavior is in the two regions. Also, it was noted that the amplitude (height from peak to trough) of the ripples was much greater than that of the noise. Being that the measurements are taken on the same images, effects of gains and other imaging parameters are excluded. Each point in the plots is the average of multiple measurements; the calculated standard deviations are shown as error bars in the plot. Images courtesy of Dr. Ying Hu.

2.7. Image analysis

2.7.1. Measurement of headgroup spacing

As a first step in understanding the structure of the ligand shell, we first describe the measurement and assignment of headgroup spacing and molecules. A typical homoligand nanoparticle showing headgroups is shown in Figure 2.8. Homoligand nanoparticles are significantly more difficult to image than mixed ligand particles, due to the lack of height and chemical contrast between ligands. Headgroup spacing is defined as the distance between one headgroup and its nearest neighbor as measured from the peak to peak spacing. Typically several measurements between clearly visible headgroups located near the center of the particle are taken and then averaged, giving an average headgroup spacing for each specific particle. Spacing measurements taken at particle edges are more subject to tip/sample distortions, and due to geometric considerations, may not be representative of the actual molecular configurations. Also, due to line scan artifacts and possible sample drift, which can distort the nanoparticle image, measurements should be taken as close to possible to the fast scan direction—horizontally, across the nanoparticle. One should note that often there are defects in the image of the ligand shell—either due to tip or external environmental effects during STM imaging or to a defect in the 3-D monolayer—which we may or may not recognize. While these defects clearly influence the nearest neighbor distance measurements, it is necessary to include them as they may be a natural variation in the monolayer structure.

In the case of mixed ligand nanoparticles, the measurement process is similar to that of homoligand nanoparticles. Due to the height difference that is often present between the two types of ligands, typically only one of the ligands is observed. There are generally two ligand shell morphologies that we have observed for mixed ligand nanoparticles: 1) a porcupine type morphology with 'patches' of one molecular type within a sea of the other—similar in morphology to homoligand nanoparticles, and 2) a 'rippled' morphology in which the SAM phase separates into ordered, ribbon-like domains of alternating composition that encircle or spiral around the nanoparticle core (Figure 2.9). In both cases, we typically assign the taller in height molecule to the longer ligand and shorter in height to the shorter ligand. This conclusion was reached based on flat surface studies of the same molecules. In the case of the 'patchy' particles, these particles often look very similar to homoligand ones and the headgroup spacing is measured as is for homoligand particles. For the rippled case, the ripple spacing is used as the characteristic measurement, which is defined as the peak-to-peak spacing from one ripple to the adjacent ripple of the same height. Thus ripple spacing is measured perpendicular to the ripple direction.

2.7.2. Measurement of nanoparticle diameter

While headgroup (or ripple, in the case of mixed ligand particles) spacing can be measured with relatively high accuracy (typical within 0.5 Å), nanoparticle diameters are considerably more difficult to determine. This is due to several factors: the 'soft' nature of the ligand shell, the possible interdigitation of ligand shells between neighboring particles, the large height difference between nanoparticle and substrate, and any other tip/sample convolution effects. All of these factors make precise determination of the ligand shell borders challenging. Through multiple measurements on various particles it was determined that the best achievable resolution is 0.2 nm (typically 2-5% of the total ligand shell diameter).

2.7.3. Interpretation of domain structure

As mentioned previously, just as it is difficult to reconstruct an object from its topographic map, it is often equally difficult to reconstruct the ligand shell structure from its STM image. In order to determine the molecular arrangements within the ligand shell, it is important to be able to understand how the tip/sample convolution contributes to the resulting image. Examining the image in Figure 2.11 of a sparse monolayer of rippled nanoparticles, it is evident that those nanoparticles which show the clearest ripples, have domains which are oriented nearly 90° (±30°) to the fast scan directions (that is the ripple direction is vertical in the image and parallel to the slow scan direction). However, the remaining nanoparticles scattered across the surface clearly show nanostructuring in their ligand shells, but clear ripples cannot be discerned (Figure 2.11d). We believe that these nanoparticles are rippled, but due to their orientation with respect to the fast scan direction, cannot be clearly resolved.

The inability of STM to clearly image ripples when not oriented perpendicular to the fast scan direction can be understood through consideration of how the tip scans across the surface and the resulting image is generated, as illustrated in Figure 2.12. When imaging particles whose ripples are rotated so that they are not perpendicular to the fast scan direction, the imaging scan lines, when merged to form an image, can produce what appears to be two sets of crossing ripple directions, resulting in a cross-hatched appearance on the nanoparticle ligand shell. In order to experimentally demonstrate this effect, as shown in Figure 2.12, we first imaged a sample at 0° scan angle and obtained clear, well resolved images of a nanoparticle whose ripples run perpendicular to the fast scan direction. We then rotated the sample by 30° and found that the particle's ripple direction was now difficult to discern and exhibits the typical 'cross-hatching' of a rotated particle.

Note that obtaining molecular resolution images of the same region of a sample as it is rotated is extremely challenging and requires the confluence of several factors. 1) There must be minimal sample drift so as to image the same region. 2) The original image must be optimal, showing molecular resolution, for comparison with the rotated images. 3) As the sample is rotated, the tip must be able to track the surface along each new direction—that is, topographical hindrances due to large clusters of particles must not be introduced along the new tip scan path. It is often the case that during rotation, one sample region will lose clarity while another will become more resolved due to changing scan paths and ripple orientations, making comparisons between images difficult. In sum, understanding how the tip tracks the surface and how an image is generated from subsequent scan lines is critical in understanding the resulting height images and interpretation of such images to determine their actual molecular configurations.

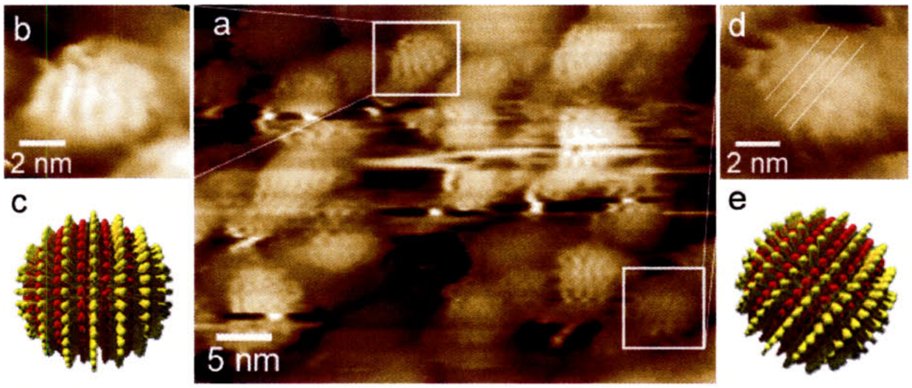

Figure 2.11 (a) STM height image of OT/MPA 2:1 mixed ligand nanoparticle monolayer on Au foil showing ripples in various orientations. (b) Enlarged image of a single nanoparticle and corresponding schematic drawing, (c), showing molecular domains that align into parallel ripples that encircle and/or spiral around the nanoparticles. The spacing of the phases, measured as the average spacing between two peaks is 0.89 nm. (d) Enlarged image and corresponding schematic drawing, (e), of a nanoparticle with ripples oriented ~45° to the fast scan direction. This rotation results in reduced visualization of the particle's ripples.

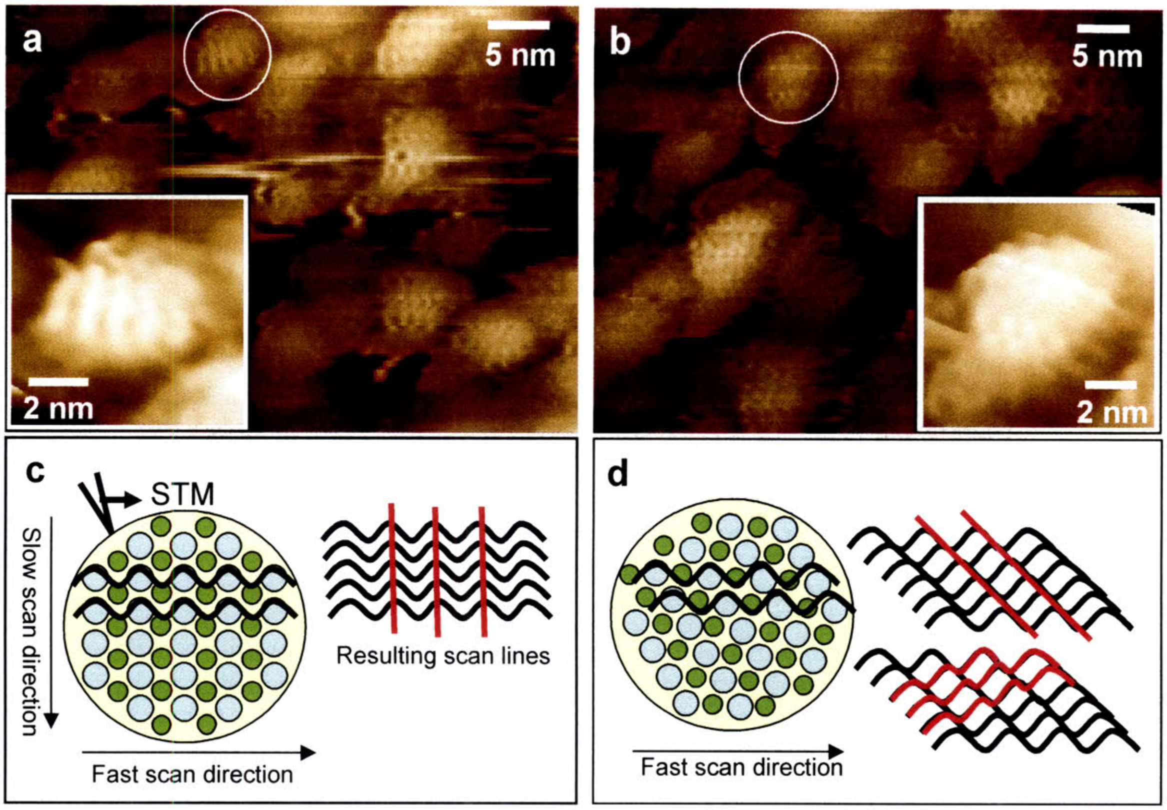

Figure 2.12 (a) STM height image of OT/MPA 2:1 nanoparticle monolayer taken at 0° scan angle. Inset: Enlarged image of a single nanoparticle showing ripples running perpendicular to the fast scan direction. (b) STM height image of the same sample as in (a) imaged at 30° scan angle. Inset: Enlarged image of the same nanoparticle as in (a); however, ripple direction is now difficult to discern. (c) Schematic drawing of STM imaging of the ligand lattice on a nanoparticle where the blue and green dots represent a phase-separated 'rippled' arrangement of two different ligands; the drawing illustrates the resulting scan lines and ripple direction seen (shown in red) when ripples run perpendicular to the fast scan direction. (d) Similar schematic drawing as in (c); the ligand shell molecular lattice has been rotated by 30° resulting in two possible ripple directions being seen, and giving rise to the characteristic 'cross-hatched' appearance on the particle when the two ripple directions are overlaid.

2.8. Conclusions

It can not be emphasized enough the role that the cleanliness of nanoparticles and the tip plays in obtaining molecular resolution images. While parameters such as tip speed and gains can be adjusted to improve an image, they are not sufficient for observing the molecular structure. Furthermore, one must always keep in mind the effect of tip/sample convolution and noise on the observed nanoparticle structure, obtaining multiple images at various scan speeds and with different tips to be able to make an informed decision on the ligand shell morphology. Lastly, obtaining molecular scale resolution images on nanoparticles is extremely challenging, not only in regards to the required optimization of sample preparation of the particles from synthesis to substrate, but in that we are pushing the limits of the STM. However, in pushing these limits, we are also seeing and discovering structures and phenomena that have never been observed before—we are at the nanofrontier.

2.9. References

1. Waters, C. A.; Mills, A. J.; Johnson, K. A.; Schiffrin, D. J., Purification of dodecanethiol derivatised gold nanoparticles. *Chemical Communications* **2003**, (4), 540-541.

2. Song, Y.; Heien, M. L. A. V.; Jimenez, V.; Wightman, R. M.; Murray, R. W., Voltammetric detection of metal nanoparticles separated by liquid chromatography. *Analytical Chemistry* **2004,** 76, (17), 4911-4919.

3. Zheng, N.; Fan, J.; Stucky, G. D., One-step one-phase synthesis of monodisperse noble-metallic nanoparticles and their colloidal crystals. *Journal of the American Chemical Society* **2006,** 128, (20), 6550-6551.

4. Gupta, P.; Loos, K.; Korniakov, A.; Spagnoli, C.; Cowman, M.; Ulman, A., Facile route to ultraflat SAM-protected gold surfaces by "amphiphile splitting". *Angewandte Chemie-International Edition* **2004,** 43, (4), 520-523.

3. STM Investigation of the Ligand shells of Homo-Ligand and Mixed-Ligand Monolayer Protected Metal Nanoparticles

3.1. Introduction

In this chapter we will focus on the two fundamental and interesting questions that arise when considering SAM structure on nanoparticles: First, how do SAMs on nanoparticles vary from those on flat surfaces, and if so, why? Which presupposes the second question: how do we study such 3-D monolayers? While there is an extensive body of knowledge of the driving forces, energetics of, and resulting molecular packing arrangements of 2-D SAMS, little is known of how the unique shape, surface energetics, and nanoscale confinement affects the resulting monolayer on the nanoparticle core. Studies done to date have found that SAMs (with alkyl ligand lengths > C_{10}) on nanoparticles do show similarities to SAMs on flat surfaces, with ligands exhibiting a high degree of chain ordering and crystalline-like packing.[1-3] However, several important differences have been noted, including increased ligand packing density and greater conformational freedom for shorter ligands (< C_8).[3] It is important to note that these experimental findings are average *ensemble* properties determined over large numbers of particles as opposed to single particle data. It is well known that the size, shape and crystallinity of nanoparticles are not uniform within each synthesized batch of particles. Unlike flat surfaces which can be uniformly (111) or (100), we can expect that each nanoparticle provides a slightly different, high energy, defect-rich substrate with various (111) and (100) facets for the ligands to arrange on and around, resulting in numerous variations of monolayers. Indeed, on the computational studies front, several studies have illustrated the importance that the nature of the core, as well as the type of ligands, play in determining the overall ligand shell morphology.[4, 5] We show here that it is not unexpected to find such a unique ordering and packing of molecules around the nanoparticle core due to curvature and crystallographic effects.

In this chapter we develop an understanding and model of the ligand arrangements around the nanoparticle core using scanning tunneling microscopy (STM). STM is unique among characterization tools in its capability to allow for single molecule visualization, allowing us to study the ligand arrangements on individual particles.[6-8] [9]

This technique has been applied extensively for understanding packing within 2-D SAMs.[10, 11] Indeed, phase separation in mixed ligand monolayers had only been postulated and was neither confirmed nor studied until the advent of STM.[12] Thus, while other characterization techniques can contribute a variety of knowledge and understanding to SAMs, only STM allows for a direct, single particle specific, visualization of SAM packing.

Our course of study is as follows: In order to first understand what role the curved nanoparticle core substrate plays in the packing of the ligands, we start by examining the most theoretically simple (yet most difficult to image) system, homoligand nanoparticles. Using these STM studies and results, combined with the body of knowledge that has been provided by other characterization techniques and studies of 3-D monolayers presented in the literature, we begin to develop a simple model of ligand shell packing. We show that the core curvature (and correspondingly, the changing facet to edge ratio on the core) of the particles is the dominant driver for the packing and behavior of both homoligand and, as we later demonstrate, two-component (or mixed) ligand monolayers. Most interestingly, we find that the molecular headgroup spacing on nanoparticles is greater than that observed on flat Au(111), and that this spacing is not constant with particle diameter, but increases.

Moving to mixed ligand nanoparticles, we find that the ligand shell packing structure deviates significantly from that on flat surfaces—presenting highly-ordered phase-separated domains on the curved surface of the core (see Figure 3.1).[13] It is well understood that 2-D SAMs composed of specific mixtures of ligands (typically those that vary in end-group functionality and length) phase-separate into single component, roughly circular domains of varying size,[a] with no long range ordering (Figure 3.2).[12, 14-16] However, we find that when some of these same mixed SAMs are assembled around the highly curved core of a nanoparticle, the ligands phase-separate into *ordered, ribbon-like domains,* only a few molecules in width[13] of alternating composition that encircle the core (Figure 3.1). We show that both the domain morphology and width can be controlled through the ligand shell composition and the particle core size.

---

[a] We note that recent studies by our group have further demonstrated the ability to both align and to form 'worm-like' domains through modulation of substrate stress.

Probing more deeply into the effect of curvature on molecular arrangements and ordered phase separation, we present a comprehensive study of octanethiol /mercaptopropionic acid (OT/MPA) mixed ligand nanoparticles of varying composition, correlating STM observed domain spacing to core diameter. We find that while for all compositions the domain spacing increases with diameter, it does so in a non-monotonic manner with regions of decreasing spacing separated by transitional, discontinuous increases in domain spacing. We propose that this 'saw-tooth like' spacing behavior is related to changes in the preferred crystal structure of the nanoparticle core with size.

The following chapter is organized as follows: in Section 3.2 we begin by presenting two basic ligand shell models which will be used to guide our interpretations of the ligand shell data. Sections 3.3 and 3.4 describe our experimental STM results on homoligand and mixed ligand nanoparticles, respectively, along with discussion of ligand ordering and packing for each particle type and the development of an improved ligand shell model. Section 3.5 details our ultrahigh vacuum, low temperature STM results on mixed ligand particles. In 3.6 we discuss our experiments and observations on the modulation of and driving forces for phase-separation on mixed ligand particles, followed by a discussion of the theoretical basis for ordered phase separation in Section 3.7. Lastly, all experimental procedures and detail are presented in Section 3.8.

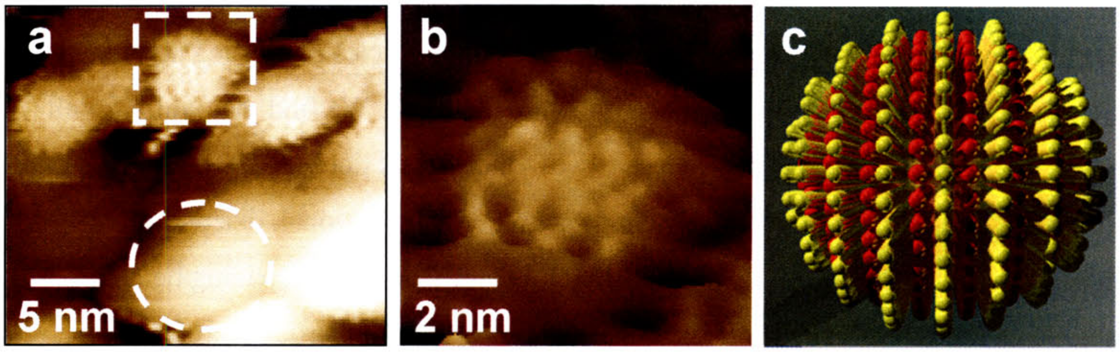

Figure 3.1 (a) STM height image of gold nanoparticles, on Au foil, coated with a 2:1 molar ratio of octanethiol (OT) and mercaptopropionic acid (MPA) showing ribbon-like stripes, hereafter called ripples, due to the phase separation of the two ligands. One such particle is outlined by the dotted square and shown in an enlarged image in (b). The raised domains that run across the particles are the OT phases which alternate with the MPA phases. A schematic drawing to help the reader visualize this three dimensional arrangement is shown in (c).

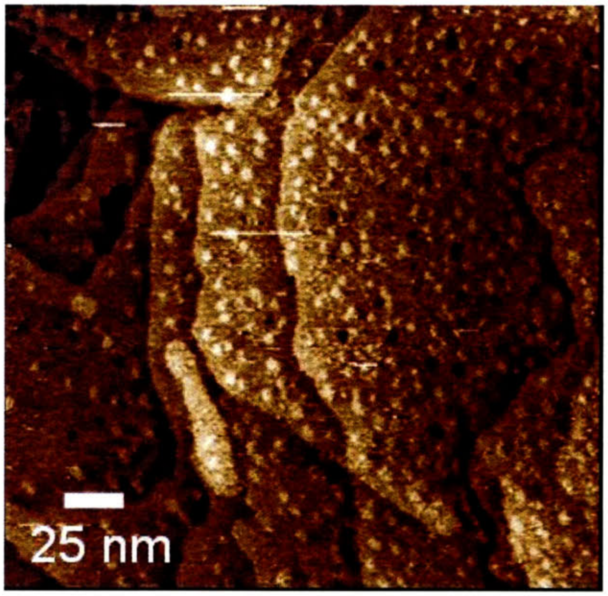

Figure 3.2 STM height image of OT/MPA mixed monolayer on Au(111) showing randomly distributed phase-separated domains. We attribute the taller, bright domains to OT, and the surrounding regions to MPA.

3.2. Models for ligand packing

STM images provide a 'bird's eye' view of the nanoparticle from above; we see only the treetops of the molecules, and so must infer how their trunks are arranged on the core below. As a starting point, and in order to provide a guide for interpretation of STM images and results, we first develop a basic model of the ligand shell, and of the ligands themselves, around the nanoparticle core, linking headgroup configuration to sulfur group packing on the core. Such a model should take into account the unique effects and configurations that the nanoparticle core imposes on the ligand shell system. There are three main effects to consider. 1) **Nanocrystal core/Commensurate effect**: adsorption sights and packing of thiols depend on the structure of the underlying gold surface.[5] Depending on the nanoparticle size, the core presents a variety of highly faceted, high energy, high defect density surfaces. Thus we expect that ligands will not see the core surface as a highly ordered (111) plane, but more as a 'poly-crystalline' high defect density substrate made up of small (111) and (100) planes, and will arrange themselves accordingly. 2) **Splay effect**: as the nanoparticle decreases in diameter the radial free volume increases significantly from the core surface outwards allowing greater conformational freedom for ligand headgroups. 3) **Topological or Curvature effect**: the nanoparticle core is equivalent to a topological sphere,[b,17] and the spherical symmetry of the core results in a packing constraint on our system. While the most efficient packing motif for hard spheres on a flat surface is hexagonal packing, on a sphere, it is not possible to achieve hexagonal packing without the introduction of defects into the lattice, resulting in a change in packing structure[18] (see Section 3.7 for further discussion).

In reviewing the literature, there are two central, basic models for ligand packing, each of which weighs the above factors to varying degrees and which we will subsequently refine; we refer to these models as the **crystallographic model**, (Figure 3.3a), which is based on that presented by Murray and coworkers,[19] and the **continuous model** (see Figure 3.3b for a drawing adapted from Luedtke and Landman).[20] The crystallographic model is the simplest and most similar to the 2-D, flat surface model. It

---

[b] The facetted crystalline core is topologically equivalent, or homeomorphic, to a sphere: that is, the polyhedral core can be deformed through a bicontinuous transformation, i.e. stretching without tearing or gluing, into a sphere. Thus, those topological principals which hold for spheres will hold for all homeomorphs of the sphere.[17]

views the nanoparticle core as a faceted single crystalline structure composed of (111) and (100) facets.[21] The ligands arrange on each facet as they would for a 2-D monolayer with a 33% ligand packing density (defined as the number of sulfur atoms to gold surface atoms—each sulfur atom sits at a 3-fold hollow site, giving 1 ligand per 3 gold atoms =1/3 or 33%). As illustrated in Figure 3.3a, the headgroup spacing of neighboring ligands (**N**) is equivalent to that of the sulfur spacing of those neighboring ligands at the core (**x**). However, one refinement must be made to this model—it is known that the packing density of ligands on nanoparticles is close to 50% or more depending on core size.[1] We can rectify this discrepancy with the model by considering that we have included only ligands located on the facet faces and have neglected those on edges. Ligands on edge sites should be able to pack with their sulfur groups closer together, than as compared to facets, due to the greater overall free volume at the edges. If we assume that ligands on edge sites pack with a density of 100% (1 ligand per edge atom), then a 2 nm particle, which has 174 surface atoms, ~22% of which are edge sites, will have an overall packing density of ~48%, corresponding to that observed experimentally.[22] Note that with the inclusion of ligands at edge sites, the *average* headgroup spacing will now have some dependence on diameter due to the changing facet to edge ratio. As the particle size increases, the ratio of terrace to edge sites increases, decreasing the overall degree of crowding, and thus, the average headgroup spacing should increase slightly (with a corresponding slight increase in sulfur spacing on the core) with diameter toward its value on flat (edgeless) surfaces.

The alternate model which we consider is the continuous model. Here the core is viewed as its topological homeomorph—a sphere. The inherent increase in free volume radially outwards from the core, allow for a tightly packed sulfur group configuration on the surface, with headgroups splaying outwards from core. This packing scheme leads to a greater ligand packing density than that which results on flat surfaces. This expectation has been experimentally confirmed by Murray who observed an increasing packing density with decreasing core size.[19] In this model, headgroup spacing (**S**) is related, to first order, to the spacing of the corresponding sulfur atoms (**x**) at the gold nanocrystal surface by the geometric relation: **N/D** = **x/d** where **d** is the particle diameter and **D** is the total STM observed diameter of core plus ligand shell, **D** = **d+2L,** where **L** is the ligand length. According to this model, as the core diameter increases, the resulting free volume available to the headgroups decreases, thus resulting in a sulfur-sulfur spacing which increases towards that observed for flat surfaces. Now armed with these two models, we can begin to interpret and understand the STM derived data of ligand packing on nanoparticles.

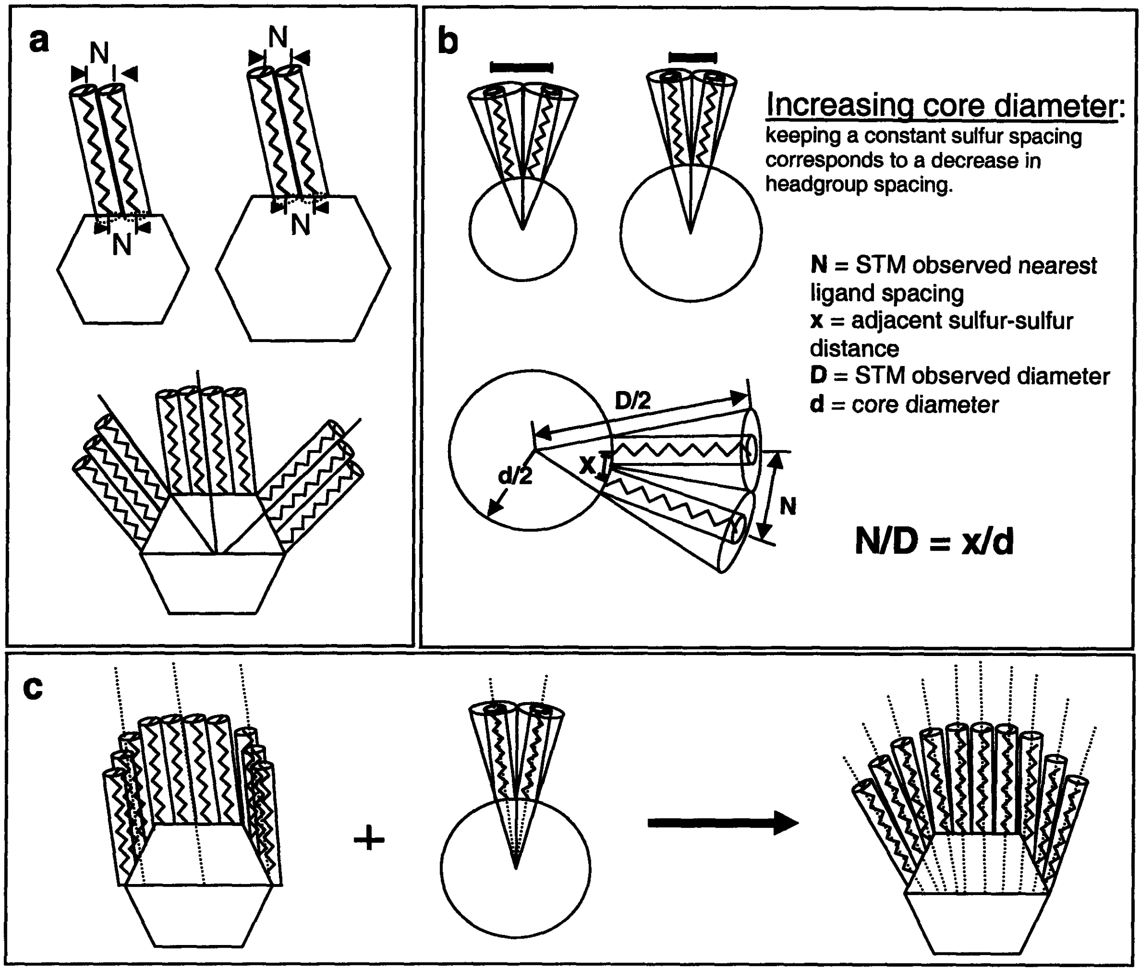

Figure 3.3 (a) Simplest representation of ligand packing for homoligand nanoparticles. Ligands pack on each nanoparticle facet as they would on a crystallographically equivalent flat 2-D gold surface, with a headgroup spacing corresponding exactly to the sulfur-sulfur spacing of the ligands at the nanoparticle core. Note, that for this representation, increasing the core diameter of a nanoparticle results in only an increasing facet size which should not affect ligand spacing or packing. Furthermore, assuming that each facet is independent of one another and ligands assume their optimal tilt angle with regards to each facet, high energy grain boundaries at the crystal edges are formed leading to a high energy configuration (b) Schematic illustration of a ligand coated nanoparticle relating the STM observed nearest headgroup spacing (N) at the periphery to the corresponding sulfur-sulfur spacing (x) at the nanoparticle core. The nanoparticle is modeled as having a spherical core of diameter d, surrounded by a ligand shell of constant length L, with an STM observed diameter D (= d +2L). The ligand length is approximated using the relation for a fully extended chain with n carbon atoms: L=0.12 (n+1) [nm]. Note that increasing the core diameter, while keeping sulfur-sulfur spacing constant, results in a decrease in headgroup spacing. (c) The true ligand configuration is likely a combination of the modified crystallographic representation, where ligands assume a global tilt angle over each hemisphere (note that this is still a constrained, higher energy configuration due to the non-equilibrium tilt angles over many of the facets), together with the continuous, space filling continuous model of (b) which takes into account the curvature of the particle and allows for the ligand to take advantage of the free volume available to headgroups. The result is a model that takes into account the crystallographic nature of the core and the optimizes ligand density with the ligands roughly conforming to a global tilt angle, but relaxing, and splaying outwards to better accommodate their preferred tilt angles and to increase their headgroup spacings, as shown in the right most drawing in (c).

3.3. STM investigation of ligand packing on homoligand nanoparticles

3.3.1. Results

In order to determine what role the core curvature and spherical symmetry play in driving the resulting ligand shell structure, we carried out an investigation of ligand ordering as a function of core diameter on homoligand nanoparticles. Such particles are free from the additional packing constraints added by phase separation in mixed ligand particles, but are extensively more difficult to image due to the lack of chemical and height difference between neighboring ligands. OT coated Au nanoparticles were synthesized using both 1-and 2-phase methods. Shown in Figure 3.4 are STM height images of such OT particles. Each figure shows a single nanoparticle, with the methyl headgroups of the particles' ligand shell visible as the raised, bright dots on the curved particle surface. We note that the particles appear smoothly curved, with no obvious faceted nature. Headgroups appear most clear near the center of the particle, due to geometrical considerations and tip effects which can occur at the particle's boundaries, and present an average head group spacing of ~0.5 nm. TEM and STM measurements give a core size distribution ranging from approximately 2 to 7 nm.

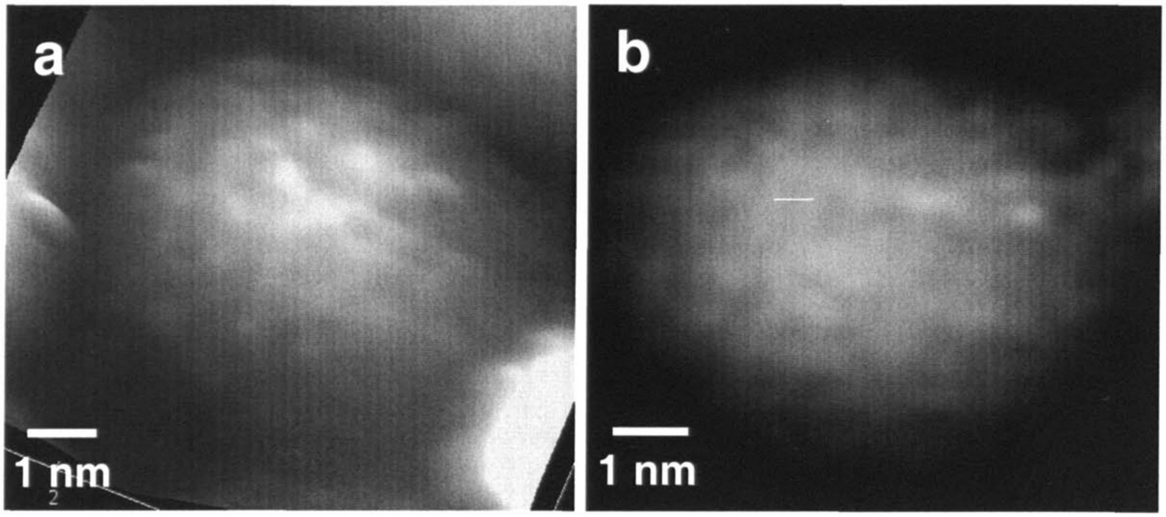

Figure 3.4 STM scan images of OT homoligand nanoparticles. (a) 3-D rendering of a homoligand nanoparticle in which the molecular headgroups are clearly visible. (b) Example of a single headgroup spacing measurement. Several measurements were taken on each nanoparticle between clearly visible headgroups near the center of the particle. The measurements were typically taken horizontally between headgroups in order to minimize the effects of line scan artifacts or vertical drift during the imaging of the particle.

To determine what role the curvature of the core plays in determining ligand packing, we plot the observed nearest neighbor headgroup spacing (**N**) as a function of core diameter (**d**) as measured from several STM scan images (Figure 3.5). **d** is determined using the relation: **d**=**D**-2**L**, where **D** is the experimentally measured nanoparticle diameter (core plus ligand shell), and **L** is the ligand length. We numerically calculate **L** by modeling the ligand as an all-trans (as supported by FTIR[1]) alkyl ligand chain with n carbon atoms, and use the relation **L** = 0.12 (n+1) [nm] to estimate the molecular length.[23] As shown in Figure 3.5b, the average headgroup spacing of the OT homoligand nanoparticles increases with diameter from a value of 5.0 Å at 2.7 nm diameter to 6.0 Å at 5.1 nm core diameter, with an average value across all particles of 5.4 Å. Average headgroup spacings were calculated from the raw, individual nanoparticle data (Figure 3.5a) by averaging all of the individual spacing measurements from particles within a set diameter range (e.g. from 4-4.2 nm, 4.2-4.4 nm, etc., with each set covering a diameter range of 0.2 nm—determined to be the accuracy to which the particle diameter can be determined by STM (see Section 3.6.1). For the raw spacing data, at least 3 measurements per particle were taken with a typical calculated standard deviation per measurement of 0.3-1 Å. The plotted error bars shown in Figure 3.5b are ±1 standard deviation of the average spacing.

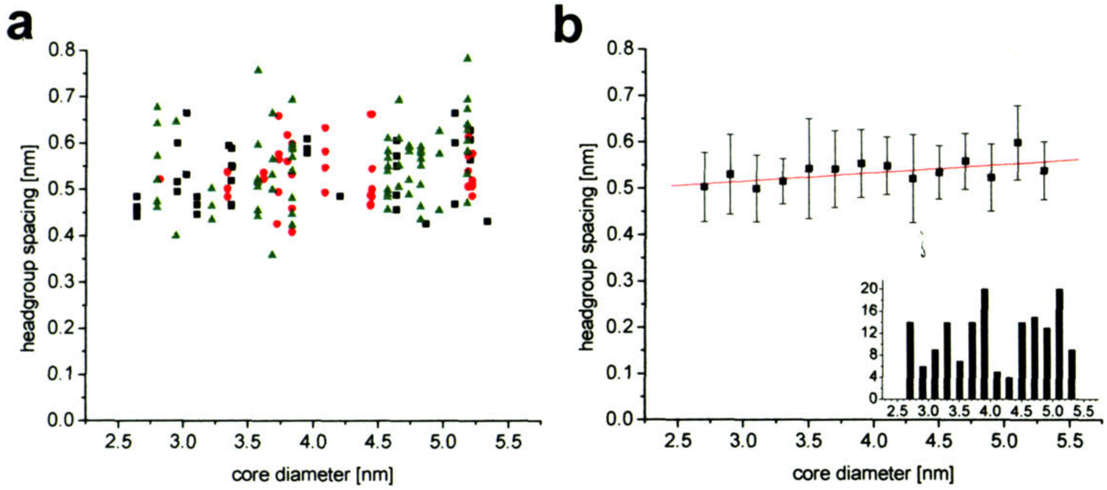

Figure 3.5 (a) STM headgroup spacing data from three scan images of OT homoligand nanoparticles as a function of core diameter: red circles, two-phase-synthesized nanoparticles, imaged at 0.868 mm/s; black squares, two-phase-synthesized nanoparticles imaged at 0.695 mm/s; green triangles, one-phase-synthesized nanoparticles imaged at a tip speed of 0.861 mm/s. (b) Averaged data from (a) showing a slight increase in headgroup spacing with core diameter. Note that the number of raw spacings averaged to obtain each data points varies due to the inherent polydispersity of particle sizes resulting from the synthesis. We also note particles of certain diameters are absent or rare in our images; this may be related to crystallographic reasons or to sample preparation issues. The red line is a linear fit to the data. The regression has statistical significance with a 99% confidence level ($R = 0.299$, DOF = 164, $R_{100} = 0.254$); the slope of the fit (2.7×10^{-2} nm/nm) is also significant with a 99.9% confidence level ($t = 3.99$, DOF = 164, $t_{120} = 3.37$). Inset: Histogram of the number of spacing measurements per nanoparticle core diameter.

3.3.2. Comparison of homoligand nanoparticle results to 2-D SAMs

The above images and resulting plots demonstrate that octanethiol 3-D monolayers on nanoparticles show significant differences in packing as compared to their 2-D counterparts on flat Au(111) and (100) surfaces[24, 25]—most notably in regards to their spacing magnitude and behavior. On Au(111), the molecules pack in a hexagonal lattice with an inter-chain spacing of 5.0 Å;[11, 16] on flat Au (100), the packing is still debated, with experimentally observed inter-chain distances ranging from 4.54 Å, for a square lattice,[26] to 5.77 Å and 4.81 Å, for a distorted, hexagonal lattice. The observed averaged headgroup spacing of 5.4 Å, although close to, matches none of the flat surface values—a somewhat expected result as nanoparticles are made up of both (111) and (100) facets and are high energy, strained surfaces with many defects. Additionally, the fact that an increase in headgroup spacing with particle diameter is observed (Figure 3.5) clearly indicates that the packing of the ligands on each facet is not equivalent to that on a flat surface, in which case no spacing dependence on core diameter should be observed.

3.3.3. Interpretation of homoligand nanoparticle results using shell models

To determine the actual packing arrangements of the ligands around the core from the STM images, it is necessary to consider how the observed headgroup spacing correlates to the sulfur arrangements below on the core. The two models, crystallographic and continuous, translate the observed headgroup spacing to sulfur spacing differently, predicting different spacing behavior with changes in core diameter. Thus, we consider our data (both headgroup and resulting sulfur spacings) in light of each model separately.

3.3.3.1 Crystallographic Model

Using the crystallographic model, the sulfur spacing (**x**), is to first order (ignoring the effect of edge sites), equivalent to head group spacing (**N**). Increases in both headgroup and sulfur spacing with diameter (Figure 3.5) are expected from the crystallographic model. However, the magnitude of the spacing values are 10% larger than those values on flat surfaces—a result that does not agree with the crystallographic model nor experimental data on ligand packing density!

Furthermore, if we consider that according to the crystallographic model, ligands pack on each facet as they would on a flat surface—forming a sort of 2-D crystal with all ligands conforming to a single tilt angle (thus maximizing their van der Walls interactions)[25]—this implies that each facet constitutes an independent 2-D monolayer, each with a different ligand tilt angle (relative to a single coordinate system). Thus, the facet edges become high energy grain boundaries between adjacent SAM domains—an extremely high energy configuration (Figure 3.3a). It is well know that molecules within a 2-D SAM attain a single tilt angle to maximize their interactions, and that this tilt angle is only weakly dependent on the underlying gold substrate structure.[25] Indeed, often there are several possible tilt angles with minimum energies.[25] This suggests a further refinement to the crystallographic model be made—one that remedies the creation of high energy grain boundaries. On a nanoparticle, the thermodynamic driving force for maximizing ligand interactions still holds, and we expect that in order to minimize the global free energy, SAMs on different facets would adjust and align their tilt angles to increase global ligand interactions, resulting in a more homogeneous packing of ligands on different facets and edge sights. As similar configuration was presented by Landman and coworkers who found that below the ligand shell melting temperature, ligands assume a single tilt angle over one hemisphere of the core regardless of facet orientation;[4] such a configuration is shown in Figure 3.3c (left). This configuration is not entirely unexpected, nor energetically difficult to achieve, given the high defect density and high energy nature of the nanoparticle core surface. Other molecular dynamics simulations have also hinted at such 'smoothing out' of the facets by finding that alkanethiol molecules induce an isotropic surface energy, resulting in a somewhat rounded shape of the particle.[5] Furthermore, our[13] and others'[7, 27, 28] STM images on nanoparticles show them to be roughly spherical, suggesting that the ligand arrangements do not strictly conform to the faceting of the core. However, the inability of the crystallographic model to correctly predict the sulfur spacing still remains even with these refinements. Thus, while the crystallographic model captures the spacing behavior, it fails to capture the observed magnitude of spacing values and breaks down when held up to thermodynamic scrutiny due to its simplistic vision of ligands packing on each independent facet as they would on a flat surface

3.3.3.2 Continuous Model

If we instead consider the homoligand spacing data in light of the continuous model, we derive the sulfur spacing using the relation presented previously: **N/D = x/d**. The plot of sulfur spacing vs. core diameter is shown below in Figure 3.6. As shown, the resulting spacing, **x,** separates into two regions, each of relatively constant value, from 2.3 to 3.3 nm and 3.5 to 5.5 nm core diameter, with average spacing values <x> of 3.2 Å and 3.8 Å, respectively. The resulting range of values of the average sulfur spacings, <x>, from 2.8 Å to 4.2 Å, are in close agreement to those found by Landman and coworkers.[4] Furthermore, the transitional change in ligand spacing between 3.3 to 3.5 nm core diameter is similar to the transitional jumps observed by Murray and coworkers for dodecanethiol coated gold nanoparticles at a core diameter of ~4.4 nm.[1] It is likely that the difference in the core radius at which this jump occurs is due to the differences in ligand lengths as well as measurement errors. We discuss this further in Section 3.4.4. Considering the observed headgroup spacing, we do not expect the observed increase with diameter from the continuous model—indeed, a slight decrease in observed spacing would be expected due to a decrease in free volume with decreasing curvature. Thus, in regards to the continuous model, we find that the close agreement of sulfur spacing with theory is indicative that the model is capturing a large part of the ligand shell behavior, However, it still lacks a key underlying component which would describe the observed headgroup spacing behavior—likely the reality that that the core has a crystallographic shape.

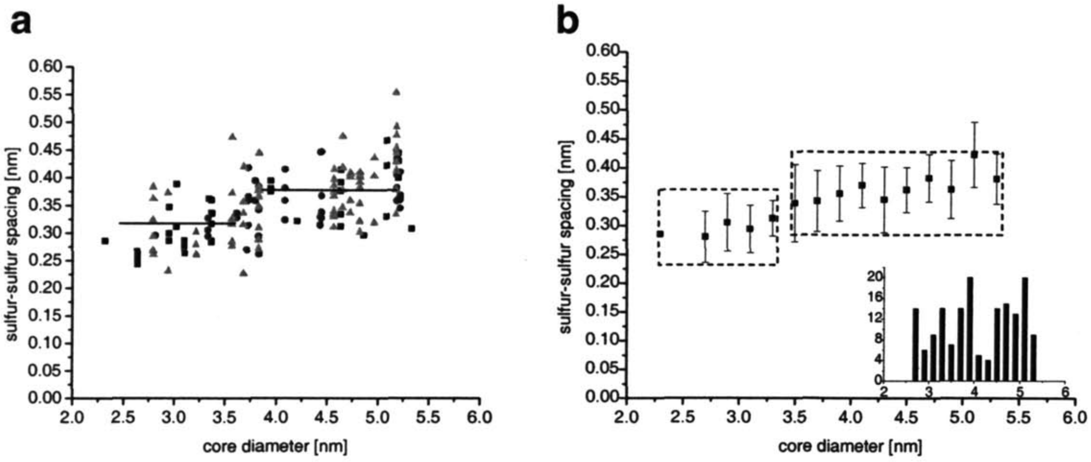

Figure 3.6 (a) Sulfur spacing (calculated using the continuous model) of OT homoligand nanoparticles from three STM scan images as a function of core diameter: red circles, two-phase-synthesized nanoparticles, imaged at 0.868 μm/s; black squares, two-phase-synthesized nanoparticles imaged at 0.695 μm/s; green triangles, one-phase-synthesized nanoparticles imaged at a tip velocity of 0.861 μm/s. (b) Averaged data from (a) showing an increase in neighboring sulfur spacing with core diameter. The dotted rectangular boxes outline two possible flat regions of sulfur spacing in the regions of 2.3–3.3 and 3.5–5.5 nm core diameters. The difference in average spacing values in these two regions is statistically significant with a level of confidence of 99%. Inset: histogram of the number of spacing measurements per nanoparticle core diameter.

3.3.4. Discussion and formation of a homoligand nanoparticle model

Given our observations and the above discussion, we believe that the most probable equilibrium conformation for the ligand shell structure is a combination of the crystallographic model—taking into account the inherent crystallographic, faceted nature of the core and a preferred global tilt anlge of the ligands over each hemisphere—and the continuous model—which brings in the effect of the splay due to the curvature of the core, as shown in Figure 3.3c. In this model, the headgroup spacing should increase slightly with diameter as the ratio between facet area and edge length increases, and should always be larger than that on flat surfaces due to splay. We note that the ratio of facet to edge sites should linearly increase as the diameter increases, but changes in the crystallographic shape of the nanoparticle core will result in discontinuous changes in such a ratio and should be reflected in a discontinuous change in the observed headgroup spacing. Indeed, our data show such a discontinuous jump in sulfur spacing at ~3.3 nm to 5.5 nm core diameter (note that we have observed this discontinuous change for mixed-ligand particles as well (section 3.4.3)). Although our homoligand data have a degree of uncertainty that does not allow for a conclusive picture on the molecular arrangements, the trends observed support this final proposed ligand shell model. For a further discussion of the effect of core shape and size on ligand packing as well as the nature of the transition in ligand spacing at 'critical' core diameters see Section 3.4.4.

3.4. STM observations of mixed-ligand shell morphology

3.4.1. Phase-separated domains in the shell of mixed-ligand nanoparticles

Mixed ligand coated metal nanoparticles, due to the complex convolution of core curvature and inter-ligand interactions, show ligand shell morphologies that are strikingly different than those observed on flat surfaces and homoligand particles. Indeed, we find that for many ligand shell compositions, the molecular mixtures phase-separate into ordered, ribbon-like domains that encircle the core, as shown in Figure 1.[13] Note that on flat surfaces these same mixtures do not form ordered domains, but phase-separate into roughly circular, dispersed domains of the minority component in a matrix of the other (see Figure 3.2 and Chapter 1.2).[12, 14, 15] As a characteristic example of such ordering, Figure 3.1 shows a STM image of gold nanoparticles coated with a 2:1 molar ratio of octanethiol: 3-mercaptopropionic acid (OT/MPA); we observe that molecular domains align into parallel, ribbon-like stripes (also referred to as ripples) that encircle and/or spiral around the nanoparticles with a spacing between like domains of ~1 nm. We assign the OT molecular domains to the bright, raised ripples, and the MPA molecular domains to the dark, low regions located in between those of the OT, based on the analysis of STM images of OT/MPA SAMs on flat surfaces of varying composition (Figure 3.2). Further defining this unique nanostructuring, we have also observed the presence of 'poles' on the rippled nanoparticles surrounded by the rings of molecular domains. These are shown in Figure 3.7 along with a schematic representation of what we believe the poles to be—singularities in the ligand shell where the rings of domains collapse to a single point. These points are essentially non-equilibrium, high energy defects sites in the ligand shell which may or may not be occupied by a ligand. Their significance is discussed in Section 3.7.

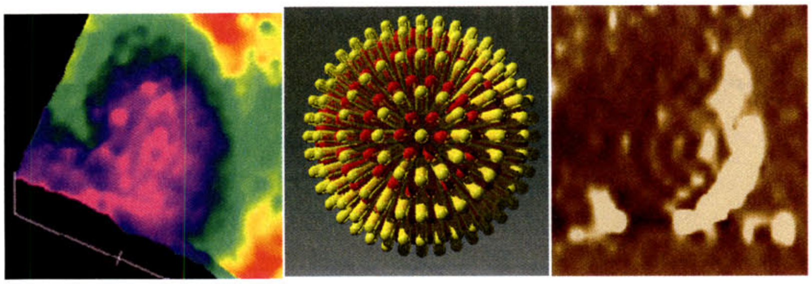

Figure 3.7 Demonstration of the presence of poles on 'rippled' nanoparticles. (a) STM height image of a rippled nanoparticle showing the one of its distal poles surrounded by rings of phase-separated domains. (b) Corresponding schematic image of (a) demonstrating what we believer the poles to be—defect sights where the ligand molecule is not at its optimal tilt angle. (c) An STM current image of a distal pole on a different particle that in (a).

This unique domain formation and morphology is not specific to the OT/MPA mixed ligand system. We have observed the presence of ribbon-like domains for nanoparticles coated with: nonanethiol/mercaptohexanol 2:1, with an average spacing of approximately 0.7 nm; octanethiol/11-mercaptoundecanoic acid (OT/MUA) 1:1, with an average spacing ranging from 0.8 to 0.9 nm; 4-amino-thiophenol/hexanethiol 2:1, with an average ripple spacing ranging from 0.6 to 0.8 nm; and octanethiol/mercaptoanthracene 2:1, with an average ripple spacing of 0.9 nm (Figures 3.8-3.11). We find that the ligand combinations which show the clearest domain formation in STM are either composed of a tall-hydrophobic/short-hydrophilic combination or, if both ligands are hydrophobic, one of the ligands contains a pi-conjugated ring system providing a strong driving force for phase segregation of the components. The wide variety of ligand functionalities for which ordered phase separation occurs indicates that the phenomenon is a general one and not specific to a specific combination of ligand functionalities (for a further discussion of the significance of the generality of domain formation see Section 3.6.1). It is also interesting to note that some ligand combinations such as OT/MPA and octanethiol/mercaptoanthracene 2:1 show significantly more defined domains as compared to other ligand shell morphologies, such as OT/MUA, and there are some combinations for which we have seen no clear domains, such as OT/decanethiol. Whether this is due to variations in domain morphology, ability to form domains as a function of ligand functionalities and/or simply to the ease with which the STM can image the domains needs to be further investigated. We discuss this point briefly and its implications about the thermodynamics of domain formation in more detail in Section 3.6.1

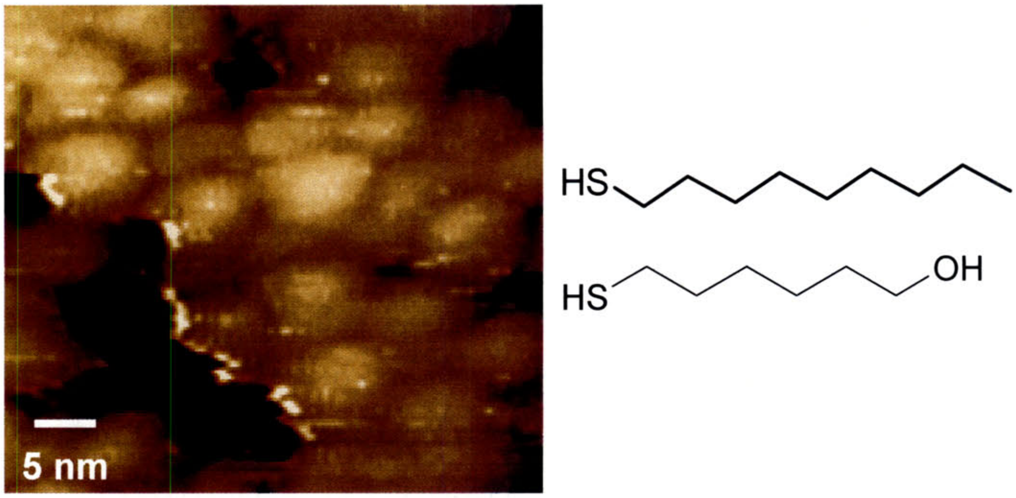

Figure 3.8 STM height image of nonanethiol:mercaptohexanol 2:1 nanoparticle monolayer along with corresponding ligand structures.

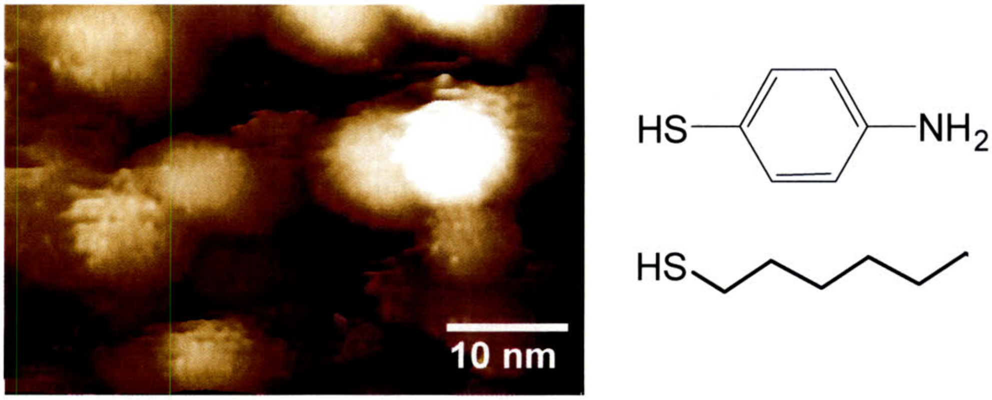

Figure 3.9 STM height image of 4-amino thiophenol/hexanethiol nanoparticle monolayer along with corresponding ligand structures.

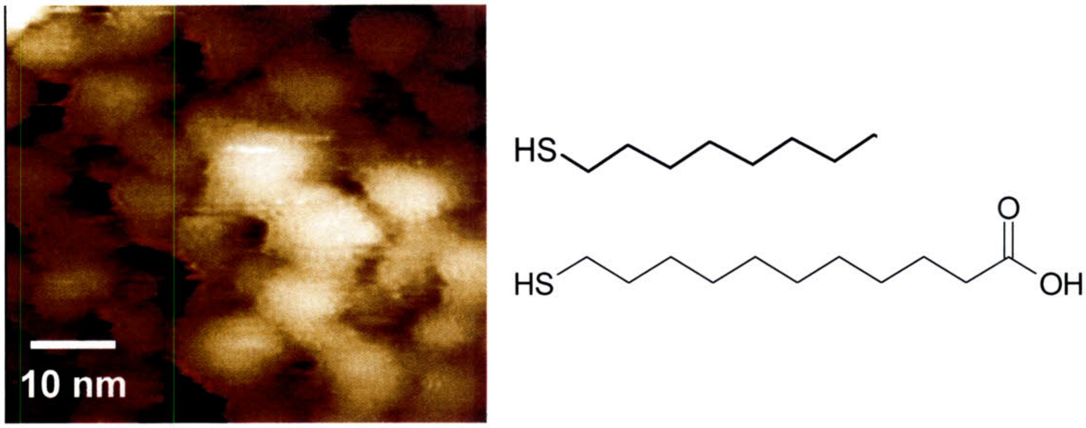

Figure 3.10 STM height image of octanethiol:mercaptoundecanoic acid 1:1 nanoparticle monolayer along with corresponding ligand structures.

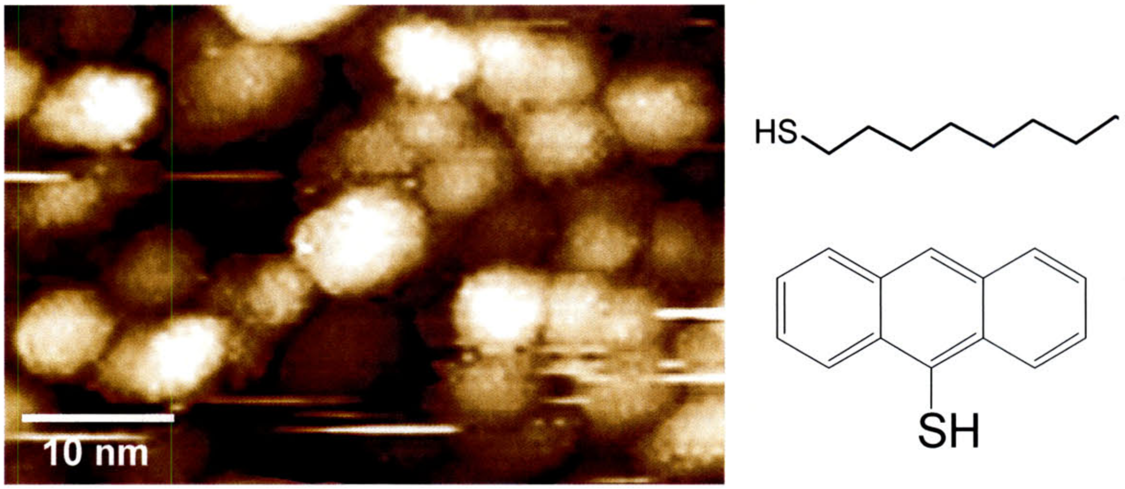

Figure 3.11 STM height image of octanethiol/mercaptoanthracene 2:1 nanoparticle monolayer along with corresponding ligand structures.

3.4.2. Tuning ligand shell morphology: dependence of domain width and morphology on ligand ratio

Ordered phaseseparation is a signature of many systems (e.g. block copolymers,[29] Langmuir-Blodget films, and Pb atoms on Cu[30])[31] and the ability to evolve through various domain morphologies as a function of composition is a common attribute. Thus, in order to understand if the unique phase separation and ligand shell morphology seen on nanoparticles also adheres to this behavior, we studied the effect of varying the relative ratio of the two ligand molecules on the nanoparticle core, specifically OT/MPA coated Au nanoparticles. As shown below in Figures 3.12 and 3.13, the observed domain structure splits into two distinct (as determined within the resolution of STM) morphologies: 1) rippled, stripe-like domains (as presented previously) for those compositions in which the minority component makes up at least 20% of the ligand shell, and 2) discrete domains for compositions in which the minority component makes up less than 20%. The discrete domain morphology was established by observing that for those compositions in which one molecule is present in small amounts (e.g. 30:1 OT/MPA), the headgroup spacing approaches that of homoligand nanoparticles—indicating the dispersal of the lesser component in a matrix of the more abundant one. However, note that the average spacing of this system of ~0.6 Å is greater than that observed for homoligand, indicating that the lesser MPA component is present, and that its presence serves to increase the observed OT headgroup spacing.

As is observed for the OT/MPA system, the stripe-like domain morphology is preferred over most of the composition range, with changes in ligand ratio leading to changes in domain-width. Indeed, one can observe that the changes in domain width occur in discrete steps of ~3 Å. For example, while 5:1 and 3:1 OT/MPA ratios have a domain spacing of ~0.6-0.7 nm (as is also seen for 1:2 and 1:3 ratios), OT/MPA 1:1 and 2:1 ratios have a larger spacing of ~0.9-1 nm. This suggests that changing composition while in the ripple regime of domain morphology, changes the width of the domains by 1 to 2 molecules. Furthermore, the observation that domain spacing is relatively constant across small changes of composition further suggests that there are *preferred* domain widths. Thus, varying the ligand ratio does have an effect on the domain morphology in terms of varying the domain spacing or in the formation of ripples. However, within the resolution limits of STM, only two domain morphologies are observed.

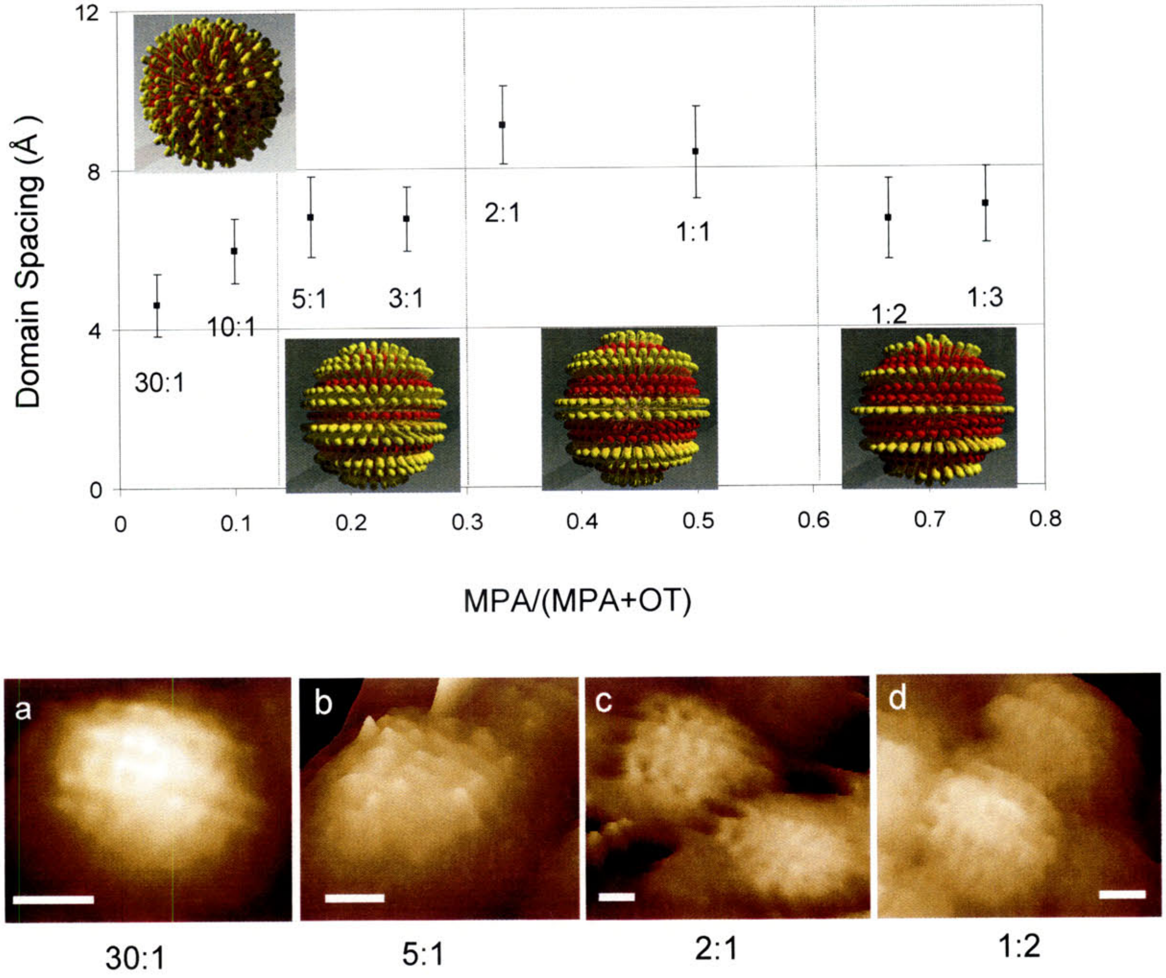

Figure 3.12 Plot of the domain spacing as a function of MPA percentage used in the synthesis of OT/MPA mixed ligand gold nanoparticles. All nanoparticles had an average diameter of ~ 3.7 nm. Variation of domain structure (e.g. ripples vs. discrete domains) as well as domain spacing with ligand composition points to a molecularly driven mechanism for the size control of the ripples and not to a metal directed one. The schematic drawings of the particles are meant to help visualize a possible molecular origin of the discreteness and the trend in the spacing of the domains.

(Below) STM height images of various ratios of OT/MPA mixed ligand nanoparticles showing the evolution of domain morphology from discrete domains to well-defined ripples. All scale bars 2 nm. Note that nanoparticles containing >50% of MPA in their ligand shell were significantly more difficult to image (e.g. ripples were not as clearly defined as in 2:1 OT/MPA coated nanoparticles); we believe that this is likely due to increased water adsorption.

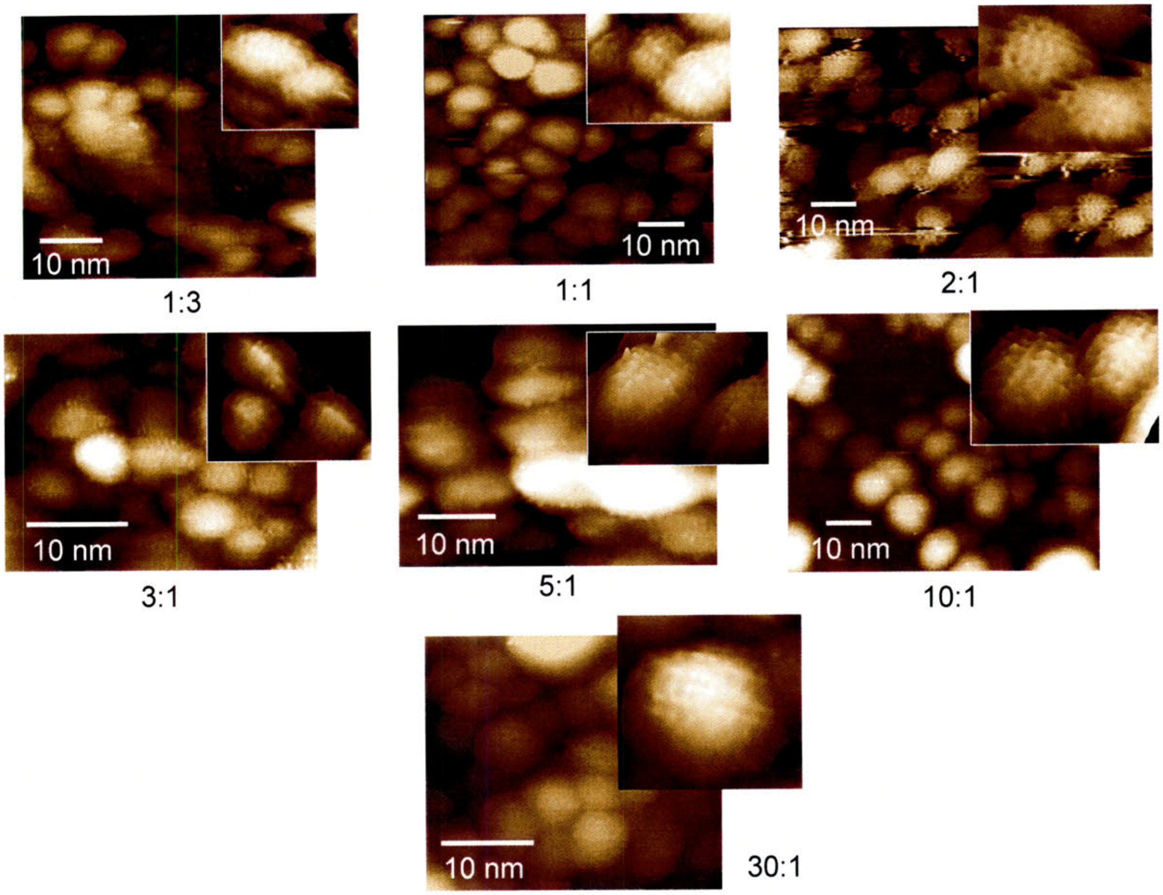

Figure 3.13 Demonstration of nanoparticle ligand shell morphology as a function of OT/MPA ligand ratio. Note that while ripples are seen for OT/MPA 1:3, 1:1, 2:1, 3:1, and possibly 5:1, for the ratios of 10:1 and 30:1 discrete domains are seen. Indeed, the headgroup spacing for 30:1 agrees with that of OT homoligand particles indicating a likely identical ligand conformation.

3.4.3. STM investigation of the dependence of domain spacing on core diameter

The clear curvature dependence of ligand spacing observed for homoligand nanoparticles, together with the ability to modulate ripple spacing on mixed-ligand particles through variation of shell composition, suggests that domain morphology can also be modulated through the core curvature. Thus, we investigated the effect the core curvature (through changes in diameter) on ligand shell morphology and domain spacing. Using OT/MPA rippled particles of fixed compositions as model systems (so chosen due to their high contrast and large spacing between domains, as compared to other ligand systems) we studied domain spacing as a function of core diameter. Both OT/MPA 2:1 and 1:1 compositions were studied, as well as a non-rippled composition, OT/MPA 30:1, for comparison, and we initially present each composition study separately.

3.4.3.1 OT/MPA 2:1 results

Two separate syntheses of OT/MPA 2:1 particles were performed using the 2-Phase method; we denote the resulting particles from each as **np1** and **np2**. The two syntheses resulted in particles of different size polydispersity with **np1** ranging from 2 to 6 nm core diameters, and **np2** ranging from 3 to 8 nm. It was observed that within the diameter ranges studied, only the rippled domain morphology was present. To investigate the effect of curvature on the domains, we plot the average STM observed domain spacing as a function of core diameter (determined assuming that the longer OT molecules in the ligand shell determines the STM observed diameter) for each nanoparticle type (**np1**, **np2**) as shown in Figure 3.14. For both sets of particles we plot both data taken from one single STM scan image (Figures 3.14a and 3.14c), as well as the composite data from all of the scan images for each nanoparticle batch (3.14b and 3.14d). We provide both plots due to the fact that, as can be observed, while the trends that are clearly apparent in the single scan plots are also evident in the composite plots, their effect is muted. This is likely due to a confluence of effects that occur when data from separate scans are merged; these include: variations in image quality between scans, variations in tip/sample convolution effects at different scan speeds, increased number of outliers in the combined images, and to the increased variation of spacing values for nanoparticles whose size lies within the transition region (see discussion below). Thus, trends in the spacing data can often be recognized more easily from single scan images (provided a large range of particle diameter and spacing values are provided in the single image); however, composite data must be examined in order to verify spacing values and behavior.

Examining the headgroup spacing data for **np1**, it is immediately apparent, particularly in the individual scan plot, that there is a complex, 'saw-tooth' like dependence of the domain spacing on the diameter, with ripple spacing decreasing from 1.15 to 0.90 nm in the diameter ranges of 3.1-4.1 nm and 4.5-5.5 nm, separated by an abrupt and transitional jump in spacing in the diameter region of 4.1-4.5 nm. The composite plot echoes these same trends and shows a total average domain spacing of 1.04 nm with a slight overall increase in spacing with diameter from 1.00 nm at 1.7 nm core diameter to 1.07 nm at 5.9 nm. Applying the continuous model to the data results in a step-like behavior in the sulfur spacing with constant values of 0.64 nm and 0.74 nm, for the composite data. Note that these constant spacing regions occur in the same regions that we observe decreases in ripple spacing.

Examining the data for **np2** (Figure 3.14 c and d) similar trends and values are observed. Again a similar pattern of spacing vs. diameter emerges with regions of decreasing headgroup spacing (from approximately 3.3-4.5 nm, 5.3-6.5 nm, and possibly in a region starting at 7.1 nm core diameters) and corresponding regions of constant sulfur spacing separated by discontinuous jumps. Average spacing measurements for each scan image typically ranged from 0.85-1.10 nm, with the average ripple spacing across all images being 0.98 nm. Again, a slight overall increase in spacing with diameter from 0.86 nm at 2.3 nm to 1.06 nm at 6.6 nm is observed.

The observed differences between **np1** and **np2** in regards to the exact diameters at which decreasing regions of and transitions in spacing occur are likely due to several factors, including: slight variances in the syntheses (reactant amounts, time of addition, etc.) which could have effects on the final structure, and that **np2** samples were imaged far earlier in time than **np1**; over this time period the STM operator's skill improved greatly, resulting in improved resolution and reduced noise for scan images of **np1**.

Combining the data from **np1** and **np2** to produce a composite plot of all OT/MPA 2:1 particles (Figure 3.14e), we find that the spacing data still shows a saw-tooth behavior, but damped. Regions of decreasing ripple spacing and constant sulfur spacing occur from roughly 2.9-4.5 nm, 5.3-6.7 nm, and a possible region starting at 7.1 nm core diameters, and are separated by discrete transitional increases in spacing. The overall, average headgroup spacing is 1.04 nm, with an increase from 1.00 nm at 1.7 nm core diameter to 1.05 nm at 7.5 nm.

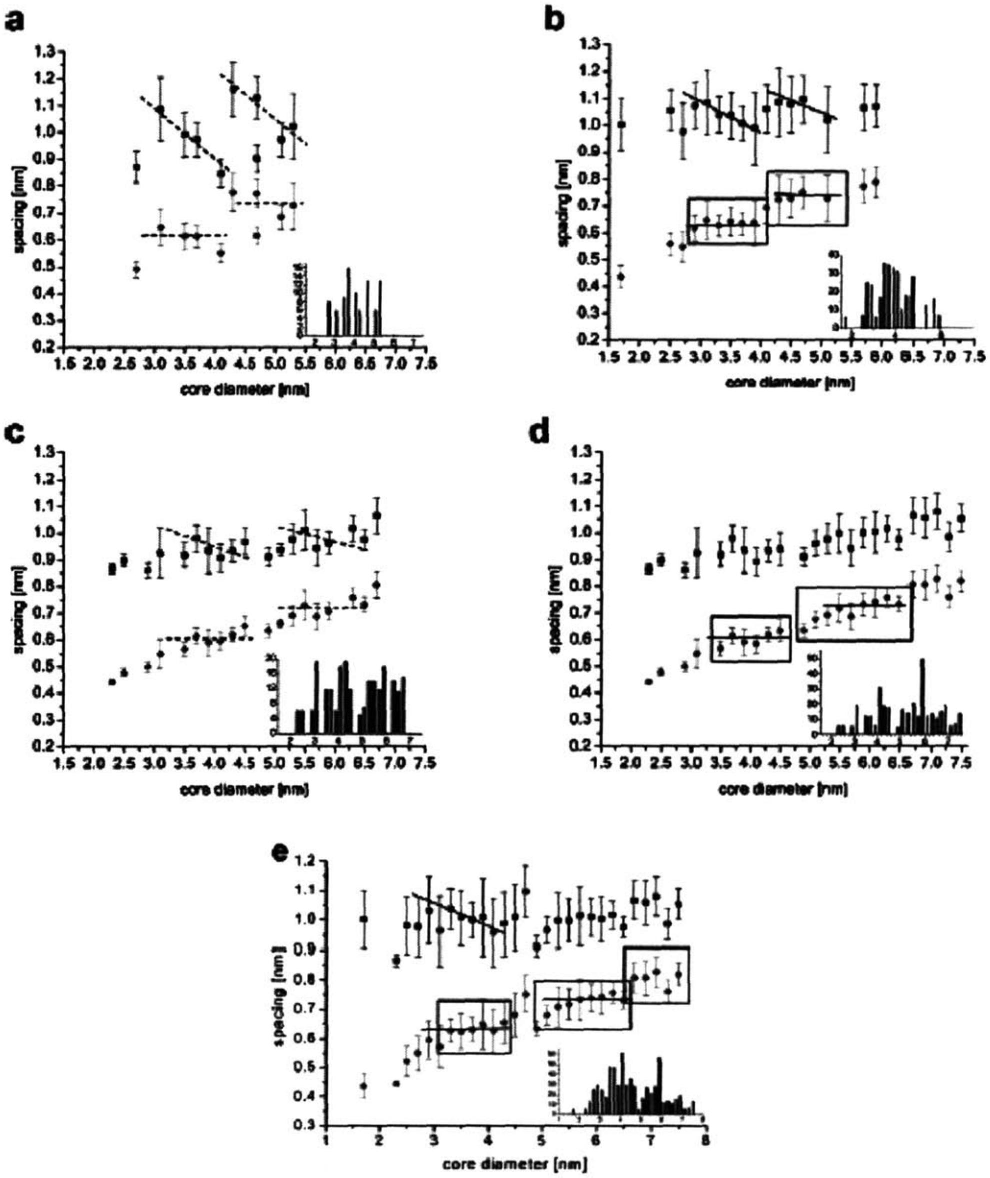

Figure 3.14 STM-observed headgroup spacing (black squares) and corresponding sulfur spacing (determined using the continuous representation) (red circles) of OT/MPA (2:1) nanoparticles as a function of nanoparticle core diameter with an average of more than 5 spacing measurements taken per particle: (a) **np1** data from one individual scan image and (b) a composite plot containing data from all individual scan images of **np1**; (c) **np2** data from one individual scan image and (b) a composite plot containing data from all individual scan images of **np2**; (e) combined data from **np1** and **np2**. The plots from single measurements show decreases in ripple spacing from roughly 2.9 to 4.5 nm and from roughly 5.3 to 6.7 nm, separated by discrete transitional increases in spacing. The trends in the plots from single images are clear, and dotted lines have been superimposed to help guide the eye; they have not been calculated and should be considered as arbitrary. In the case of the statistically more relevant combined plots (b, d, e), the trend lines shown are supported by a statistical analysis. The differences in the average sulfur spacing values in the regions identified with boxes are significant with a level of confidence of 99% or more. The regression and the slopes of the trend lines in the headgroup spacing plots are significant with a level of confidence of 95% or more. Insets: histograms of the number of spacing measurements per nanoparticle diameter.

3.4.3.2 OT/MPA 1:1 results

In order to determine if the trends in domain spacing observed for OT/MPA 2:1 nanoparticles held for other compositions of rippled particles, we examined the domain spacing dependence of OT/MPA 1:1 nanoparticles as a function of core diameter. The particles were synthesized using the 2-phase synthesis, and ranged in core diameter from 1.5-6 nm. As shown in Figure 3.15, we plot both data from a single scan image as well as composite data from multiple scans. Both plots show a range of average spacings ranging from 0.6-0.7 nm with a dependence of spacing on core size; slight decreases in ripple spacing occur from approximately 2.1-3.1 nm and 3.5-4.9 nm core diameters separated by a transitional jump in spacing between the two at 3.1-3.5 nm diameter. Correspondingly, sulfur spacing, as calculated by the continuous model, exhibits a step-like behavior in both plots, demonstrating two constant spacing values of ~0.35 nm and ~0.45 nm. As can be observed in the composite plot, there is an overall increase in ripple spacing from 0.58 nm at 1.5 nm core diameter to 0.75 nm at 5.7 nm, and an overall average spacing of 0.69 nm.

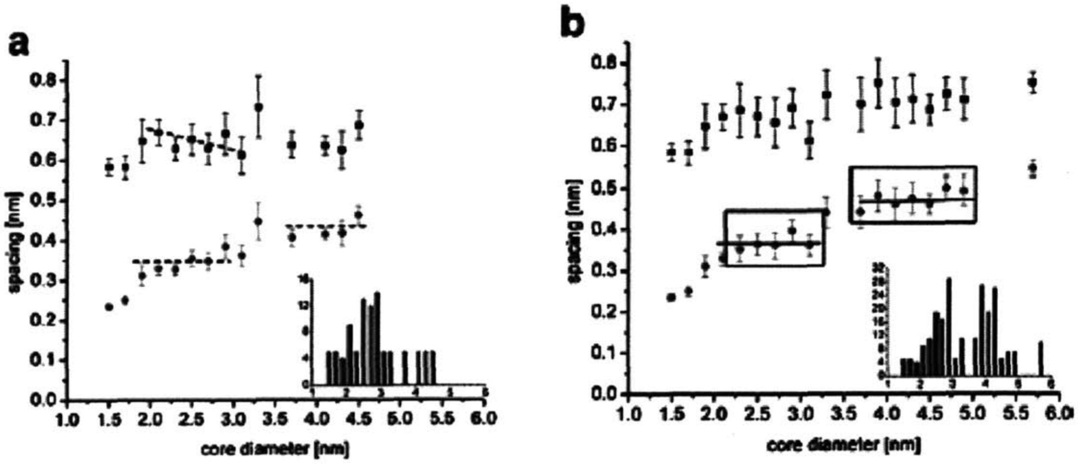

Figure 3.15 STM-observed headgroup spacing and corresponding sulfur spacing of OT/MPA (1:1) nanoparticles as a function of nanoparticle core diameter. (a) Data from one individual scan image. (b) Combined data from all individual scan images. Insets: histograms of the number of spacing measurements per nanoparticle diameter. The plot from a single scan image, (a), shows decreases in ripple spacing in the ranges of 2.1–3.1 and 3.3–4.9 nm core diameters separated by a transitional jump in spacing in the region of 3.1–3.3 nm core diameter. The trends in (a) have been superimposed to help guide the eye; they have been not calculated and should be considered as arbitrary. In the case of the combined plot (b), the differences in the average sulfur spacing values in the regions identified with boxes are significant with a level of confidence of 99%.

3.4.3.3 OT/MPA 30:1 results

We also investigated the effect of core diameter on mixed-ligand, but non-rippled nanoparticles in which one component is present in far greater excess that the other (e.g. OT/MPA 30:1) and so show only a 'patchy,' nearly homoligand, spacing behavior. The particles were synthesized using the 2-phase synthesis and ranged in core diameter from ~1-6 nm. As is shown in Figure 3.16b, the average STM observed headgroup (note we do not use the term 'domains' here as no grouping and formation of either island-like or ripple domains were observed) spacing is ~0.6 nm and increase with core diameter from 0.54 nm at 1.1 nm diameter to 0.66 nm at 5.1 nm diameter. As can be observed from both the individual (Figure 3.16a) and composite (Figure 3.16b) plots, the headgroup spacing demonstrated the characteristic 'saw-tooth' behavior that has been observed for both the OT/MPA 2:1 and 1:1 compositions, as well as the step-like behavior in sulfur spacing (as determined by the continuous mode). Two regions of approximately constant sulfur spacing occur from approximately 1.7-2.8 nm and 3.5-5.0 nm core diameters with an average sulfur spacing of 0.3 nm, and 0.4 nm, respectively, separated by a discontinuous jump in spacing.

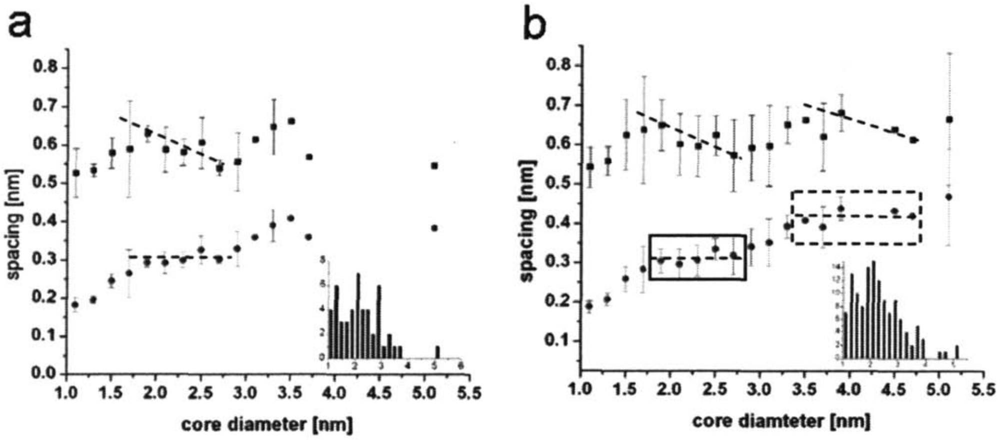

Figure 3.16 STM-observed headgroup spacing and corresponding sulfur spacing of OT/MPA 30:1 nanoparticles as a function of core diameter. (a) Data from one individual scan image. (b) Combined plot of data from all individual scan images. Insets: histograms of the number of nanoparticles measured per nanoparticle diameter; note that ~3-4 spacing measurements were taken per particle. The plot from a single measurement (a) shows decreases in ripple spacing in the ranges of 1.7–2.8 and 3.5–5.0 nm core diameters separated by a transitional jump in spacing in the region of 2.8–5.0 nm core diameter. The trends in (a) and (b) have been superimposed to help guide the eye; they have been not calculated and should be considered as arbitrary.

3.4.4. Discussion of the dependence of domain spacing on core diameter

Comparing the domain spacing behavior of the mixed ligand particles, we find that within the diameters studied, the overall change in domain spacing for each particle type is slight, with no plot overlapping another, indicating that total ligand composition on the particles does not change significantly with diameter. All of the plots show a similar complex dependence of the domain spacing on core diameter, each exhibiting the 'saw-tooth' behavior of regions of decreasing spacing separated by transitional jumps in spacing. It is interesting to note, as is particularly evident for OT/MPA 2:1, that the standard deviation of the average spacing measurements is greater in transitional regions than elsewhere in the plot. This suggests that these regions are indeed 'transitional' with particles near these diameters exhibiting widely different domain spacings. We also note that the plots show an overall average increase in domain spacing with diameter—as was also observed for homoligand particles due to the changing facet/edge ratios of the core. The complex and similar spacing behavior displayed by all of the particles, indicates that the core curvature is having a dominant effect on the ligand organization and domain behavior that is general across and independent of composition.

In order to develop a deeper understanding of the spacing behavior it helps to consider how the values and trend observed for headgroup spacing translate to the corresponding sulfur atoms on the gold surface. Applying the continuous model to the data for all of the particles, as shown in Figures 3.14-3.16, we see that the regions of decreasing domain spacing transform to regions of constant spacing separated by transitional jumps—similar to those observed for OT homoligand nanoparticles. The emergence of regions of constant sulfur spacing once again suggests that the continuous model and its implications hold in these diameter ranges. Discontinuous, transitional changes in monolayer packing behavior have also been observed by Murray and coworkers. The researchers studied dodecanethiol coated gold nanoparticles ranging in diameter from 1.5 to 5.2 nm,[1] and found, using TGA and FTIR, that the ligand shell monolayer underwent a transition in packing at a 'critical' core diameter of ~4.4 nm, with larger particles exhibiting a more ordered, 2-D-like monolayer structure.

The most striking feature when we compare the domain spacing data between all of the compositions of particles is not the 'saw-tooth' trends seen in both, but the occurrence of almost identical behavior at approximately the same diameters. Indeed, if we also include in this comparison the OT homoligand data (see Figure 3.17), we find that, particularly when examining the sulfur spacing data, the critical diameters at which trends occur, overlap. As shown, all particles have regions of decreasing spacing separated by transitional jumps in the regions around 3.1 nm and 5.1 nm. The universality of the step-wise changes in spacing, independent of the presence of domains, suggests an underlying effect of the nanoparticle core. Indeed, in examining the behavior of the ligand shell of homoligand particles using the continuous model, we suggested that the changing facet to edge site ratio with diameter could play a role in the transitions seen. It has been shown in the literature that the preferred crystallographic shape of nanoparticles is a function of particle size. For nanoparticle diameters below 2-3 nm, the predominant crystallographic core shape is icosahedral, transitioning to a predominance of the truncated dodecahedral structure from 3-4 nm, and then to the truncated octahedral shape above 4-5 nm.[21, 32] While within a set crystallographic shape, size changes lead to an edge to facet site ratio that changes linearly, but as one preferred crystallographic shape transitions to another, there is a discontinuous change in the facet to edge ratio. Considering the above information, we propose that it is these discontinuous changes in crystallographic shape which lead to the discontinuous changes in ligand spacing. Furthermore, we propose that the linear decreases in headgroup spacing, which are so clearly evident for the rippled particles, are likely due to the effect of splay—increasing diameter leads to a loss of free volume for the headgroups, resulting in a smaller observed domain spacing. The same effect is present for homoligand particles, but due to the fact that headgroup, as opposed to domain, spacing is measured, the effect is muted and difficult to distinguish. Indeed, domains, due to their collective headgroup behavior, serve to amplify the effect of core changes in the ligand shell. This explanation further serves to explain the weakened (as compared to OT/MPA 2:1) saw-tooth behavior for OT/MPA 1:1 particles due to the decreased width of the ripples which also have the effect of making imaging and subsequent spacing analysis more difficult. Lastly, the overall increase in headgroup/domain spacing with diameter seen for all particle compositions, we ascribe to decreases in the fraction of edge atoms on the core surface and to the consequent decrease of crowded ligands on edge atoms, leading to an overall increase in headgroup spacing. Thus, we find that our proposed ligand shell model, which takes into account both the inherent curvature and hence splay of the ligand shell from the continuous model as well as the changing crystallographic nature of the core and preferred tilt angles of the ligands from the crystallographic model, describes the behavior of both homoligand and mixed-ligand particle systems.

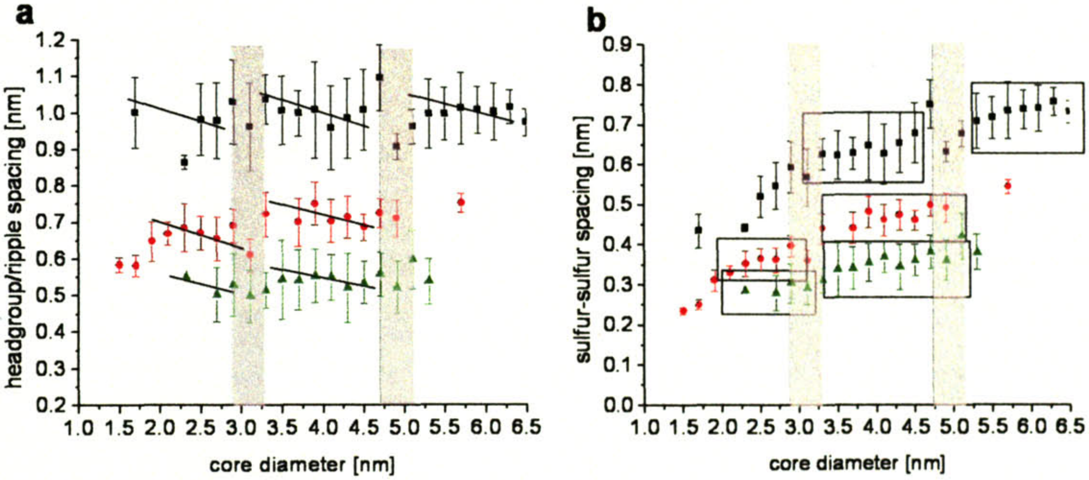

Figure 3.17 (a) Headgroup spacing as a function of core diameter for all nanoparticle compositions: OT homoligand particles (green triangles), OT/MPA 1:1 (red squares), and OT/MPA 2:1 (black boxes). Gray areas indicate regions of transitional changes in spacing. (b) Sulfur spacing as a function of core diameter for all nanoparticle compositions. Boxes outline regions of constant spacing for each nanoparticle composition. Gray areas are the same as those for (a). Note that 30:1 OT/MPA particles exhibit the same trends as the other OT/MPA compositions presented but are not included in the plots as it overlaps with homoligand data.

3.4.5. Discussion of sulfur spacing values at very small core diameters

Comparing the sulfur spacing values at very small core diameters (< 2 nm) across all of the particles, we see that there appears to be a transition region for all of the particles at ~2 nm, and below this value, the sulfur spacings approach very small values. We see that for OT/MPA 2:1 particles that the sulfur spacing is ~4 Å, and for OT/MPA 1:1 and 30:1 compositions, we find that the spacing values decrease roughly linearly to 0.3-0.2 nm—values close to those seen for homoligand particles. We note that for such a small sulfur spacing to be attained, particularly 0.2 nm, the sulfurs would need to form disulfides—a possibility which has been proposed in the literature. Guttierez-Wing and coworkers found, using computational simulations, some presence of sulfur pairing on thiol coated gold particles with a size of ~5 nm.[5] Additionally, the formation of disulfides in SAMs on flat surfaces has been experimentally observed using various methods. Fenter, using grazing incidence x-ray, reported a sulfur-sulfur distance of 2.2 Å for decanethiol SAMs,[33] implying the existence of a sulfur-sulfur bond which was further supported through X-ray standing wave[34] and high-resolution electron energy loss spectroscopy experiments[35]—albeit these are highly contested results. It has been suggested that the observed disulfide formation is a result of the measurement technique of X-ray, which results in an excited state of the thiol molecules, causing them to move from their Au-S ground state form to the higher energy disulfide state.[36] However, recent STM studies have also suggested the formation of disulfides for some monolayers.[37, 38] Müller-Meskamp observed sulfur-pairing for dodecanethiol SAMs, which they ascribed to be an intermediate phase close to desorption—pointing again to the influence of the molecules' energy state on packing.[39] Adding to this debate, a recent large scale simulation study of alkanethiol monolayers finds that thiolates are thermodynamically favored relative to sulfur-paired chains, but that disulfides may exist in some cases.[38] Thus, one might argue that the high energy surface of the particle (with increasingly higher energy surfaces for decreasing core size) provides such a 'high-energy' state for disulfide formation.

Furthermore, we note that the observed headgroup spacings, particularly on OT/MPA 1:1 and 30:1 particles, approach that of homoligand particles, raising the question as to whether these particles continue to be rippled and/or mixed ligand at such small diameters. There are some reports in the literature that mixed ligand particle compositions vary with core size at very small diameters.[22, 40] There is some question as to whether such small particles can support ripples, especially as the ripple width becomes equivalent to particle size. Lastly, we must also consider the possibility that the continuous model used to determine the sulfur spacing does not hold at these particle diameters. In this size regime, there may be too few ligands to constitute a 'true' monolayer, the nanoparticle may possibly be no longer viewed by the ligands as a sphere, and the ligands may have so much conformational freedom that they are highly disordered. Any of these factors could lead to a breakdown in the continuous model. Further studies should be pursued, and are currently underway, in order to clarify the ligand shell behavior at small core diameters.

3.5. Ultra high vacuum, low temperature STM investigation of nanoparticles

Ultra High Vacuum, Low Temperature (UHV, LT) STM imaging allows for the capability to examine nanoparticles in an impurity free environment at a variety of controlled temperatures. At room temperature, despite the high packing density of ligands around the nanoparticle core, it has been predicted that the ligand chains within the particles' shell are conformationally mobile.[41] This is expected to have a negative effect on the resolution achievable with STM when imaging and characterizing ligand arrangements.[4] However, below the ligand shell melting temperature (T_m),[2, 4] it has been predicted that ligands attain a highly crystalline order allowing for better imaging resolution and more accurate characterization of the ordering and packing arrangements of the ligand shell. Thus we sought to examine whether imaging nanoparticles at low temperature could improve the molecular resolution of the ligand shell. We also sought to confirm our previous results on the ligand ordering and spacing using a different STM.

3.5.1. Results

Prior to imaging, samples were heated under vacuum to ~338 K for ~20 min after which they were cooled to and held at 318 K overnight. This allowed for the release of impurities from the ligand shells of the particles and for better interdigitation, and hence stabilization, of the particles during imaging. Figure 3.18 displays a large scale STM height image showing nonanethiol/mercaptohexanol 2:1 nanoparticles ~4-6 nm in diameter with nanostructuring evident in many of the particles' ligand shells. A close-up image of the nanoparticles (Figure 3.18a) shows two groupings of nanoparticles with a few particles showing highly defined ribbon-like domains (or ripples) of ~0.7-0.8 nm in spacing. Images were obtained at various scan angles ranging from 0-90° with nanostructuring evident on at least some, but often not the same, particles with each scan rotation.

3.5.2. Discussion

The ripple structure and spacing observed using the DI microscope in ambient conditions (Section 3.4.1, Figure 3.8) and the Omicron microscope in UHV at low temperature are essentially identical, ~0.7-0.8 nm. This agreement in spacing across the temperature range probed suggests that for some compositions of rippled nanoparticles (e.g. those in which the absolute lengths and relative length difference of the ligands are not very large), that the ligand chains are highly ordered and not highly conformationally mobile at room temperature—that is, the ripples 'lock-in' and provide ordering within the structure of the ligands, essentially raising the T_m of the ligand shell. More experiments need to be done to confirm this assumption, specifically examining homoligand nanoparticles, as these results suggest that ligands are less labile on rippled particles as compared to non-rippled or homoligand particles.

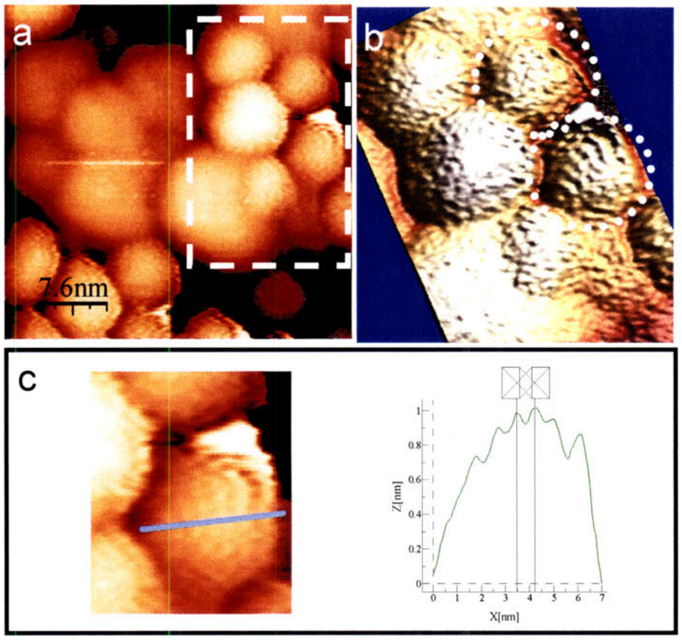

Figure 3.18 (a) STM height image of nanoparticles on Au on mica, coated with a 2:1 molar ratio of nonanethiol and mercaptohexanol. Ripples are visible on the particles in the upper right and lower left of the image. We assign the raised, bright ripples to nonanethiol, and the darker regions in between to mercaptohexanol based upon previous monolayer experiments. (b) 3-D rendering of nanoparticles from (a) indicated by the dotted box. Highly defined ripples can be seen on two of the nanoparticles, indicated by the dotted circles. (c) Line section through one rippled nanoparticle, showing a peak to peak spacing between ripples of 0.74 nm.

3.6. Probing the thermodynamics of ordered phase separation

The formation and evolution of phase separated domain patterns is a well-known and general phenomenon[31] occurring in a variety of systems from the behavior of Pb atoms on Cu surfaces[30] to block-copolymers[42]. Such phase separation and the resulting domain morphology occurs due to competing energies, system constraints, and the degree of mobility within a system to form such domains.[30, 43] However, for mixtures of ligands on flat surfaces, while many ligand combinations lead to phase separation,[12, 14, 15, 44] ordered domains have not been observed—making the observation of such ordered domains on nanoparticles even more intriguing. Phase-separation at this molecular length scale or possessing the degree of order seen on nanoparticles had actually never been observed in SAMs—the smallest domains to date being ~5 nm in width observed in STM by Stranick for two component monolayers on Au(111).[12] It is postulated that the formation of domains on flat surfaces results from the system evolving from an initial, highly mixed, high energy configuration (due to the large number of interface interactions) toward a lower energy configuration by reducing the interface length and hence energy through the growth of increasingly larger domains.[12] It is expected that the same reasoning would apply to monolayers on nanoparticles. However, considering only a reduction in interfacial energy for phase separation on nanoparticles would lead to the conclusion that particles should either be bi-phasic, that is each hemisphere of the particle is coated with only one type of ligand, or constitute two populations of particles with each population coated with only one type of ligand. The fact that we have instead observed highly ordered, phase-separated domains on mixed ligand nanoparticles, prompted us to investigate the ordering mechanism—specifically we wished to evaluate the roles of core material and crystalline structure, ligand functionalities, as well as overall curvature in determining domain structure.

3.6.1. Effect of ligand functionality

As presented above in Section 3.4.1, to date we have clearly observed ripple formation using several two-component mixtures of ligands, varying their relative ligand lengths and functionalities on gold nanoparticles ranging from 2.5 to 6 nm in core diameter, as shown in Figures 3.8-3.11. In all cases the chosen ligands contained a thiol end-group to ensure significant mobility across the gold core and ability to undergo place exchange. Additionally, the fact that in all cases the phase separation manifests itself as 'ripples' indicates a fundamental underlying, optimal domain morphology for alkyl ligands, independent of headgroup functionality. However, as was noted, some ligand combinations were significantly more challenging to image, such as OT/MUA, and we did not observe clear phase separation in the case of others such as OT/DT. This lack of clear observation of ripples may be due to poor imaging resolution due to similar ligand lengths and/or adsorption of water from the atmosphere (in the case of OT/MUA) or to the absence of phase separation in the ligand shell resulting from similar ligand lengths and/or functionalities. It has been suggested by Glotzer (personal communication) that, based upon molecular dynamics simulations of two-component mixtures of ligand on nanoparticle, the height difference between the ligands plays a critical role in determining the domain morphology. Her simulations suggest that it is energetically favorable for ligands to form molecular scale 'stripe-like' domains in order for the end groups of the longer ligand to gain conformational entropy, with the width of the domains varying as a function of chain length difference (see Figure 3.19). Thus, the primary driving force for such ordered, stripe-like domains formation is an entropic gain by the system in forming stripes. This would support the lack of clear STM evidence of domain formation for ligands of similar length on nanoparticles.

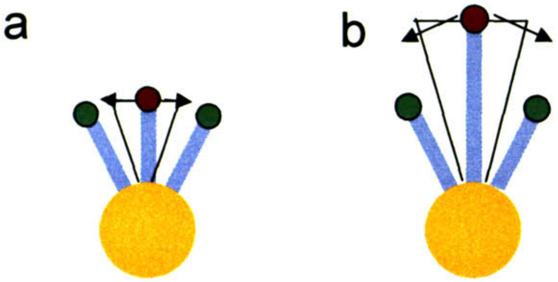

Figure 3.19 Schematic illustration of the degree of conformational freedom available to ligands as a function of substrate curvature and neighboring ligands. (a) On a nanoparticle sphere, ligands of the same height have some degree of conformational freedom (represented by the magnitude of the arrows) due to their splay. (b) However, a longer ligand can gain freedom by surrounding itself with ligands of shorter length. Note that this results in a loss of enthalpic interactions that could be gained by packing with other long chain ligands, as well as the formation of domain wall creating line tension. For both (a) and (b) the degree of conformational freedom available to the shorter ligand does not change significantly whether they are surrounded by ligands of the same height or those that are longer.

3.6.2. Formation of mixed ligands nanoparticles with other core materials

To understand how the material nature of the metallic core influences the formation of the ripples, we synthesized silver nanoparticles with a 2:1 OT/MPA molar composition. The choice of silver was driven by the very similar chemistry between silver and gold; thiols are mobile on both metals, and the synthetic procedures to obtain silver and gold particles are very similar. Preliminary results indicate that ripples form with similar spacing as those on gold, suggesting that the ripple formation mechanism is not solely determined by the core metal. Additionally, indirect evidence by DeVries (personal communications) who has utilized the unique ripple morphology to create particle chains,[45] has shown that these particle form chains, thus supporting the conclusions these particles show ordered domains. Furthermore, initial experiments on mixed monolayers on other core metals (Fe_2O_3, CdSe) suggested that ripples form on these particles as well. However, because the syntheses of these particles are not yet perfected, often there are contaminates in the ligand shell which complicate ligand shell imaging. Further studies are necessary to confirm these results. The above observations suggest that the formation of ordered domains is at most weakly dependent on, and is not precluded by the crystallographic nature of the underlying core

3.6.3. Effect of curvature

To study the effect of substrate curvature on the formation of ordered domains, we analyzed mixed OT/MPA SAMs on Au surfaces of varying curvatures. To produce a broader size and curvature range than that allowed by the synthetic and solubility constraints of larger nanoparticles, we used surfaces ranging from flat Au(111) on mica to highly curved, nanoparticle-like Au surfaces (Figure 3.20). On Au(111) on mica as well as Au thermally evaporated on Si, whose surface is fairly rough with numerous terraces and 10-20 nm diameter hemispheres ~5 nm in height, only roughly circular and randomly distribute domains were observed. To better approximate the curvature present on nanoparticle surfaces, sparse, bare nanoparticle monolayers were prepared on Au on mica substrates. Two variations of substrates were produced: a gold film containing gold crystals of ~10 nm diameter and a gold film with 4-5 nm spherical gold particles. Both substrates were exposed to a mixed ligand OT/MPA solution, forming a SAM over the surface. Using STM, it was observed that both substrates exhibited the ordered, stripe-like domain morphology on the nanocrystals with a domain spacing of ~1 nm—the same as that observed for OT/MPA 2:1 gold nanoparticles. It should be noted that no ordered domain formation was seen on the flat regions of the substrate. This suggests that the dominant driving force for *ordered* domain formation is the curvature of the substrate. Further studies need to be done in order to understand if curvature determines this phenomenon because of geometrical conditions[46], anisotropic surface stress,[47] or yet to be understood mechanisms.

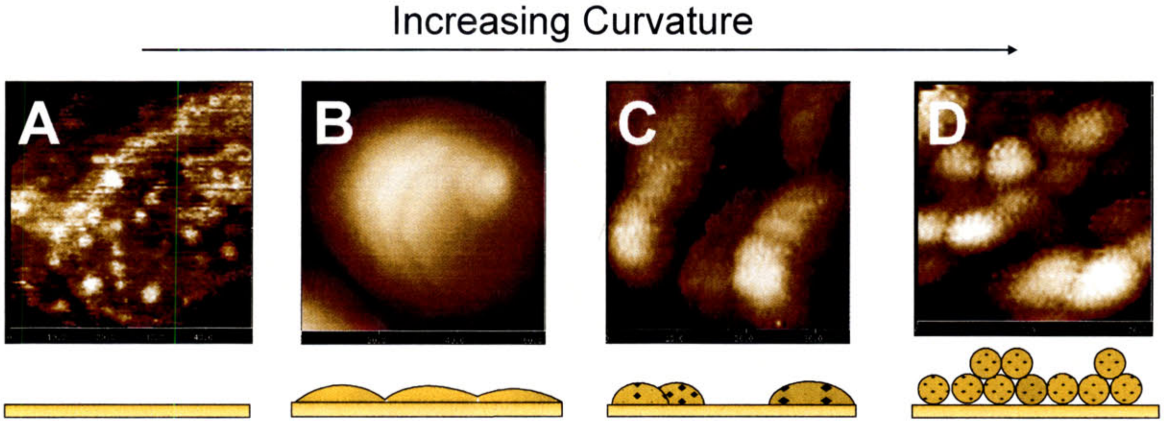

Figure 3.20 STM images of mixed OT/MPA monolayers formed on surfaces of varying roughnesses. (Bottom) Schematic drawings of gold surface roughness and (top) STM height images of mixed monolayers formed on (a), a flat Au(111) on mica substrate, (b), a gold film deposited on a silicon wafer showing hemispheres of ~20 nm diameter, (c), a gold film containing gold crystals of ~10 nm diameter and (d), a gold film with 5 nm gold crystals on it. Ordered, rippled domains are observed only in (c), and (d), while in (a) and (b), randomly dispersed domains are observed. All the monolayers were obtained from a 1 mM ethanol solution of OT/MPA (1:4). It should be noted that on the flat regions of the sample d, the ligands phase-separated in a random way, resembling the behavior shown in a. The fact that no noticeable difference was observed between surfaces generated in different methods seems to rule out a strong effect of the specific crystallographic nature of the metal surface.

3.7. Theoretical basis of ordered phase separation

As we have demonstrated above, the observed ordered, phase-separation of two-component mixtures of ligands on nanoparticles seems to be driven by the high curvature of the underlying nanoparticle core. Since our first publication[13] of the observation of 'ripples' on mixed ligand metal nanoparticles several other authors have published similar results on related systems[48] (e.g. lateral phase separation of polymers on silica nanoparticles[49]) further supporting the conclusion of high curvature as a driving force for ordered phase separation. Additionally it has long been known and demonstrated that the assembly of objects around a sphere is subject to constraints not found on flat surface, leading to different packing motifs than those found on flat surfaces. One of the best known examples of this is that while the assembly of hard spheres over a flat surface leads to a close packed hexagonal array—the most efficient packing—such a six-fold lattice cannot be wrapped around the curved surface of a sphere; instead defects must be introduced. This effect is seen in virus morphology, protein s-layers, and even the Thompson problem of the distribution of charges around a sphere.

In order to understand the effect of spherical packing on phase separation in SAMS, we must first consider the 2-D packing of SAMs. For a SAM formed on a flat surface, the molecules pack together into a hexagonal array, all assuming the same tilt angle. The order parameter that describes this SAM is a vector representing the projection of the molecules onto the plane (Figure 3.21a).[46] Thus, if we consider only the vector associated with each molecule on the plane, we find that the vectors form a perfect 'vectorial' crystal propagating across the entire surface (Figure 3.21b). However if we now apply the same treatment to a SAM on a nanoparticle (now projecting the molecules onto the curved nanoparticle core) we find that we cannot form a perfect vectorial crystal. This is described in a topological theorem known as the 'Hairy Ball Theorem' which states: 'vectorial order cannot propagate on a topological sphere unless the vector assumes a zero value in at least two points, called poles.' These two points, or defects, repel one another, and thus end up at diametrically opposed points on the sphere.[46] In sum, in order to form an ordered monolayer on a sphere (note that the nanoparticle core is the topological equivalent of a sphere), two defect points must be introduced (Figure 3.22a). Extending this treatment to mixed ligand, rippled nanoparticles, there are now two lengths of vectors which can propagate around the sphere as depicted in Figure 3.22b. We see that the vectors can only form ordered rings if two poles are generated at diametrically opposed positions on the core where the rings collapse. As was presented above in section 3.4.1, we have observed these poles for rippled particles, surrounded by rings of molecules. This experimental confirmation of poles suggests that the 'Hairy Ball Theorem' and its subsequent results for ligand coated nanoparticles are likely applicable to the packing of ligands around the core. Additionally, Nelson and coworkers have proposed and demonstrated the formation of such defect points on analogous systems using similar reasoning.[46] Thus examining our results in light of the topological theory of ordering on curved surface as well as with the insights from the molecular simulations of Glotzer (personal communication) we propose that the phase-separation of the ligand shell into molecular-scale domains occurs as the result of the large degree of conformation freedom that can be attained by the endgroups by such organization. Furthermore, because the ligands assume a tilt angle on the nanoparticle core, thereby generating a vector field over the surface, two point defects must be introduce into the ligand shell at the poles, resulting in the ordering of the domains into rings which encircle the core.

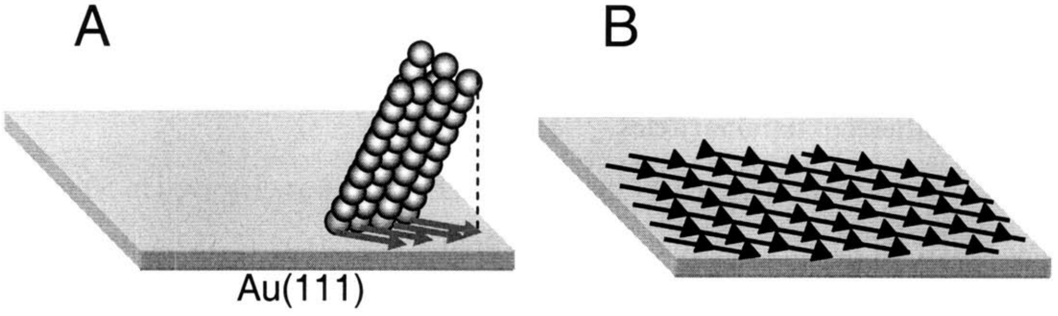

Figure 3.21 Ligand organization and corresponding vectorial order in a 2-D SAM in which a perfect vectorial crystal is formed that can propagate across the entire surface.

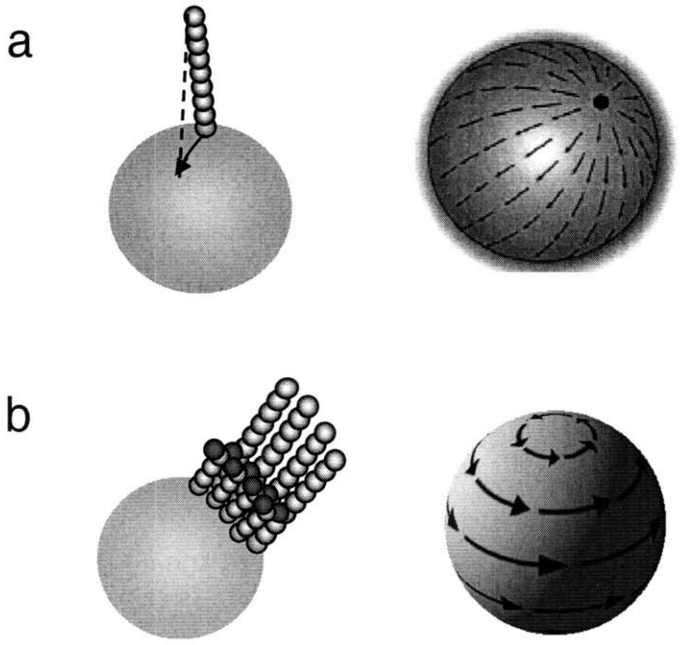

Figure 3.22 Schematic of ligand organization and corresponding vector propagation for (a) homoligand and (b) mixed ligand nanoparticles. Note that in both cases, vector propagation across the core can only occur if two defect points are formed at the poles of the particles. Grey figures taken from: D. Nelson, Nano Lett. 2002, 2, 1125.

3.8. Experimental

3.8.1. Synthesis of nanoparticles

2-Phase Method. $HAuCl_4 \cdot 3H_2O$ (354.45 mg, 0.9 mmol) was dissolved in 50 ml of water and stirred for 10 min. A 4-fold excess of $(BrN((CH_2)_7CH_3)_4$ (2.187 g, 4mmol) was dissolved in 80 ml of toluene, added to the aqueous phase, and the mixture left stirring for 30 min, or until the color due to the gold salt had transfer completely to the organic phase. The thiolated molecule (or a mixture of thiolated molecules) (0.9 mmol) was injected into the solution and allowed to react for 20 minutes, after which the solution typically attained a white color. 30 ml of a 0.33 M water solution of $NaBH_4$ were added slowly dropwise until the solution became a deep red color and then the drop rate was increased to ~1 drop per second. After 2 hours of stirring, the phases were separated, the organic phase was washed 3 times with water, and then reduced to 10 ml and diluted with ~80 ml of ethanol. The solution was left in the refrigerator overnight to allow for the nanoparticles to slowly precipitate. The particles were collected by vacuum filtration using a quantitative paper filter and washed extensively with water, ethanol, acetonitrile, and acetone. Typically the collected black powder weighed ~100 mg. Nanoparticles that were soluble in ethanol were collected by vacuum evaporation of the ethanol solution and extensive rinsing with water, acetone, and toluene.

1-Phase Method. The entire reaction was performed at 0 °C. To 500 ml absolute ethanol, $HAuCl_4 \cdot 3H_2O$ (354.45 mg, 0.9 mmol) was added and stirred for 10 min. The thiolated molecule (or a mixture of thiolated molecules) (0.9 mmol) was injected into the solution and allowed to react for 20 minutes. 200 ml of a supersaturated solution of $NaBH_4$ in ethanol were then added slowly dropwise until the solution became a deep red color and then the drop rate was increased to ~1 drop per second. After complete addition, the solution was stirred for 2h and then transferred to the refrigerator to slowly precipitate. The particles were then isolated and cleaned as described for 2-phase synthesis.

3.8.2. Creation of bare nanocrystal coated substrates

In order to create gold surfaces of high curvature, substrates coated with bare nanocrystals were formed using one of two methods. 1) Creation of 10 nm gold hemispheres: a nanoparticle monolayer on Au(111) on mica, was placed in a round bottom flask under vacuum (10^{-3} Torr) and then heated at 170 °C for 1 h to allow for desorption of thiols. The flask was brought back to atmospheric pressure and allowed to cool to room temperature. The sample was then cleaned with acetone and imaged with STM. 2) Creation of ~4 nm hemispheres: a nanoparticle submonolayer on Au(111) on mica was irradiated with UV light (21.7 mW cm^{-2}, B-100 AP, Fisher Scientific) for 8 h.; The subsrate was then rinsed with acetone and ethanol and imaged with STM. Both samples showed absence of ligands in STM.

3.8.3. STM imaging of the ligand shell

An analysis and discussion of STM imaging parameters, control studies, image interpretation, and measurement methods used to determine the structure and the ordering of molecules on metal nanoparticles is presented in Chapter 3.

3.9. References

1. Hostetler, M. J.; Wingate, J. E.; Zhong, C. J.; Harris, J. E.; Vachet, R. W.; Clark, M. R.; Londono, J. D.; Green, S. J.; Stokes, J. J.; Wignall, G. D.; Glish, G. L.; Porter, M. D.; Evans, N. D.; Murray, R. W., Alkanethiolate gold cluster molecules with core diameters from 1.5 to 5.2 nm: Core and monolayer properties as a function of core size. *Langmuir* **1998,** 14, (1), 17-30.
2. Badia, A.; Cuccia, L.; Demers, L.; Morin, F.; Lennox, R. B., Structure and dynamics in alkanethiolate monolayers self-assembled on gold nanoparticles: A DSC, FT-IR, and deuterium NMR study. *Journal of the American Chemical Society* **1997,** 119, (11), 2682-2692.
3. Hostetler, M. J.; Stokes, J. J.; Murray, R. W., Infrared spectroscopy of three-dimensional self-assembled monolayers: N-alkanethiolate monolayers on gold cluster compounds. *Langmuir* **1996,** 12, (15), 3604-3612.
4. Luedtke, W. D.; Landman, U., Structure and thermodynamics of self-assembled monolayers on gold nanocrystallites. *Journal of Physical Chemistry B* **1998,** 102, (34), 6566-6572.
5. Gutierrez-Wing, C.; Ascencio, J. A.; Perez-Alvarez, M.; Marin-Almazo, M.; Jose-Yacaman, M., On the structure and formation of self-assembled lattices of gold nanoparticles. *Journal of Cluster Science* **1998,** 9, (4), 529-545.
6. Bigioni, T. P.; Harrell, L. E.; Cullen, W. G.; Guthrie, D. E.; Whetten, R. L.; First, P. N., Imaging and tunneling spectroscopy of gold nanocrystals and nanocrystal arrays. *European Physical Journal D* **1999,** 6, (3), 355-364.
7. Harrell, L. E.; Bigioni, T. P.; Cullen, W. G.; Whetten, R. L.; First, P. N., Scanning tunneling microscopy of passivated Au nanocrystals immobilized on Au(111) surface. *Journal of Vacuum Science & Technology B* **1999,** 17, (6), 2411-2416.
8. Rolandi, M.; Scott, K.; Wilson, E. G.; Meldrum, F. C., Manipulation and immobilization of alkane-coated gold nanocrystals using scanning tunneling microscopy. *Journal of Applied Physics* **2001,** 89, (3), 1588-1595.
9. Li, J.; Liang, K. S.; Camillone, N.; Leung, T. Y. B.; Scoles, G., The Structure of N-Octadecane Thiol Monolayers Self-Assembled on Au(001) Studied by Synchrotron X-Ray and Helium Atom Diffraction. *Journal of Chemical Physics* **1995,** 102, (12), 5012-5028.
10. Love, J. C.; Estroff, L. A.; Kriebel, J. K.; Nuzzo, R. G.; Whitesides, G. M., Self-assembled monolayers of thiolates on metals as a form of nanotechnology. *Chemical Reviews* **2005,** 105, (4), 1103-1169.
11. Poirier, G. E.; Tarlov, M. J., The C(4x2) Superlattice of N-Alkanethiol Monolayers Self-Assembled an Au(111). *Langmuir* **1994,** 10, (9), 2853-2856.
12. Stranick, S. J.; Atre, S. V.; Parikh, A. N.; Wood, M. C.; Allara, D. L.; Winograd, N.; Weiss, P. S., Nanometer-scale phase separation in mixed composition self-assembled monolayers. *Nanotechnology* **1996,** 7, (4), 438-442.
13. Jackson, A. M.; Myerson, J. W.; Stellacci, F., Spontaneous assembly of subnanometre-ordered domains in the ligand shell of monolayer-protected nanoparticles. *Nature Materials* **2004,** 3, (5), 330-336.

14. Folkers, J. P.; Laibinis, P. E.; Whitesides, G. M., Self-Assembled Monolayers of Alkanethiols on Gold - Comparisons of Monolayers Containing Mixtures of Short-Chain and Long-Chain Constituents with Ch3 and Ch2oh Terminal Groups. *Langmuir* **1992,** 8, (5), 1330-1341.

15. Smith, R. K.; Reed, S. M.; Lewis, P. A.; Monnell, J. D.; Clegg, R. S.; Kelly, K. F.; Bumm, L. A.; Hutchison, J. E.; Weiss, P. S., Phase separation within a binary self-assembled monolayer on Au{111} driven by an amide-containing alkanethiol. *Journal of Physical Chemistry B* **2001,** 105, (6), 1119-1122.

16. Delamarche, E.; Michel, B.; Biebuyck, H. A.; Gerber, C., Golden interfaces: The surface of self-assembled monolayers. *Advanced Materials* **1996,** 8, (9), 719-&.

17. Hocking, J. G.; Young, G. S., *Topology*. Dover: New York, 1988.

18. Bausch, A. R.; Bowick, M. J.; Cacciuto, A.; Dinsmore, A. D.; Hsu, M. F.; Nelson, D. R.; Nikolaides, M. G.; Travesset, A.; Weitz, D. A., Grain boundary scars and spherical crystallography. *Science* **2003,** 299, (5613), 1716-1718.

19. Terrill, R. H.; Postlethwaite, T. A.; Chen, C. H.; Poon, C. D.; Terzis, A.; Chen, A. D.; Hutchison, J. E.; Clark, M. R.; Wignall, G.; Londono, J. D.; Superfine, R.; Falvo, M.; Johnson, C. S.; Samulski, E. T.; Murray, R. W., Monolayers in three dimensions: NMR, SAXS, thermal, and electron hopping studies of alkanethiol stabilized gold clusters. *Journal of the American Chemical Society* **1995,** 117, (50), 12537-12548.

20. Landman, U.; Luedtke, W. D., Small is different: energetic, structural, thermal, and mechanical properties of passivated nanocluster assemblies. *Faraday Discussions* **2004,** 125, 1-22.

21. Zanchet, D.; Hall, B. D.; Ugarte, D., Structure population in thiol-passivated gold nanoparticles. *Journal of Physical Chemistry B* **2000,** 104, (47), 11013-11018.

22. Hostetler, M. J.; Templeton, A. C.; Murray, R. W., Dynamics of place-exchange reactions on monolayer-protected gold cluster molecules. *Langmuir* **1999,** 15, (11), 3782-3789.

23. Whetten, R. L.; Shafigullin, M. N.; Khoury, J. T.; Schaaff, T. G.; Vezmar, I.; Alvarez, M. M.; Wilkinson, A., Crystal structures of molecular gold nanocrystal arrays. *Accounts of Chemical Research* **1999,** 32, (5), 397-406.

24. Poirier, G. E.; Tarlov, M. J.; Rushmeier, H. E., 2-Dimensional Liquid-Phase and the Px-Root-3-Phase of Alkanethiol Self-Assembled Monolayers on Au(111). *Langmuir* **1994,** 10, (10), 3383-3386.

25. Ulman, A.; Eilers, J. E.; Tillman, N., Packing and Molecular-Orientation of Alkanethiol Monolayers on Gold Surfaces. *Langmuir* **1989,** 5, (5), 1147-1152.

26. Strong, L.; Whitesides, G. M., Structures of Self-Assembled Monolayer Films of Organosulfur Compounds Adsorbed on Gold Single-Crystals - Electron-Diffraction Studies. *Langmuir* **1988,** 4, (3), 546-558.

27. Osman, H.; Schmidt, J.; Svensson, K.; Palmer, R. E.; Shigeta, Y.; Wilcoxon, J. P., STM studies of passivated Au nanocrystals immobilised on a passivated Au(111) surface: ordered arrays and single electron tunnelling. *Chemical Physics Letters* **2000,** 330, (1-2), 1-6.

28. Gusev, A. O.; Taleb, A.; Silly, F.; Charra, F.; Pileni, M. P., Inhomogeneous photon emission properties of self-assembled metallic nanocrystals. *Advanced Materials* **2000,** 12, (21), 1583-+.

29. Fasolka, M. J.; Mayes, A. M., Block copolymer thin films: Physics and applications. *Annual Review of Materials Research* **2001,** 31, 323-355.
30. Plass, R.; Last, J. A.; Bartelt, N. C.; Kellogg, G. L., Nanostructures - Self-assembled domain patterns. *Nature* **2001,** 412, (6850), 875-875.
31. Seul, M.; Andelman, D., Domain Shapes and Patterns - the Phenomenology of Modulated Phases. *Science* **1995,** 267, (5197), 476-483.
32. Cleveland, C. L.; Landman, U.; Shafigullin, M. N.; Stephens, P. W.; Whetten, R. L., Structural evolution of larger gold clusters. *Zeitschrift Fur Physik D-Atoms Molecules and Clusters* **1997,** 40, (1-4), 503-508.
33. Fenter, P.; Eberhardt, A.; Eisenberger, P., Self-Assembly of N-Alkyl Thiols as Disulfides on Au(111). *Science* **1994,** 266, (5188), 1216-1218.
34. Fenter, P.; Schreiber, F.; Berman, L.; Scoles, G.; Eisenberger, P.; Bedzyk, M. J., On the structure and evolution of the buried S/Au interface in self-assembled monolayers: X-ray standing wave results. *Surface Science* **1998,** 413, 213-235.
35. Kluth, G. J.; Carraro, C.; Maboudian, R., Direct observation of sulfur dimers in alkanethiol self-assembled monolayers on Au(111). *Physical Review B* **1999,** 59, (16), R10449-R10452.
36. Zerulla, D.; Chasse, T., X-ray induced damage of self-assembled alkanethiols on gold and indium phosphide. *Langmuir* **1999,** 15, (16), 5285-5294.
37. Wan, L. J.; Hara, Y.; Noda, H.; Osawa, M., Dimerization of sulfur headgroups in 4-mercaptopyridine self-assembled monolayers on Au(111) studied by scanning tunneling microscopy. *Journal of Physical Chemistry B* **1998,** 102, (31), 5943-5946.
38. Fischer, D.; Curioni, A.; Andreoni, W., Decanethiols on gold: The structure of self-assembled monolayers unraveled with computer simulations. *Langmuir* **2003,** 19, (9), 3567-3571.
39. Muller-Meskamp, L.; Lussem, B.; Karthauser, S.; Waser, R., Rectangular (3 x 2 root 3) superlattice of a dodecanethiol self-assembled monolayer on Au(111) observed by ultra-high-vacuum scanning tunneling microscopy. *Journal of Physical Chemistry B* **2005,** 109, (23), 11424-11426.
40. Song, Y.; Heien, M. L. A. V.; Jimenez, V.; Wightman, R. M.; Murray, R. W., Voltammetric detection of metal nanoparticles separated by liquid chromatography. *Analytical Chemistry* **2004,** 76, (17), 4911-4919.
41. Pradeep, T.; Mitra, S.; Nair, A. S.; Mukhopadhyay, R., Dynamics of alkyl chains in monolayer-protected Au and Ag clusters and silver thiolates: A comprehensive quasielastic neutron scattering investigation. *Journal of Physical Chemistry B* **2004,** 108, (22), 7012-7020.
42. Matsen, M. W.; Bates, F. S., Origins of complex self-assembly in block copolymers. *Macromolecules* **1996,** 29, (23), 7641-7644.
43. Suo, Z.; Gao, Y. F.; Scoles, G., Nanoscale domain stability in organic monolayers on metals. *Journal of Applied Mechanics-Transactions of the Asme* **2004,** 71, (1), 24-31.
44. Laibinis, P. E.; Nuzzo, R. G.; Whitesides, G. M., Structure of Monolayers Formed by Coadsorption of 2 Normal-Alkanethiols of Different Chain Lengths on Gold and Its Relation to Wetting. *Journal of Physical Chemistry* **1992,** 96, (12), 5097-5105.
45. DeVries, G. A.; Brunnbauer, M.; Hu, Y.; Jackson, A. M.; Long, B.; Neltner, B. T.; Uzun, O.; Wunsch, B. H.; Stellacci, F., Divalent metal nanoparticles. *Science* **2007,** 315, (5810), 358-361.

46. Nelson, D. R., Toward a tetravalent chemistry of colloids. *Nano Letters* **2002,** 2, (10), 1125-1129.
47. Lu, W.; Suo, Z., Symmetry breaking in self-assembled monolayers on solid surfaces. II. Anisotropic substrate elasticity. *Physical Review B* **2002,** 65, (20).
48. Roan, J. R., Soft nanopolyhedra as a route to multivalent nanoparticles. *Physical Review Letters* **2006,** 96, (24), -.
49. Zhao, B.; Zhu, L., Nanoscale phase separation in mixed poly(tert-butyl acrylate)/polystyrene brushes on silica nanoparticles under equilibrium melt conditions. *Journal of the American Chemical Society* **2006,** 128, (14), 4574-4575.

4. Conclusions and Outlook

4.1. Conclusions

In this thesis, I have shown using STM that SAMs on nanoparticles pack and behave differently than on flat surfaces, resulting in unique ligand-shell morphologies. The packing morphologies and behaviors observed are due to the highly faceted and topologically spherical nature of the core—faceting results in a variety of surface crystal structures upon which to pack, the topological spherical nature results in a boundary condition on the ligand packing, and the high curvature results in a radially increasing free volume. These factors, when brought together, generate a radically different energy landscape for ligand packing than seen for 2-D monolayers. As we have presented, the model that best accounts for the SAM behavior on nanoparticle, namely the tight and step-like sulfur packing distances, is one that takes into the account the changing crystallographic nature of the core, but also allows the ligands to relax their conformations, splaying outwards but still conforming to a preferred tilt angle over each hemisphere of the particle. The core's impact on the ligand shell can best seen through the formation of highly ordered rings of domains in the case of two-component, mixed ligand monolayers—a morphology that has never been observed on flat surfaces. Indeed this stripe-like morphology seems to be the thermodynamically preferred one. In this work we have observed this morphology for all of the two-component ligand combinations studied which phase-separate on nanoparticles, across a large range of ligand ratios with only stripe width changing with composition. We have shown that the curvature of the core is the main driving force for molecular-scale phase separation, and propose that it is the rotational symmetry (resulting in a boundary condition) of the core that orders these stripes.

4.2. Outlook

Given that the formation of ordered domains on nanoparticles is a new field, it is quite fruitful in areas of exploration. I focus here on the opportunities available for improved understanding and characterization of SAMs and their phase-separation on nanoparticles. First, for improved understanding, given the power of the nanoparticle core over the resulting ligand shell morphology, there is much low-hanging fruit: varying the size, shape, and composition of both the core and ligand mixtures. In particular,1) studying the upper and lower size limits of the core on the shell packing—at very small core sizes the core may not be seen by the ligands as a sphere and composed of to few ligands to even constitute a monolayer. Furthermore even at a slightly larger size, one could imagine that ripple width would become comparable to core size, and so will phase separation even occur? Will the particles become Janus-like? Or will they separate into two groups of homoligand particles? 2) Study nanoparticles of different shapes, e.g. rods. Although rods still posses a rotational, cylindrical symmetry, they are essentially 'flat' along their long axis—how will this affect the ligand shell morphology? 3) Using flat surface studies to understand further the causes and mechanisms of phase separation on nanoparticles—stress tests. One area that has become particularly fruitful is that of understanding how stress and ligand combinations on flat surface leads to phase separation and specific domain morphologies. While there is much theoretical work in the literature on this topic—little has been done experimentally. However one of the most beneficial projects would be improved visualization of the ligand shell. There are several areas which could be tackled—improved noise isolation, using Ultra-High Vacuum STM, and imaging in fluids. All of these factors have resulted in improved resolution for 2-D SAMs and must be implemented for nanoparticles. Improved resolution would contribute greatly to understanding how ligands arrange themselves within ripples, and in understanding the packing motifs on homoligand nanoparticles. As has already been shown by DeVries at al.,[1] the ability to understand and engineer the resulting ligand shell structure has immediate and enormous benefits towards assembly of nanoparticles into new materials and, in the future, towards new devices.

4.3. References

(1) DeVries, G. A.; Brunnbauer, M.; Hu, Y.; Jackson, A. M.; Long, B.; Neltner, B. T.; Uzun, O.; Wunsch, B. H.; Stellacci, F. *Science* **2007**, *315*, 358-361.